

# Laser-Enhanced Solar Sailing

Modeling and Trajectory Optimization  
for Interplanetary Missions

Livio Carzana

Master of Science Thesis





# LASER-ENHANCED SOLAR SAILING

## MODELING AND TRAJECTORY OPTIMIZATION FOR INTERPLANETARY MISSIONS

by

**Livio Carzana**

4514920

in partial fulfillment of the requirements for the degree of

**Master of Science**  
in Aerospace Engineering

at the Delft University of Technology,  
to be defended publicly on December 18, 2017 at 1 : 00 PM.

Thesis committee: Dr. D.M. Stam, TU Delft, chairholder  
Ir. R. Noomen, TU Delft, supervisor  
Ir. P.P. Sundaramoorthy, TU Delft  
Prof. Dr. -Ing. B. Dachwald, FH Aachen, external supervisor

*This thesis is confidential and cannot be made public until December 31, 2018.*

An electronic version of this thesis is available at <http://repository.tudelft.nl/>.

This thesis project was pursued at the aerospace engineering faculty  
of the FH Aachen University of Applied Sciences.



Copyright © Astrodynamics and Space Missions.  
All rights reserved.





*Partiti da lontano,  
per arrivare ad essere contenti.*

*Francesco Motta*



# ACKNOWLEDGMENTS

I proudly present this report as the result of several months of work spent between Germany and Italy. All this time has been characterized by the presence of people who helped me get through this thesis project and which I would like to deeply thank.

First of all my gratitude goes to my supervisors, Ron Noomen and Bernd Dachwald, for their technical support, the countless meetings, advices, and great availability on which I could always rely. In particular a special thank goes to Professor Dachwald, who made it possible for me to work at FH Aachen, giving me the chance to use In-Trance and write a conference paper on my thesis work. Furthermore, I would like to thank also Andreas Ohndorf for having provided me with all files I needed to actually work with the program.

I am deeply grateful to my parents for the support they gave me throughout the last two years, till this very moment. I want you to know that all the steps I am moving towards my future are just the result of your trust, love and sacrifices. Moreover, many thanks go to my brother, Matteo, for having let me work with his high-performance computer whenever I needed, and for his endless patience especially during my last months of work.

Many thanks go to Debora and all my "sfravcated" mates, Pietro, Manuel, Fefy, Maurizio, Vinz, Mario, Peppe and Fabiano: I'm glad you guys are my closest friends and a constant presence in my life, despite the distance dividing us.

Eventually I would like to thank all "Bombers", Alex, Chiara C., Chiara R., Miguel, Mattia, Giova, Giò and Francesco, for the wonderful moments shared in Delft and around Europe. You guys have really been like a family to me.

In particular some special thanks go to Chiara C., a great friend with whom I shared most of my university life and Dutch experience. I really thank you for the countless hours spent at the phone, the sleepless study nights, the reciprocal support and for having taught me how to cook some noodles without burning up our flat.

Speaking of burning up things, I also want to thank Chiara R. for having introduced me to Aachen as soon as I arrived in the city, and for having been a constant presence of my German staying with whom I have shared many beautiful (and some bad...) experiences.

Last but not least, I am really thankful to Alex for his friendship, the suffering shared while working together on assignments and, above all, the great support he gave me during my last months of thesis work.

*Livio Carzana*  
*Santa Maria Capua Vetere, December 1, 2017*



## ABSTRACT

When sunlight illuminates a body, a tiny pressure is exerted upon its surface due to the photons impacting on it. Such a principle forms the basis of solar sailing, in which the solar radiation pressure is used to accelerate highly reflective lightweight structures called solar sails. Similarly, a laser-enhanced solar sail is a solar sail in which also an external laser beam pointed towards the sail is exploited to generate thrust. In this way an additional laser radiation pressure is exerted onto the sail, hence conferring higher propulsive and steering capabilities, and leading to an increased maneuverability of the sailcraft.

The main purpose of this research is to provide a model of the laser-enhanced solar sail dynamics and to establish the advantages of laser-enhanced solar sailing as compared to "traditional" solar sailing. The analysis has been pursued focusing on interplanetary missions and considering ideal sails, i.e. sails able to perfectly reflect the impinging radiation. Normally, for low-thrust interplanetary missions the propellant consumption and time of flight required for the transfers to take place play a crucial role. However, since solar sails do not exploit any propellant, the traditional and laser-enhanced sailcraft performances have been compared by analyzing their flight-time optimal trajectories, focusing on three different mission scenarios: a Mercury orbit rendezvous, Mars orbit rendezvous and Neptune flyby. These trajectories have been computed by taking advantage of an evolutionary neurocontrol optimizer, in which newly added functionalities have been implemented with the purpose of optimizing laser-enhanced solar sail trajectories. The trajectory analysis results have shown that, if laser-enhanced sailcraft are used instead of traditional sailcraft, flight time gains in the order of 8–11% can be achieved for the missions to Mercury and Mars orbits, while a smaller 2.5% gain is achieved for the flyby mission to Neptune.



# TABLE OF CONTENTS

<b>Preface</b>	<b>i</b>
<b>Abstract</b>	<b>iii</b>
<b>Abbreviations, Units, Constants and Symbols</b>	<b>vii</b>
<b>1 Introduction</b>	<b>3</b>
<b>2 State-of-the-Art Technology</b>	<b>5</b>
2.1 Heritage . . . . .	5
2.1.1 Solar Sailing . . . . .	5
2.1.2 Laser-Pushed Sailing and Laser-Enhanced Solar Sailing. . . . .	9
2.2 Technology Readiness Level . . . . .	10
<b>3 Mathematical Model</b>	<b>15</b>
3.1 Reference Frames . . . . .	15
3.1.1 J2000 Heliocentric Ecliptic Reference Frame . . . . .	15
3.1.2 Orbital Reference Frame . . . . .	16
3.2 Coordinates Systems . . . . .	17
3.2.1 Cartesian Coordinates . . . . .	17
3.2.2 Spherical Coordinates . . . . .	17
3.2.3 Keplerian Elements . . . . .	19
3.2.4 Modified Equinoctial Elements. . . . .	19
3.2.5 Solar Sail Attitude Vectors and Angles . . . . .	20
3.3 Reference Frame Transformations . . . . .	21
3.3.1 Rotation Matrix-based Method. . . . .	21
3.3.2 Quaternion-based Method . . . . .	22
3.4 Solar Radiation Pressure Models . . . . .	23
3.4.1 Point-like Solar Radiation Pressure Model . . . . .	23
3.4.2 Finite Solar Disk Solar Radiation Pressure Model . . . . .	24
3.4.3 Choice of the Solar Radiation Pressure Model . . . . .	24
3.5 Laser Radiation Pressure Force Model . . . . .	25
3.6 Radiation Pressure Force Models . . . . .	28
3.6.1 Ideal Reflection Models . . . . .	28
3.6.2 Optical Radiation Models . . . . .	29
3.6.3 Generalized Sail Model. . . . .	32
3.6.4 Choice of Sail Model . . . . .	33
3.7 Perturbing Forces . . . . .	35
3.8 Equations of Motion . . . . .	37
3.8.1 Vectorial Form . . . . .	37
3.8.2 Choice of the Coordinates System . . . . .	39
3.8.3 Equations of Motion in Spherical Coordinates . . . . .	40

<b>4</b>	<b>Optimization</b>	<b>43</b>
4.1	Choice of optimizer . . . . .	43
4.2	InTrance Overview . . . . .	44
4.2.1	Evolutionary Neurocontrol . . . . .	44
4.2.2	Architecture . . . . .	46
4.2.3	Optimization Outputs . . . . .	47
<b>5</b>	<b>Implementation and Validation</b>	<b>49</b>
5.1	Laser-Enhanced Solar Sailing Implementation within InTrance . . .	49
5.2	Validation of Laser Radiation Pressure Acceleration Model . . . . .	52
5.2.1	Dependency on Critical Laser Distance. . . . .	52
5.2.2	Laser Radiation Pressure Acceleration . . . . .	55
5.3	Computational Performances of Different Frame Rotation Methods	56
5.4	Validation of Laser Generator Powering-Off Scenarios . . . . .	59
5.4.1	Solar Sail Back-Side Exposure. . . . .	59
5.4.2	Solar Occultation . . . . .	62
5.4.3	Extremely High Laser Flux Impinging . . . . .	64
5.5	Validation of Laser-Enhanced Solar Sailing Optimization . . . . .	66
<b>6</b>	<b>Simulation Setup and Parameter Tuning</b>	<b>71</b>
6.1	Simulation Scenarios . . . . .	71
6.2	Laser Source and Sailcraft Parameters. . . . .	73
6.3	Laser Source Position . . . . .	75
6.4	Integrator Choice and Tuning. . . . .	78
6.4.1	Mission to the Inner Solar System . . . . .	79
6.4.2	Mission to the Outer Solar System . . . . .	82
6.5	Neural Network Structure and Chromosome Population Size. . . . .	87
<b>7</b>	<b>Results and Analysis</b>	<b>91</b>
7.1	Mercury Orbit Rendezvous . . . . .	91
7.2	Mars Orbit Rendezvous. . . . .	95
7.3	Neptune Flyby . . . . .	99
<b>8</b>	<b>Conclusions and Recommendations</b>	<b>107</b>
<b>A</b>	<b>Appendix</b>	<b>111</b>
A.1	Flight Time Variation due to Neptune's Perturbing Acceleration . . .	111
A.2	Files Modified and Implemented within InTrance. . . . .	112
A.3	Laser Source Positioning for the Missions to Neptune and Mars Orbit . . . . .	112
A.3.1	Neptune Flyby Mission. . . . .	113
A.3.2	Mars Orbit Rendezvous Mission . . . . .	113
	<b>References</b>	<b>117</b>

# ABBREVIATIONS, UNITS, CONSTANTS AND SYMBOLS

## ABBREVIATIONS

<b>2BP</b>	Two-body problem	<b>InTrance</b>	Intelligent trajectory optimization using neurocontroller evolution
<b>AN</b>	Ascending node	<b>IR</b>	Ideal reflection
<b>ANN</b>	Artificial neural network	<b>J2000</b>	1 <sup>st</sup> January 2000
<b>AU</b>	Astronomical Unit	<b>JAXA</b>	Japan Aerospace Exploration Agency
<b>CLSA</b>	Close laser source approach	<b>LE</b>	Laser-enhanced
<b>CM</b>	Center of mass	<b>LEO</b>	Low Earth orbit
<b>DCM</b>	Direction cosine matrix	<b>LG</b>	Laser generator
<b>DES</b>	Differential equation system	<b>LHS</b>	Left-hand side
<b>DLR</b>	Deutsches Zentrum für Luft- und Raumfahrt	<b>LRP</b>	Laser radiation pressure
<b>DP</b>	Dormand & Prince	<b>LS</b>	Laser source
<b>EA</b>	Evolutionary algorithm	<b>LTOM</b>	Local trajectory optimization method
<b>ENC</b>	Evolutionary neurocontrol	<b>MJD</b>	Modified Julian Date
<b>EoM</b>	Equations of motion	<b>NASA</b>	National Aeronautics and Space Administration
<b>ESA</b>	European Space Agency	<b>NEA</b>	Near Earth Asteroid
<b>GEO</b>	Geostationary Earth orbit	<b>OR</b>	Optical radiation
<b>GTOM</b>	Global trajectory optimization method	<b>PaGMO</b>	Parallel Global Multiobjective Optimiser
<b>HEO</b>	High Earth orbit	<b>RAAN</b>	Right ascension of the ascending node
<b>i4is</b>	Initiative for Interstellar Studies	<b>RHS</b>	Right-hand side
<b>IC</b>	Initial condition	<b>RK</b>	Runge-Kutta
<b>IKAROS</b>	Interplanetary Kite-craft Accelerated by Radiation Of the Sun	<b>RKF</b>	Runge-Kutta-Fehlberg

<b>S/C</b>	Spacecraft	<b>SSE</b>	Search scan epoch
<b>SOI</b>	Sphere of influence	<b>TOF</b>	Time of flight
<b>SPA</b>	Solar photonic assist	<b>TUDAT</b>	TU Delft Astrodynamics Toolbox
<b>SRI</b>	Solar radiation interference	<b>U<sub>235</sub></b>	Uranium-235
<b>SRP</b>	Solar radiation pressure	<b>UV</b>	Ultraviolet

## UNITS

AU	$1.49597870700 \cdot 10^{11}$ m	Astronomical Unit [Wakker, 2015, p.671]
day	86400 s	Mean solar day [Wakker, 2015, p.671]
year	365.256363 days	Earth sidereal year [Wakker, 2015, p.671]

## CONSTANTS

$a_{\text{♃}}$	0.387099 AU	Mercury semi-major axis [Wakker, 2015, p.673]
$a_{\text{♀}}$	0.723336 AU	Venus semi-major axis [Wakker, 2015, p.673]
$a_{\text{♆}}$	30.069923 AU	Neptune semi-major axis [Wakker, 2015, p.673]
$c$	$2.99792458 \cdot 10^8$ ms <sup>-1</sup>	Speed of light in vacuum [NIST, 2017]
$\mathcal{L}_{\odot}$	$3.828 \cdot 10^{26}$ Js <sup>-1</sup>	Solar Luminosity [NASA, 2017c]
$P_0$	$4.563 \cdot 10^{-6}$ Nm <sup>-2</sup>	Solar radiation pressure at Earth [Dachwald, 2004, p.8]
$R_{\odot}$	$6.95700 \cdot 10^8$ m	Mean solar radius [NASA, 2017c]
$R_{SOI, \text{♃}}$	$1.1 \cdot 10^8$ m	Mercury sphere of influence radius [Wakker, 2015, p.115]
$R_{SOI, \text{♂}}$	$5.8 \cdot 10^8$ m	Mars sphere of influence radius [Wakker, 2015, p.115]
$R_{SOI, \text{♆}}$	$8.66 \cdot 10^{10}$ m	Neptune sphere of influence radius [Wakker, 2015, p.115]
$S_0$	$1368$ Js <sup>-1</sup> m <sup>-2</sup>	Solar constant [Beatty et al., 1981, p.36]
$T_{\text{♀}, \text{syn}}$	583.92 days	Earth-Venus synodic period [NASA, 2017e]
$\epsilon$	$2.2204 \cdot 10^{-16}$	Machine epsilon
$\tilde{\epsilon}$	23.439279 deg	Obliquity of the ecliptic [Wakker, 2015, p.671]
$\mu_{\odot}$	$1.327124421 \cdot 10^{20}$ m <sup>3</sup> s <sup>-2</sup>	Solar gravitational parameter [Wakker, 2015, p.673]
$\mu_{\text{♃}}$	$2.2032 \cdot 10^{13}$ m <sup>3</sup> s <sup>-2</sup>	Mercury gravitational parameter [NASA, 2017a]
$\mu_{\text{♆}}$	$6.8351 \cdot 10^{15}$ m <sup>3</sup> s <sup>-2</sup>	Neptune gravitational parameter [NASA, 2017b]

$\sigma^*$	$1.53 \text{ gm}^{-2}$	Critical sail loading parameter [McInnes, 1999, p.40]
------------	------------------------	---

## LATIN SYMBOLS

$A$	[–] [m <sup>2</sup> ]	Action Area
$\mathbf{a}$	[ms <sup>-2</sup> ]	Acceleration vector
$a$	[ms <sup>-2</sup> ] [–] [m]	Acceleration magnitude Refined optical radiation sail model coefficient Semi-major axis
$B$	[–]	Non-Lambertian coefficient
$D$	[m]	Laser generator collimating lens diameter
$\hat{\mathbf{d}}$	[–]	Transversal unit vector
$d$	[m]	Equivalent sail diameter
$\mathcal{E}$	[J]	Radiation energy
$\hat{\mathbf{e}}$	[–]	Rotation axis unit vector
$e$	[–]	Eccentricity
$\mathbf{F}$	[N]	Force vector
$F$	[N]	Force magnitude
$\hat{\mathbf{f}}$	[–]	Thrust unit vector
$f$	[–]	Second modified equinoctial element
$g$	[–]	Third modified equinoctial element
$\hat{\mathbf{h}}$	[–]	Angular momentum unit vector
$H$	[–]	Search space region
$h$	[–] [s]	Fourth modified equinoctial element Step-size
$\mathcal{J}$	[–]	J2000 heliocentric ecliptic reference frame
$I$	[Js <sup>-1</sup> m <sup>-2</sup> ]	Solar specific intensity
$i$	[rad]	Inclination
$\mathbf{J}$	[m <sup>2</sup> ]	Surface normal distribution integral
$J$	[–]	Fitness function
$j$	[rad]	Jitter angle
$k$	[–] [–]	Rotation axis identifier Fifth modified equinoctial element
$L$	[Js <sup>-1</sup> m <sup>-2</sup> ] [rad]	Laser flux True longitude
$m$	[kg] [–]	Mass Tensor order
$N$	[–]	Network function
$\hat{\mathbf{n}}$	[–]	Normal unit vector
$\check{\mathbf{n}}$	[–]	Local normal unit vector
$n$	[rads <sup>-1</sup> ]	Mean motion
$\mathcal{O}$	[–]	Orbital reference frame
$O$	[–] [–]	Order of magnitude Reference frame origin
$P$	[Nm <sup>-2</sup> ]	Pressure

$\hat{p}$	[-]	Clock unit vector
$p$	[m]	Semi-latus rectum
$q$	[-]	Quaternion
$R$	[-]	Axis rotation matrix
	[m]	Radius
$\hat{r}'$	[-]	Reflected sunlight direction unit vector
$\hat{r}$	[-]	Radial unit vector
$r$	[m]	Position vector
	[m]	Heliocentric distance
	[m]	Range
$S$	[-]	Strategy
$\hat{s}$	[-]	Laser unit vector
$s$	[m]	Laser vector
$\tilde{s}$	[m]	Critical laser distance
$s$	[m]	Laser distance
	[-]	Specular reflection coefficient
$\mathcal{T}$	[-]	Reference frame
$T$	[-]	Direction cosine matrix
$\hat{t}$	[-]	In-plane transversal unit vector
$\check{t}$	[-]	Local in-plane transversal unit vector
$\bar{t}$	[s]	Discrete time
$\tilde{t}$	[s]	Time of critical laser distance
$t$	[s]	Time
$u$	[-]	Control vector
$u$	[rad]	Argument of pericenter
$V$	[ms <sup>-1</sup> ]	Velocity magnitude
$v$	[ms <sup>-1</sup> ]	Velocity vector
	[-]	Generic vector
$v$	[ms <sup>-1</sup> ]	Velocity magnitude
$W$	[Js <sup>-1</sup> ]	Power
$X$	[-]	Reference frame axis
	[-]	Situation
$x$	[m, ms <sup>-1</sup> , rad, rads <sup>-1</sup> ]	State vector
$x$	[m]	Cartesian coordinate
$Y$	[-]	Reference frame axis
$y$	[m]	Cartesian coordinate
$Z$	[-]	Reference frame axis
$z$	[m]	Cartesian coordinate

## GREEK SYMBOLS

$\alpha$	[rad]	Pitch angle
$\beta$	[rad]	Centerline angle
	[-]	Lightness number
$\Gamma$	[-]	Minimum laser distance solar radiation factor
$\gamma$	[rad]	Angular distance
	[rad]	Euler angle

$\Delta$	[-]	Difference
$\delta$	[-]	Relative or absolute tolerance
	[rad]	Clock angle
$\varepsilon$	[-]	Emission coefficient
	[m, ms <sup>-1</sup> , rad, rads <sup>-1</sup> ]	Integration error
	[rad]	Safety pitch angle margin
$\zeta$	[rad]	Orbit angle
	[-]	Solar disk finiteness correction factor
$\eta$	[-]	Efficiency
$\vartheta$	[rad]	True anomaly
$\hat{\theta}$	[-]	Azimuth unit vector
$\theta$	[rad]	Azimuth angle
	[rad]	Laser beam diffraction-limited divergence angle
	[rad]	Cone angle
$\lambda$	[m]	Laser wavelength
$\mu$	[rad]	Generic angle
	[m <sup>3</sup> s <sup>-2</sup> ]	Gravitational parameter
$\Xi$	[-]	Population
$\xi$	[-]	Chromosome
$\zeta$	[-]	Laser power provision coefficient
$\pi$	[-]	Neural parameters vector
$\rho$	[-]	Reflection coefficient
$\sigma$	[kgm <sup>-2</sup> ]	Sail loading parameter
$\hat{\phi}$	[-]	Polar angle (elevation) unit vector
$\phi$	[rad]	Phase angle
	[rad]	Polar angle (elevation)
$\chi$	[-]	Laser generator throttle
$\Psi$	[-]	Refined optical radiation sail model efficiency
$\Omega$	[rad]	Laser beam divergence solid angle
	[rad]	Right ascension of the ascending node
$\omega$	[rad]	Argument of pericenter

## ASTRONOMICAL SYMBOLS

$\odot$	Sun
$\mercury$	Mercury
$\mars$	Mars
$\venus$	Venus
$\neptune$	Neptune
$\gamma$	First point of Aries

## INDEXES

0	Initial or reference value
<i>b</i>	Back-side
<i>c</i>	Cartesian or characteristic

<i>d</i>	Diffuse or disturbing body
<i>f</i>	Final or front-side
<i>in</i>	Input
<i>k</i>	Generation number
<i>L</i>	Laser
<i>LG</i>	Laser generator
<i>lim</i>	Limit
<i>LS</i>	Laser source
<i>max</i>	Maximum
<i>min</i>	Minimum
<i>out</i>	Output
<i>ref</i>	Reference
<i>rel</i>	Relative
<i>S</i>	Solar
<i>s</i>	Specular or spherical
<i>SC</i>	Spacecraft
<i>SRI</i>	Solar radiation interference
<i>T</i>	Target
<i>wp</i>	Wall-plug
*	Critical, optimal or point-like source
$\infty$	Asymptotic or excess





# 1

## INTRODUCTION

Solar sailing is a propulsion method in which the main source of thrust is the solar radiation impinging on a surface. In fact, when photons impact a body surface they transfer part of their momentum to the body itself, hence defining a so-called solar radiation pressure (SRP). As the latter usually has a small magnitude, also the thrust defined onto the body is relatively small, so that, if a significant acceleration is sought, vast, lightweight and highly reflective structures called solar sails need to be used. Since solar radiation propagates radially from the Sun throughout the Solar System, one of the main advantages of a solar sail is represented by the limitless thrust provision it can rely on. On the other hand, however, solar sails are also constrained in the achievable thrust directions and magnitude, which strictly depend on the sailcraft orientation and position with respect to the Sun.

Theoretically one way to overcome these problems is exploiting another source of radiation besides the Sun, such as a laser beam providing a so-called laser radiation pressure (LRP) to the sailcraft. In fact, in this way an additional acceleration would be provided that is independent of the sail distance or attitude relative to the Sun, therefore making such a laser-enhanced solar sail potentially perform better than a traditional solar sail.

Consequently in the present work a study on laser-enhanced solar sailing as compared to traditional solar sailing has been carried out, with a particular focus on interplanetary missions. Since for low-thrust interplanetary missions one of the aspects playing a crucial role is the time of flight (TOF) required for transfers to be performed, the comparison of these propulsion systems has been carried out with respect to interplanetary flight-time optimal trajectories, in order to measure the (expected) gain in the TOF introduced by the additional exploitation of LRP.

Given the above considerations, the main research question the present work aims to answer is: to what extent is laser-enhanced solar sailing more advantageous with respect to traditional solar sailing? The subquestions to be addressed in order to answer this main question are: what is the dynamical model of a laser-enhanced solar sail? What are the optimal locations of the laser source for missions to the inner and outer Solar System? What is the TOF gain acquired for missions to the inner Solar System? What is instead the gain for missions to the outer Solar System?

This report is structured in order to present all relevant concepts to answer the above research questions. Firstly a survey over the past solar sailing missions and the laser-enhanced solar sailing mission concepts is provided in Chapter 2, with a view to make the reader aware of the current state-of-the-art technology within this field. In Chapter 3 the mathematical modeling of the problem is discussed in detail, and it includes a description of all reference frames, coordinate systems, force models and equations of motion used for analyzing the dynamics of both traditional and laser-enhanced sails. As for answering the above research questions flight-time optimal trajectories have been compared, in Chapter 4 the optimization procedure used to retrieve such orbits is presented. In particular, in order to optimize laser-enhanced sailcraft trajectories, the optimization software has been provided with additional functionalities which are presented and validated in Chapter 5. The mission scenarios analyzed and all parameters used to setup the optimizations are presented in Chapter 6, whereas the optimization results are given in Chapter 7. Eventually, the conclusions and recommendations for future research are given in Chapter 8.

# 2

## STATE-OF-THE-ART TECHNOLOGY

Solar sailing is an innovative spacecraft (S/C) propulsion method in which the SRP is used as thrust source. This pressure is generated by the momentum exchange yielded by solar photons when they impact onto a body surface, so that, consequently, a force is generated and the body itself experiences an acceleration [Dachwald, 2004, pp.7-8]. Since the SRP has, on average, a relatively small magnitude inside the Solar System (e.g. in the order of  $10^{-6} \text{ Nm}^{-2}$  at Earth), in order to capture as much sunlight as possible and hence best exploit such a thrust source, vast and lightweight sail structures called solar sails (or lightsails) are used, therefore giving the name to this propulsion system.

Being a propellant consumption-free propulsion method, solar sailing has drawn the attention of space agencies and companies already in the beginning of the 1970s and, since the 2000s, its feasibility has been assessed by means of ground tests, technology demonstrations and in-space experiments. However, besides solar sails also other propulsion systems based on the same idea of exploiting the radiation pressure to generate thrust have been conceived during the last decades. Among these is laser-enhanced solar sailing, i.e. a propulsive method whose main innovative feature is the capacity to exploit external laser beams which are pointed towards the sailcraft as an auxiliary radiation source. Doing so, the LRP provides an additional acceleration to the sailcraft, while ideally increasing the possibility of defining trajectories that were otherwise unfeasible if traditional solar sailing was used (as will be seen in Chapter 7).

The present chapter serves as presentation of the state-of-the-art technology of solar sailing and laser-enhanced solar sailing, highlighting what is the current achievable performance of such propulsion systems, as well as the current technology readiness level in these fields.

### 2.1. HERITAGE

#### 2.1.1. SOLAR SAILING

Even though the first theoretical concepts investigating the possibility of exploiting SRP for orbital maneuvering were conceived already during the 1950s, mainly thanks

to the work of Richard Garwin and T. C. Tsu ([Garwin, 1958][Tsu, 1959]), solar sailing began being considered a valid alternative to other low-thrust propulsion systems for the first time only in 1973, when the National Aeronautics and Space Administration (NASA) funded a study on the feasibility of a solar sailing comet Halley rendezvous mission, to be performed during the early 1980s [McInnes, 1999, p.5]. Being one of the first in-depth studies on solar sailing, the work carried out by NASA highlighted both the potential and issues related to this propulsion system. In fact, even if it was found that solar sailing could have shortened the TOF to only 4 years for the rendezvous mission (instead of the 7-8 years required by solar-electric ion propulsion), on the other hand exploiting a solar sail would have defined high risks related to its stabilization, deployment and manufacturing, mainly due to the enormous sail dimensions. In fact the proposed sailcraft designs considered either an 800x800 m square sail or the so-called "heliogyro" sail structure, constituted by twelve 7.5 km long blades of reflective film [McInnes, 1999, p.5]. Eventually, due to the above-mentioned risks, both these sailcraft configurations were discarded and the electric ion propulsion was chosen instead (even though, a few time later, also this concept was dropped due to escalating cost estimates). Artistic representations of the sailcraft configurations presented above are shown in Figure 2.1 [McInnes, 1999, p.6].

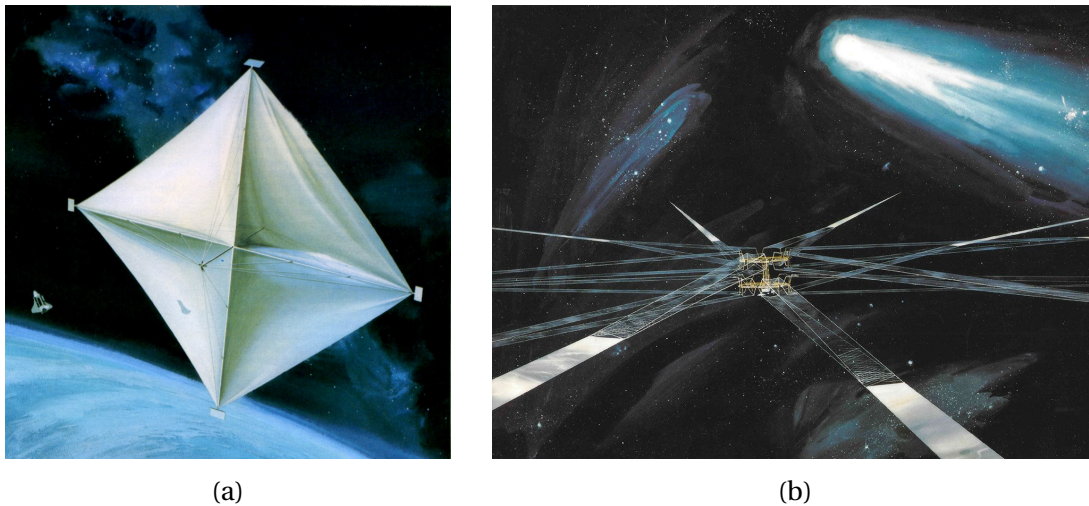


Figure 2.1: Artistic representation of the square sail (a) and heliogyro (b) configurations proposed for the comet Halley rendezvous mission [McInnes, 1999, p.6].

Despite the sailcraft designed for the comet Halley rendezvous mission was not sent to orbit, a renewed optimism built up in the upcoming decades and, not by chance, space agencies around the world already started designing, testing and flying the first demonstrator sailcraft in the 2000s. In particular, the first sail deployment ground test was performed in December 1999 by the Deutsches Zentrum für Luft- und Raumfahrt (DLR) (i.e. the German aerospace center) in cooperation with the European Space Agency (ESA). The test was performed on a 20x20 m sail made of Kapton (i.e. a polyimide used for the sail film) with a thickness of  $7.5 \mu\text{m}$ , and was deployed by taking advantage of ultra-lightweight carbon fiber reinforced plastic booms having a linear density of  $101 \text{ gm}^{-1}$  [Herbeck et al., 2001, pp.108,112][Herbeck et al., 2002, p.9]. Since the maximum achievable sailcraft thrust is strictly related to the sail loading parameter

$\sigma$ , i.e. the ratio of the sailcraft mass to the sail surface area, the sail design was carried out trying to minimize this parameter, eventually achieving a  $\sigma$  of about  $90 \text{ gm}^{-2}$ .

Afterwards, in June 2005, the first attempt in sending a solar sail technology demonstrator to orbit took place with The Planetary Society's Cosmos 1 sailcraft. The sail was composed of eight triangular blades, each one 15 m long, defining a total surface area of  $600 \text{ m}^2$ . The sail film used this time was made of mylar and had a thickness of just  $5 \mu\text{m}$ , hence conferring a small mass to the overall sail structure and a loading parameter of  $67 \text{ gm}^{-2}$  [Herbeck et al., 2002, p.9].

Even though it should have been the first sailcraft to get into orbit, Cosmos 1 was lost because of a malfunctioning in the Volna launcher used for the mission, which made it explode 82 seconds after launch [Friedman, 2017]. Consequently, the first solar sailing technology demonstrator to reach orbit became the Interplanetary Kite-craft Accelerated by Radiation Of the Sun (IKAROS) designed the Japan Aerospace Exploration Agency (JAXA), in 2010. The sailcraft successfully demonstrated the in-orbit deployment of a  $14 \times 14 \text{ m}$  sail [eoPortal, a, 2017], performed the sail attitude control and directly measured the SRP defined on the sail film [JAXA, 2010a][JAXA, 2010b]. However, since the S/C mass was relatively high (roughly equal to  $307 \text{ kg}$  [eoPortal, a, 2017]), SRP could possibly not be the only thrust source exploited and indeed a secondary ion-propulsion system was used for maneuvering [JAXA, 2017].

Successively after IKAROS, space agencies began focusing on different ways to optimize the performance of lightsails, hence making improvements involving the sail material manufacturing, the sail deployment capabilities and the minimization of the overall sailcraft mass. In these terms the most performing sailcraft ever manufactured was Sunjammer, designed by NASA in 2013, which is still nowadays the biggest sailcraft ever developed, with a mass of  $44 \text{ kg}$ , a sail surface area of  $1208 \text{ m}^2$ , a sail film thickness of just  $5 \mu\text{m}$  and a sail loading parameter equal to  $36 \text{ gm}^{-2}$  [Macdonald, 2014, p.117][Space.com, 2013a]. Although Sunjammer was just used for on-ground deployment tests and was never sent to orbit (the project got canceled before launch due to the high schedule risk [Spacenews.com, 2017]), thanks to its characteristics it was expected to provide a relatively high thrust, in the order of  $10^{-2} \text{ N}$  [NASA, 2017d]. A picture of one of the four quadrants of Sunjammer being manually unfolded is given in Figure 2.2 [Space.com, 2013b].



Figure 2.2: Engineers extend one of the four quadrants of Sunjammer's solar sail [Space.com, 2013b].

Besides exploiting solar sailing to accelerate conventional S/C, since IKAROS many other missions have been designed with a view to highlighting the advantages of using solar sailing propulsion also for micro- and nanosatellites. In these terms the most relevant solar sail projects have been NanoSail-D2, from NASA, and Lightsail-1, from The Planetary Society.

Designed in 2008 and launched in May 2010, NanoSail-D2 was a 3-unit cubesat having a mass of 4 kg that successfully demonstrated the space debris de-orbiting feasibility in low Earth orbit (LEO), by means of a 10 m<sup>2</sup> lightsail and a loading parameter of 400 gm<sup>-2</sup> [eoPortal, d, 2017]. A picture of NanoSail-D is given in Figure 2.3a [NASA, 2008].

Similarly, Lightsail-1 was also a 3-unit cubesat launched in 2015 whose mission objective was to perform an in-orbit sail deployment test, which was indeed fulfilled and photographed, as shown in Figure 2.3b [Davis, 2015]. However Lightsail-1 mounted a sail roughly three times larger than the one used by NanoSail-D2, with a surface area of 32 m<sup>2</sup>, hence defining a much smaller loading parameter, only 140 gm<sup>-2</sup> [eoPortal, c, 2017].

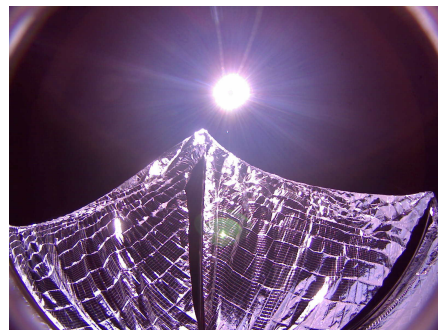
Thanks to the promising results achieved, other solar sailing missions have already been planned for the imminent future, with a view to further assessing this propulsion system's performance.

Among the upcoming small satellite missions, the most relevant one is NASA's Near Earth Asteroid (NEA) Scout mission, which will be flown in 2019 and aims to demonstrate the capability of low-cost sailcraft to perform NEAs reconnaissance. The satellite will be a 6-unit cubesat, with a total mass of roughly 14 kg, propelled through a 86 m<sup>2</sup> sail (hence almost three times larger than the Lightsail-1 one) [Marinan et al.] [Johnson et al., 2017, pp.1-2].

Concerning large sailcraft missions, at present none of them has been planned for the near future. The most recently proposed project has been Gossamer Roadmap, for which three demonstrator sailcraft called Gossamer-1, -2 and -3 were expected to be flown respectively in 2013, 2014 and 2015. In spite of this, however, none of them has been sent to orbit yet, as the Gossamer Roadmap project itself has been momentarily suspended. The main purpose of this project born from the combined efforts of ESA and DLR is to demonstrate the deployment of a 5x5, 20x20 and 50x50 m sails, as well as to demonstrate their full attitude and orbit control. In particular, while Gossamer



(a)



(b)

Figure 2.3: Picture of NanoSail-D and its project team after a sail deployment test [NASA, 2008] (a), and picture of the Lightsail-1 spacecraft taken during the in-space sail deployment [Davis, 2015] (b).

1 and 2 will orbit in LEO, Gossamer-3 is supposed to reach an altitude greater than 10000 km [Geppert et al., 2010].

### 2.1.2. LASER-PUSHED SAILING AND LASER-ENHANCED SOLAR SAILING

Since the achievable thrust provided by a lightsail rapidly decreases as the distance from the Sun increases, the idea of exploiting laser beams with a limited divergence to accelerate lightsails at a large distance from the Sun started being considered already in the 1970s. In these terms, Robert Forward provided numerous studies on laser-pushed solar sails (with a particular focus on missions to other stellar systems) in which he clearly exposed the engineering challenges related to such a propulsion system. As discussed in [Forward, 1984, pp.189-191], these mainly concern the laser beam pointing and tracking. In fact, in order to accelerate a sailcraft at a large distance from the laser source (LS) (e.g. interstellar distances), narrow beams with a small divergence are required, hence defining the need of a highly-accurate pointing. Furthermore, also the finiteness of the speed of light should be considered when pointing the laser beam toward the lightsail, hence requiring a precise estimation of the future sailcraft position to be performed before pointing the laser beam.

Apart from laser-pushed sailing, these issues also affect laser-enhanced solar sailing, even if to a lesser extent. Unlike solar sailing, laser-enhanced solar sailing has never been exploited during a real mission nor during on-ground tests, but, nonetheless, in the last few years several mission concepts taking advantage of the latter propulsion method have been proposed. Among these, the most relevant ones are the Dragonfly Project, founded by the Initiative for Interstellar Studies (i4is) in 2014, and the currently ongoing Breakthrough Starshot program, from The Planetary Society.

The Dragonfly Project's main purpose was to assess the feasibility of a laser-propelled small satellite mission to Alpha Centauri requiring a maximum flight time of 100 years and a laser power of 100 GW at most. To carry out this conceptual study and find the most promising mission design, i4is held a design competition which was won by the team of the Technical University of Munich.

The winning project proved that such a mission would be theoretically feasible using current and near-future technology only in the case some major engineering challenges were to be overcome first. Besides the extremely high laser pointing accuracy required (as already noticed by R. Forward), other problems highlighted were the laser energy spread losses in space (due to the laser beam divergence) and the choice of a suitable sail material (which should be able to efficiently reflect both the solar and laser radiation). The winning team overcame (to some extent) these issues by proposing to use a laser system built of multiple collimating lenses and a highly-reflecting lightweight sail material like graphene, nevertheless underlining the importance of developing also other materials having a smaller density and a higher reflectivity in order to improve the sailcraft performance [Perakis et al., 2016, p.27-29].

Based on Philip Lubin's design proposal for the Dragonfly Project, in June 2016 an even more ambitious project called Breakthrough Starshot was launched by The Planetary Society. Similarly to the Dragonfly Project, the Breakthrough Starshot objective is to study the feasibility of a laser-enhanced solar sailing mission to Alpha Centauri, using ultra-lightweight nano-sailcraft traveling at one-fifth of the speed of light (hence

requiring a total TOF of  $\sim 20$  years) [Breakthrough Initiatives, c, 2017]. At present many mission designs have been proposed, but none of them has ever been analyzed in depth also due to the variety of problems related to the mission feasibility. As for the Dragonfly Project, also in this case the most relevant problems concern the high laser beam pointing accuracy required, which should be at least in the order of 1 milliarc-second ( $\sim 4.8 \cdot 10^{-9}$  rad), and the sail material degradation caused by the high-power laser beam impinging, for which different solutions have been proposed, such as the use of sails made up of graphene and silicon microcubes [Breakthrough Initiatives, a, 2017][Breakthrough Initiatives, b, 2017].

## 2.2. TECHNOLOGY READINESS LEVEL

All missions, tests and conceptual studies presented in the previous section have shown the technological advancements of traditional and laser-enhanced solar sailing. From these the currently available technology readiness level related to these propulsion systems can be outlined.

The first solar sails have been flown already during the 2000s and since then all ground tests and technology demonstrations have been carried out to assess the solar sails deployment feasibility and measure the SRP acceleration exerted onto them. The next step is the demonstration of the full orbit and attitude control in space, which shall be carried out in the near future. Since the sail deployment feasibility strictly depends on the sail dimensions while the SRP acceleration is maximized for lightweight sailcraft, during the years space agencies have aimed at developing more and more lightweight sail materials that could allow the manufacturing of larger sails, capable of being also deployed by small satellites. Consequently during the last two decades the achievable sailcraft mass-to-area ratio has decreased and, therefore, the sailcraft performances have improved. In Table 2.1 the values of the sailcraft mass  $m$ , sail surface area  $A$  and sail loading parameter  $\sigma$  (i.e. the above-mentioned sailcraft mass-to-area ratio) are given for all solar sailing missions discussed in the previous section.

As can be seen, the largest sail ever manufactured is Sunjammer, with an area of  $1208 \text{ m}^2$  and a loading parameter of  $36 \text{ gm}^{-2}$ . Nonetheless, the Gossamer-3 sailcraft, which unfortunately has never been developed, aimed to achieve an even bigger sail with an area approximately twice as the Sunjammer's one and a slightly smaller  $\sigma$  of  $32 \text{ gm}^{-2}$ .

With regard to cubesats, so far the most performing one has been Lightsail-1, mounting a relatively big  $32 \text{ m}^2$  sail which allowed to achieve a  $\sigma$  of  $140 \text{ gm}^{-2}$ . However in 2018 the NEA Scout sailcraft is expected to be sent to orbit and it will exploit an almost three times bigger sail with a surface area of  $86 \text{ m}^2$ .

Both for small and large satellites, the direction of technological improvement mainly aims at minimizing the sail loading parameter, thus maximizing the sailcraft performance. In fact, achieving a small loading parameter helps obtaining a higher acceleration, which in turn makes it possible to perform interplanetary missions and reach distant targets. As a consequence, for many ambitious solar sailing mission concepts, having a small loading parameter represents a crucial requirement which may be fulfilled only through future technological advancements. This direction of technological

Table 2.1: Launch date, S/C mass, sail surface area and sail loading parameter of different sailcraft or solar sail concepts [Herbeck et al., 2001, pp.108,112] [Herbeck et al., 2002, p.9][eoPortal, a, 2017] [Macdonald, 2014, p.117][Space.com, 2013a] [eoPortal, d, 2017][eoPortal, c, 2017] [Johnson et al., 2017, pp.1-2][Geppert et al., 2010].

Year	Sailcraft/Project	m [kg]	A [m <sup>2</sup> ]	$\sigma$ [g/m <sup>2</sup> ]
2000	Deployment test by DLR & ESA	36.6	400	92
2005	Cosmos 1	40	600	67
2010	IKAROS	310	196	1582
2010	NanoSail-D2	4	10	400
2013	Sunjammer	44	1208	36
2013*	Gossamer-1	20	25	800
2014*	Gossamer-2	57	400	143
2015*	Gossamer-3	80	2500	32
2015	Lightsail-1	4.9	32	140
2018*	NEA Scout	14	86	163

: Cubesat

\* : Not sent to orbit yet (original/expected launch date)

improvement can be appreciated in Figure 2.4, where the required sail loading parameters and sail surface areas of different sailcraft mission concepts are given [Herbeck et al., 2002, p.2].

Strictly related to the achievable loading parameter is the choice of the materials to use to manufacture solar sails, which should be highly reflective to sunlight while being lightweight. Usually the most used materials for the sail films are Kapton and Mylar, even though the former is on average more exploited as it provides a high resistance to radiation in a wide range of frequencies, as well as to high temperatures [McInnes, 1999, pp.61-62]. On the other hand, the most used sail coating material is aluminium, as it provides a good reflectivity in the visible spectrum (in the order of 0.88 – 0.9) and has a low density [McInnes, 1999, pp.62-63].

Concerning laser-enhanced solar sailing, no ground test nor in-space demonstration has ever been conducted yet, although some mission concepts have already been conceived. Such preliminary studies have been focusing mainly on missions to the outer Solar System or to close stellar systems like Alpha Centauri but, in spite of the advantages this propulsion system may provide, at present such missions are still unfeasible. Several issues prevent the practical use of laser-propelled sailcraft. The most challenging ones concern the high amount of laser power required, the sail material (which should withstand degradation while being highly-reflective with respect to both the solar and laser radiation), the huge laser-collimating lens, the sail dimensions, and the high laser beam pointing accuracy required, especially for missions to the outer Solar System. One way to measure this pointing accuracy is through the so-called jitter angle  $j$ , which is defined as the average angular distance displacement between the real direction of the beam and the nominal (intended) one. The graph provided in Figure 2.5 (adapted from [Taylor et al., 2003, p.375]) gives the maximum allowed jitter angle as a function of the LS-sailcraft distance  $s$  for a sail having a diameter of 1 km. As can be seen, for missions inside the Solar System ( $s \leq 50$  AU), the required

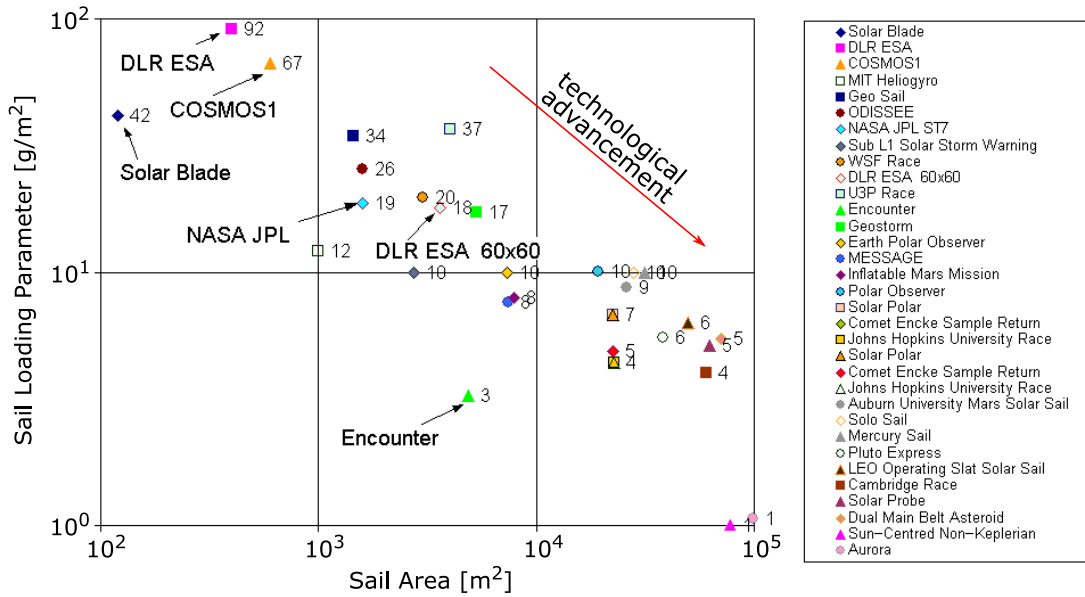


Figure 2.4: Sail areas and loading parameters of different sailcraft concepts [Herbeck et al., 2002, p.2].

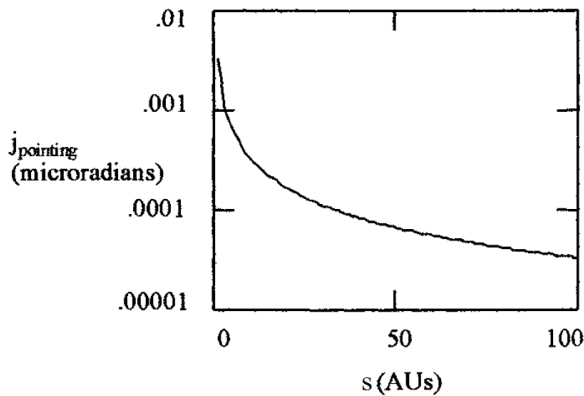


Figure 2.5: Maximum jitter angle as a function of the laser source-sailcraft distance for a circular solar sail with diameter of 1 km (adapted from [Taylor et al., 2003, p.375]).

jitter angle shall be at least in the range  $10^{-10} - 10^{-8}$  rad, although even more stringent accuracies are required for sails with smaller dimensions. It should be noted that, in comparison, the pointing accuracy required for the Hubble Space Telescope to operate was  $7.0 \cdot 10^{-3}$  arcsec  $\approx 3.4 \cdot 10^{-8}$  rad [Beals et al., 1988, p.119], while the line-of-sight stabilization of the James Webb Space Telescope to be launched in 2018 will be smaller than  $7.3 \cdot 10^{-3}$  arcsec  $\approx 3.5 \cdot 10^{-8}$  rad [eoPortal, b, 2017].

In case the above-mentioned problems related to laser-enhanced solar sailing were to be addressed, this propulsion method could allow the performing of missions that would otherwise be unfeasible using other propulsion systems. The substantial advantages given by laser-enhanced solar sailing in terms of achievable travel distances are summarized (to a first approximation) in Figure 2.6, in which are also presented the expected sail diameters and loading parameters to be achieved in the future [Johnson, 2016, p.36]. This figure shows that currently the "mid-term" development phase is taking place, which is indeed characterized by sail areal density and sail dimension ranges as the ones of the latest solar sailing projects presented in Table 2.1. From 2025

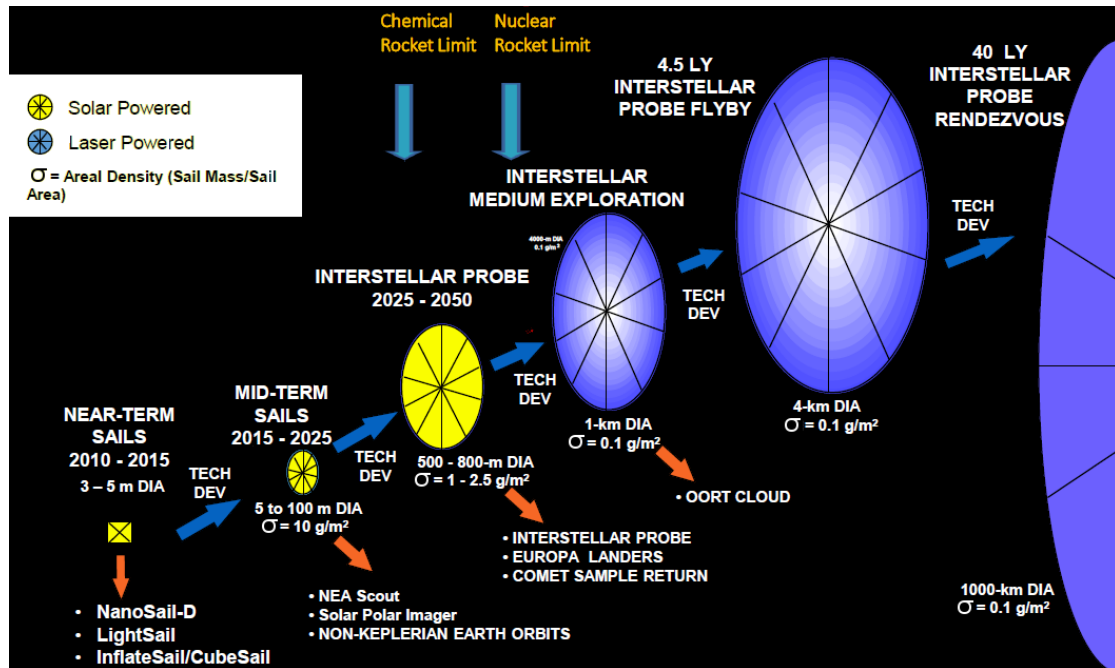


Figure 2.6: Direction of technological advancement and characteristics of traditional and laser-enhanced sailcraft in the future. In this picture DIA indicates the sail diameter, while  $\sigma$  the sail areal density [Johnson, 2016, p.36].

onward sailcraft to be used for interstellar missions might already start being designed, while in the 2050s the first laser-enhanced solar sails having a  $\sigma$  smaller than  $1 \text{ gm}^{-2}$  might be manufactured and put to test. Since such a small  $\sigma$  value has the same order of magnitude as the critical sail loading parameter  $\sigma^*$  (defined in Subsection 3.8.1), the SRP acceleration and solar gravitational acceleration will equally have the same order of magnitude, therefore making traditional and laser-enhanced solar sailing supersede chemical and nuclear propulsion in terms of providable velocity increment and achievable travel distances.



# 3

## MATHEMATICAL MODEL

In this chapter all mathematical concepts used to model the sailcraft dynamics are provided. To this aim, the most relevant reference frames, coordinate systems, sail models and perturbing forces are presented so that, based on these, the equations of motion (EoM) of traditional and laser-enhanced solar sails are eventually provided.

### 3.1. REFERENCE FRAMES

In describing the motion of a satellite, a crucial role is played by the choice of the reference frame because, depending on the reference frame and coordinate system used, the EoM describing the satellite's dynamics can be made more or less complex, and with them also the entire mathematical treatment of the problem.

Before presenting the orbital and J2000 heliocentric ecliptic frames of reference used throughout this report, it is convenient to define two classes of reference frames: the inertial and pseudo-inertial ones. In general, a reference frame is an inertial one in the case Newton's first law holds inside of it. This means that when the motion is described within these frames, no apparent forces have to be taken into account, therefore facilitating the orbital dynamics mathematical description. In a similar fashion, inside the so-called pseudo-inertial reference frames some apparent forces do exist which, however, can be neglected if compared to the other ones characterizing the S/C dynamics [Wakker, 2015, p.42]. As a consequence, such frames can be treated as if they were "purely" inertial.

#### 3.1.1. J2000 HELIOCENTRIC ECLIPTIC REFERENCE FRAME

This reference frame (which will be referred to with the symbol  $\mathcal{S}$ ) comes in useful especially when describing interplanetary trajectories. It is a pseudo-inertial frame that, as the name suggests, is centered in the Sun and has its  $XY$ -plane coincident with the ecliptic plane of the 1<sup>st</sup> January 2000 (J2000). More specifically, the  $X$ -axis is defined by the intersection of the Earth mean equatorial plane and the ecliptic plane at J2000, and points towards the so-called "first point of Aries" (indicated as  $\Upsilon$ ), i.e. the Earth-Sun direction at the vernal equinox [Mazzini, 2016, p.12]. The  $Z$ -axis is directed perpendicularly with respect to the ecliptic plane and points to the ecliptic north pole, forming

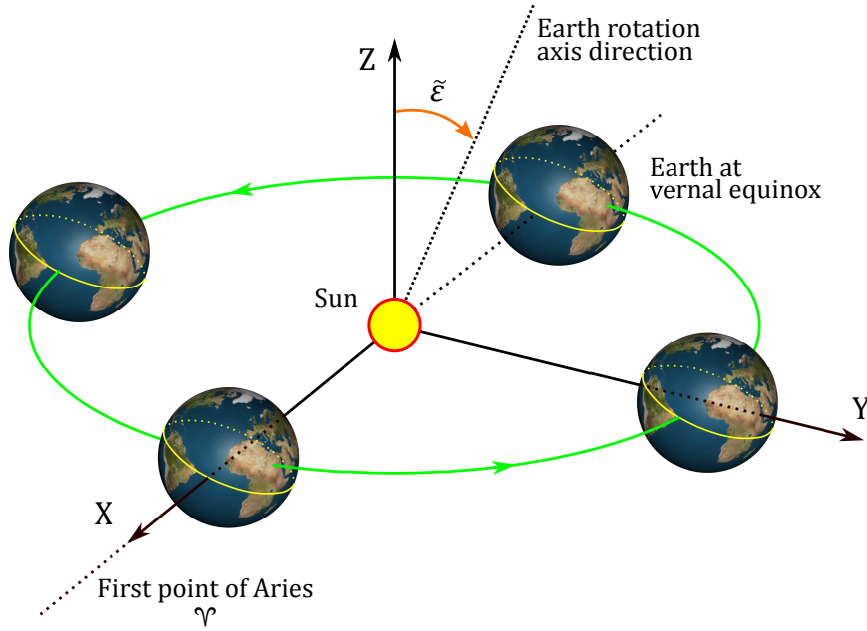


Figure 3.1: Representation of the J2000 heliocentric ecliptic reference frame.

an angle  $\tilde{\epsilon}$  with the J2000 Earth rotation axis equal to 23.439279 deg, also known as the obliquity of the ecliptic [Wakker, 2015, p.671]. Finally the Y-axis is chosen to form a right-handed frame.

A graphic representation of the J2000 heliocentric ecliptic frame of reference is given in Figure 3.1.

### 3.1.2. ORBITAL REFERENCE FRAME

The orbital reference frame (which will be referred to with the symbol  $\mathcal{O}$ ) is mainly used to express the SRP and LRP accelerations defined onto the sail, rather than to describe the orbital motion. In fact by using this frame the solar sail acceleration components can be directly related to the sail pitch and clock attitude angles defined in the next section.

This reference frame is centered in the sailcraft center of mass (CM), meaning that, as the sailcraft orbits around the Sun, the frame also rotates. Consequently, non-negligible apparent forces are also present and this frame cannot be considered a pseudo-inertial one.

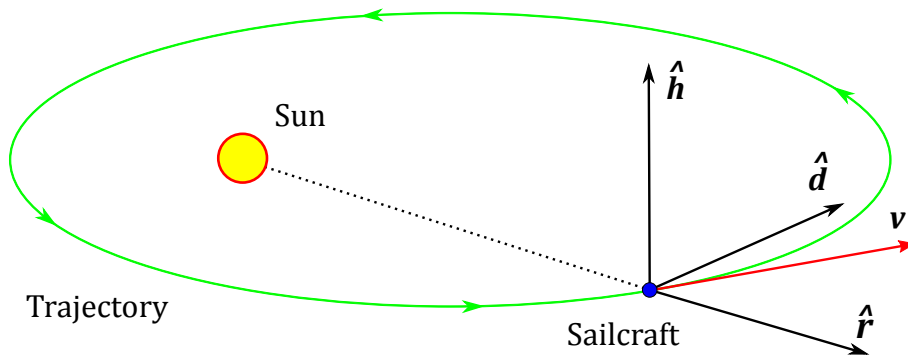


Figure 3.2: Representation of the orbital reference frame.

The reference frame is defined by means of three unit vectors: the radial unit vector  $\hat{r}$  pointing in the Sun-S/C direction, the angular momentum unit vector  $\hat{h}$  pointing along the instantaneous sailcraft's angular momentum vector, and the transversal unit vector  $\hat{d}$ , chosen such that  $\hat{r} \times \hat{d} = \hat{h}$  (hence forming a right-handed reference frame) [Dachwald, 2010, p.2]. In this way the velocity vector  $\mathbf{v}$  lies always in the plane defined by the unit vectors  $\hat{r}$  and  $\hat{d}$ , which indeed is the instantaneous orbital plane. A graphic representation of this reference frame is shown in Figure 3.2.

## 3.2. COORDINATES SYSTEMS

Within the above-presented orthogonal right-handed reference frames different coordinate systems can be used to express the position, velocity or the entire orbit of a satellite. Among the most commonly used coordinate systems are the Cartesian and spherical ones, as well as the Keplerian and modified equinoctial elements which are used exclusively for astrodynamics applications.

Since these coordinate systems will be used to describe solar sailing trajectories within this report, they are presented in this section together with the angles and vectors used to characterize the sailcraft attitude and thrust. On the other hand, only one of these coordinate sets will be exploited to write the EoM and, in particular, such a choice of the most suitable coordinate system will be carried out in Subsection 3.8.2.

### 3.2.1. CARTESIAN COORDINATES

When using a Cartesian coordinate system the position of a point is uniquely identified by the  $x$ ,  $y$  and  $z$  spatial coordinates. These represent the distance between the reference frame origin  $O$  and the projection of the point on the three frame axes, as shown in Figure 3.3. The main advantage of Cartesian coordinates is that they can be easily used to express the S/C state and do not suffer from singularities.

### 3.2.2. SPHERICAL COORDINATES

In this case the position of a point is identified by means of one spatial coordinate, the range  $r$ , and two angles, the azimuth  $\theta$  and polar angle  $\phi$  (also known as elevation). The range is simply the distance between the reference frame origin  $O$  and the des-

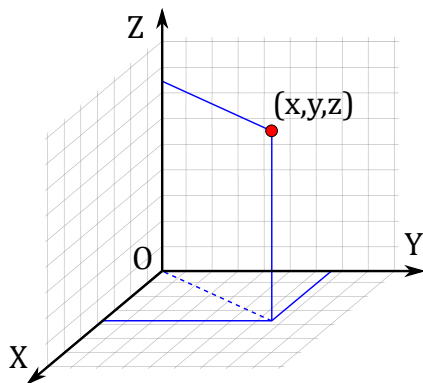


Figure 3.3: Visualization of a point's Cartesian coordinates.

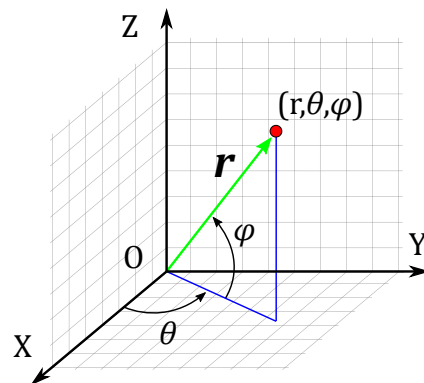


Figure 3.4: Visualization of a point's spherical coordinates.

ignated point, or, alternatively, the magnitude of the position vector  $\mathbf{r}$ . As shown in Figure 3.4, the polar angle lies between  $\mathbf{r}$  and the reference frame  $XY$ -plane, whereas the azimuth  $\theta$  is defined as the angle between the  $X$ -axis and the projection of  $\mathbf{r}$  on the  $XY$ -plane. As extensively discussed in [Carzana, 2017, pp.16-18] (based on [Hassani, 2008, pp.13-15]), the conversion from spherical coordinates to Cartesian ones and vice versa is obtained by exploiting the following relations:

$$\begin{cases} r = \sqrt{x^2 + y^2 + z^2} \\ \theta = \text{atan2}(y, x) \\ \phi = \text{asin}(z/r) \end{cases} \quad \begin{cases} x = r \cos\phi \cos\theta \\ y = r \cos\phi \sin\theta \\ z = r \sin\phi \end{cases} \quad (3.1)$$

where the  $\text{atan2}(y, x)$  function is used instead of  $\text{atan}(y/x)$  to solve for the quadrant ambiguity of the arctangent solution.

In the spherical coordinate system the unit vectors  $\hat{\mathbf{r}}$ ,  $\hat{\boldsymbol{\theta}}$  and  $\hat{\boldsymbol{\phi}}$  shown in Figure 3.5 are commonly used. When inside a Cartesian  $\mathcal{F}$ -frame (hereafter indicated as  $\mathcal{F}_c$ ), their expressions are given by [Dachwald, 2004, p.122]:

$$\begin{cases} \hat{\mathbf{r}} = [\cos\theta \cos\phi, \sin\theta \cos\phi, \sin\phi]^T \\ \hat{\boldsymbol{\theta}} = [-\sin\theta, \cos\theta, 0]^T \\ \hat{\boldsymbol{\phi}} = [-\cos\theta \sin\phi, -\sin\theta \sin\phi, \cos\phi]^T \end{cases} \quad (3.2)$$

so that through differentiation the following is found:

$$\begin{cases} \frac{d\hat{\mathbf{r}}}{dt} = \dot{\phi}\hat{\boldsymbol{\phi}} + \cos\phi \dot{\theta}\hat{\boldsymbol{\theta}} \\ \frac{d\hat{\boldsymbol{\theta}}}{dt} = -\dot{\theta}[\cos\phi \hat{\mathbf{r}} - \sin\phi \hat{\boldsymbol{\phi}}] \\ \frac{d\hat{\boldsymbol{\phi}}}{dt} = -\dot{\phi}\hat{\mathbf{r}} - \sin\phi \dot{\theta}\hat{\boldsymbol{\theta}} \end{cases} \quad (3.3)$$

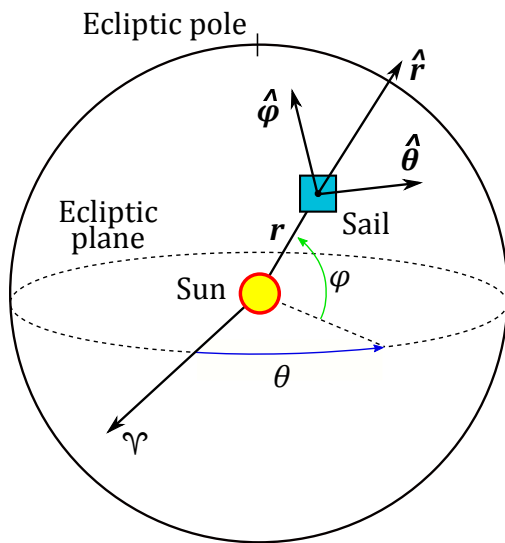


Figure 3.5: Representation of the spherical coordinates and related unit vectors inside the  $\mathcal{F}$ -frame.

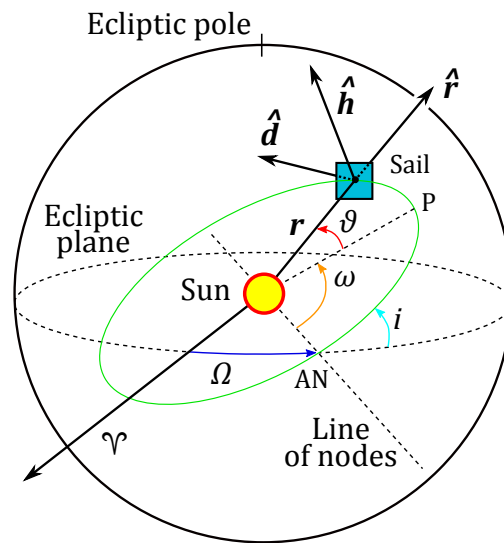


Figure 3.6: Representation of the Keplerian elements and orbital frame unit vectors inside the  $\mathcal{F}$ -frame.

Equations 3.2 and 3.3 will come in useful to define the EoM in spherical coordinates, as discussed in Subsection 3.8.3.

### 3.2.3. KEPLERIAN ELEMENTS

Keplerian elements (also known as "orbital elements") are particularly suited to describe the S/C motion because they can give information not only about a satellite's position, but also about its entire orbit in terms of dimension, shape and orientation. More specifically the semi-major axis  $a$  is directly related to the dimension and specific energy of the orbit, whereas the eccentricity  $e$  is used to express the orbit's oblateness, i.e. how much it deviates from being circular. The orbit orientation in space is determined by the inclination  $i$ , argument of pericenter  $\omega$  and right ascension of the ascending node (RAAN)  $\Omega$ .  $i$  Is defined as the angle between the orbital plane and reference frame  $XY$ -plane. For instance, the latter plane would be the ecliptic one if an  $\mathcal{S}$ -frame were used. Defining the ascending node (AN) as the point along the orbit where the S/C passes from the southern ( $z < 0$ ) to the northern ( $z > 0$ ) hemisphere of the reference frame,  $\omega$  represents the angle lying between the pericenter and the AN direction (as seen from the reference frame origin).  $\Omega$  Is the angle between the reference frame  $X$ -axis (the  $\Uparrow$ -direction inside the  $\mathcal{S}$ -frame) and the line of nodes, where also the AN is placed. Eventually the true anomaly  $\vartheta$  is used to exactly determine the position of the S/C along the orbit and is defined as the angular distance between the pericenter and the S/C, as seen from the frame origin [Wakker, 2015, pp.260-261]. A sketch showing a sailcraft orbit inclination, argument of pericenter, RAAN and true anomaly is provided in Figure 3.6.

It should be noted that, in certain cases, depending on the type of trajectory to be analyzed the S/C position along the orbit can also be expressed by means of the argument of pericenter  $u = \omega + \vartheta$  or the true longitude  $L = \Omega + u = \Omega + \omega + \vartheta$  instead of the true anomaly [Wakker, 2015, p.262]. Moreover, just as for spherical coordinates, also orbital elements can be expressed in terms of Cartesian coordinates and vice versa. For the procedure to be used to achieve this the reader is referred to [Wakker, 2015, pp.268-274,276-278].

### 3.2.4. MODIFIED EQUINOCTIAL ELEMENTS

Modified equinoctial elements represent an alternative to orbital elements and, not by chance, they can be defined by means of the latter as follows [Falck and Dankanich, 2012, pp.6-7]:

$$\left\{ \begin{array}{l} p = a(1 - e^2) \\ f = e \cos(\omega + \Omega) \\ g = e \sin(\omega + \Omega) \\ h = \tan(i/2) \cos\Omega \\ k = \tan(i/2) \sin\Omega \\ L = \Omega + \omega + \vartheta \end{array} \right. \quad (3.4)$$

where  $p$  represents the semi-latus rectum and  $L$  the already mentioned true longitude. Unlike Keplerian elements, most of the variables of this coordinate set do not have a straightforward physical meaning but, on the other hand, they lead to EoM (the Lagrange planetary equations) that become singular only for  $i = 180$  deg, and even in

these cases specific variables re-definitions can be exploited to avoid such inconveniences [Walker, 1986, p.410].

### 3.2.5. SOLAR SAIL ATTITUDE VECTORS AND ANGLES

As in solar sailing the sunlight represents the S/C thrust source, it is useful to describe the attitude of solar sails with respect to the Sun-line, i.e. Sun-S/C direction. By doing so the thrust magnitude and direction can be defined in a straightforward way, as done hereafter (see Figures 3.7a and 3.7b, based on [Dachwald, 2004, p.8]).

By taking advantage of the orbital reference frame presented in Subsection 3.1.2, the attitude of a flat ideal sail can be unequivocally defined by means of two angles: the sail pitch angle  $\alpha$  and clock angle  $\delta$ . The pitch angle is the angle between the sail normal unit vector  $\hat{n}$  (which, by definition, points always away from the Sun) and the sunlight direction  $\hat{r}$ , whereas  $\delta$  lies between the transversal unit vector  $\hat{d}$  and clock unit vector  $\hat{p}$ , i.e. the projection of  $\hat{n}$  on the plane perpendicular to the Sun line. The SRP thrust direction  $\hat{f}_S$  is identified through the cone angle  $\theta$ , i.e. the angle between  $\hat{r}$  and  $\hat{f}_S$ .

The angles and vectors presented above can be used to unequivocally determine the attitude and thrust of a solar sail. However, in the case a laser-enhanced sailcraft is considered, also the laser pitch angle  $\alpha_L$  and laser cone angle  $\theta_L$  shall be defined.

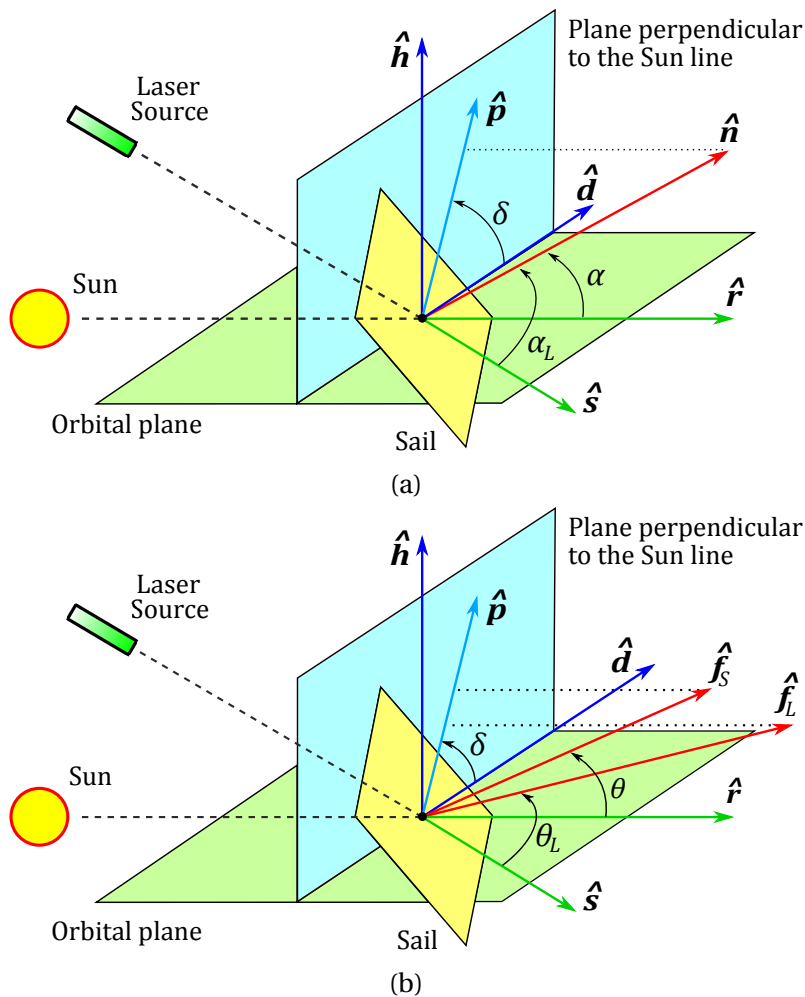


Figure 3.7: Angles and vectors used to describe the attitude of a (laser-enhanced) solar sail (based on [Dachwald, 2004, p.8]).

Similarly to a traditional solar sail,  $\alpha_L$  represents the angle between the LS-S/C direction  $\hat{\mathbf{s}}$  and  $\hat{\mathbf{n}}$ , while  $\theta_L$  is the angle between  $\hat{\mathbf{s}}$  and laser thrust unit vector  $\hat{\mathbf{f}}_L$ .

As will be seen in Subsection 3.6.1, in the case an ideal sail is used, the SRP and LRP forces are assumed to be pointing always in the  $\hat{\mathbf{n}}$  direction, hence yielding  $\alpha = \theta$  and  $\alpha_L = \theta_L$  always. Moreover, while  $\alpha$  (or  $\alpha_L$ ) has a strong influence on the thrust magnitude exerted onto the sail, the clock angle  $\delta$  assumes a great importance to determine the direction the sail should head to. In this regard it is useful to look at Figure 3.8 (modified after [Dachwald, 2004, p.12]), which shows that for  $\delta$  in the order of 0 or 180 deg, a solar sail can spiral outwards or inwards the Solar System, respectively. This result will come in useful to analyze the sailcraft trajectories presented in Chapter 7.

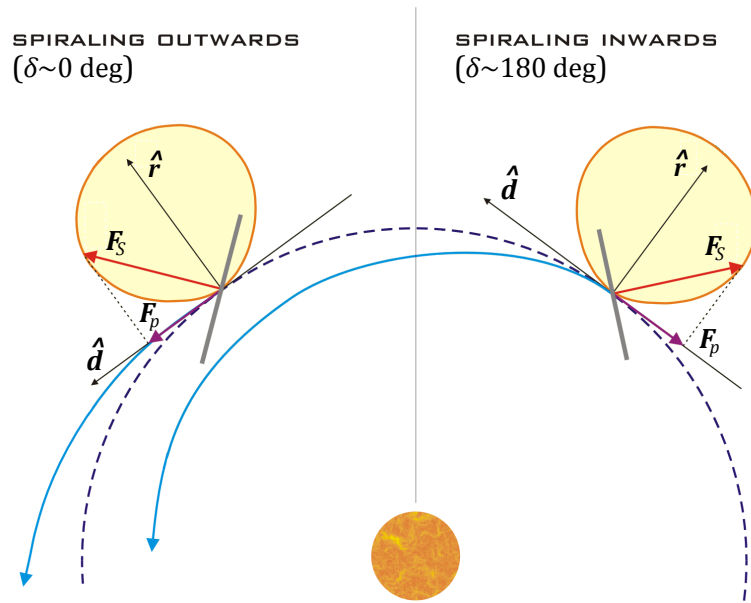


Figure 3.8: Visualization of the sail attitudes and related thrust vectors defining inward and outward spiral trajectories (modified from [Dachwald, 2004, p.12]).

### 3.3. REFERENCE FRAME TRANSFORMATIONS

Reference frame transformations are used when the need of expressing a vector inside another reference frame arises. In this section two different techniques to fulfill this task are presented, while their accuracies and computational efficiencies have been tested directly through the software used for trajectory optimization, as discussed in Section 5.3. All frame transformation techniques shown hereafter assume that the initial frame  $\mathcal{T}_A$  and final frame  $\mathcal{T}_B$  share the same origin, meaning that, if this is not the case, a reference frame translation shall be performed beforehand to make such frames' origins coincide.

#### 3.3.1. ROTATION MATRIX-BASED METHOD

Given an arbitrary vector  $\mathbf{v}_A$  inside  $\mathcal{T}_A$ , one way of retrieving its new expression  $\mathbf{v}_B$  inside  $\mathcal{T}_B$  is by performing a maximum of three consecutive frame axis rotations to transform  $\mathcal{T}_A$  into  $\mathcal{T}_B$ . In particular, each of these rotations can be modeled through

one of the following rotation matrices [De Marco and Coiro, 2016a, p.9]:

$$R(1, \mu) = \begin{bmatrix} 1 & 0 & 0 \\ 0 & C_\mu & S_\mu \\ 0 & -S_\mu & C_\mu \end{bmatrix} \quad R(2, \mu) = \begin{bmatrix} C_\mu & 0 & -S_\mu \\ 0 & 1 & 0 \\ S_\mu & 0 & C_\mu \end{bmatrix} \quad R(3, \mu) = \begin{bmatrix} C_\mu & S_\mu & 0 \\ -S_\mu & C_\mu & 0 \\ 0 & 0 & 1 \end{bmatrix} \quad (3.5)$$

with  $R(k, \mu)$  being the rotation matrix,  $k = \{1, 2, 3\}$  indicating the axis about which the rotation is performed (1, 2 and 3 correspond to the  $X$ -,  $Y$ - and  $Z$ -axis, respectively),  $\mu$  being the rotation angle,  $S_\mu = \sin \mu$  and  $C_\mu = \cos \mu$  [De Marco and Coiro, 2016a, pp.7-8]. By using this formulation, in [De Marco and Coiro, 2016a, pp.8-9] it is proven that consecutive axis rotations can be mathematically expressed through consecutive multiplications of the matrices  $R(k, \mu)$ , hence resulting in a so-called direction cosine matrix (DCM)  $T$ . Eventually such a matrix can be exploited to express the vector  $\mathbf{v}_B$  inside  $\mathcal{T}_B$  as [De Marco and Coiro, 2016a, p.9]:

$$\mathbf{v}_B = \prod_{i=1}^3 R(k_i, \gamma_i) \mathbf{v}_A = T_{AB} \mathbf{v}_A \quad (3.6)$$

with  $k_i$  representing the rotation axis identifiers and  $\gamma_i$  the so-called Euler's angles.

### 3.3.2. QUATERNION-BASED METHOD

Besides rotation matrices, also quaternions can be successfully used to rotate a reference frame. In this case, however, the formulation of the rotation problem is slightly different and is based on the Euler's rotation theorem, which states that "any displacement of a rigid body such that a point on the rigid body, say  $O$ , remains fixed, is equivalent to a rotation about a fixed axis through the point  $O$ " [Kumar, 2000, p.1]. As a direct consequence of this theorem it holds true that a generic vector  $\mathbf{v}_A$  inside  $\mathcal{T}_A$  can be transformed into  $\mathbf{v}_B$  inside  $\mathcal{T}_B$  once a rotation axis unit vector  $\hat{\mathbf{e}} = [e_x, e_y, e_z]^T$  and a rotation angle  $\mu$  are provided, as graphically shown in Figure 3.9 (based on [De Marco and Coiro, 2016b, p.7]).

Besides the above-presented formulation, another way of expressing the frame rotation problem is to use the so-called Euler-Rodrigues parameters, which represent the

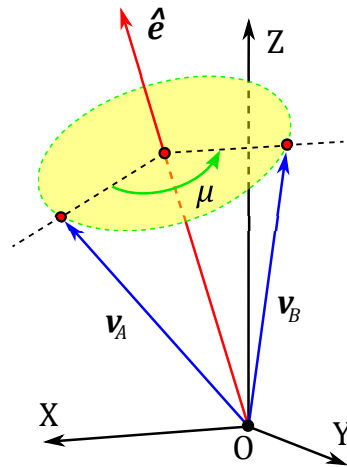


Figure 3.9: Use of the axis-angle formulation to retrieve the  $\mathbf{v}_B$  vector inside the rotated frame from  $\mathbf{v}_A$  given in the initial frame (based on [De Marco and Coiro, 2016b, p.7]).

components of the finite rotation quaternion  $\mathbf{q}$  defined as [De Marco and Coiro, 2016b, p.11]:

$$\mathbf{q} = [q_0, q_x, q_y, q_z]^T = [\cos(\mu/2), e_x \sin(\mu/2), e_y \sin(\mu/2), e_z \sin(\mu/2)]^T \quad (3.7)$$

In spite of not having a straightforward physical meaning, the quaternion  $\mathbf{q}$  contains all the information required to perform the frame rotation and, in particular, it can be demonstrated (see [Janota et al., 2015, pp.7021-7022]) that the following equation holds for retrieving the rotated vector  $\mathbf{v}_B$  from  $\mathbf{v}_A$ :

$$\mathbf{v}_B = \mathbf{v}_A + 2 \cdot \hat{\mathbf{q}} \times [\mathbf{v}_A q_0 + (\hat{\mathbf{q}} \times \mathbf{v}_A)] \quad (3.8)$$

with  $\hat{\mathbf{q}} = [q_x, q_y, q_z]^T = \hat{\mathbf{e}} \sin(\mu/2)$  [Janota et al., 2015, p.7022].

### 3.4. SOLAR RADIATION PRESSURE MODELS

#### 3.4.1. POINT-LIKE SOLAR RADIATION PRESSURE MODEL

What makes a solar sail experience a tiny acceleration when illuminated by sunlight is the SRP acting onto the sail which in turn is due to the momentum exchange that takes place between the solar photons and the sail itself. In the case a black body is considered (i.e. a body ideally capable of absorbing all radiation illuminating it), the momentum provided by the photons is equal to [French, 1968, p.202]:

$$p = \frac{\mathcal{E}}{c} \quad (3.9)$$

with  $c = 2.99792458 \cdot 10^8 \text{ ms}^{-1}$  and  $\mathcal{E}$  being the speed of light in vacuum [NIST, 2017] and the solar radiation energy, respectively. Furthermore, through differentiation of Equation 3.9 the force associated to such radiation is found as:

$$F_S = \frac{1}{c} \frac{d\mathcal{E}}{dt} \quad (3.10)$$

When the entire amount of radiation emitted by the Sun is considered,  $d\mathcal{E}/dt$  represents the total solar radiative power (i.e. the solar luminosity  $\mathcal{L}_\odot = 3.828 \cdot 10^{26} \text{ W}$  [NASA, 2017c]), whereas  $F_S$  is the total explicable force related to such radiation. If the Sun is considered as a point-like radiation source, the solar power can be assumed to be radially emitted in space. In this case the solar radiation pressure  $P_S$  defined by  $F_S$  is constant for a given heliocentric distance  $r$  and therefore is evenly distributed over spheres having a surface of  $4\pi r^2$ . Hence the following holds [Lissauer and De Pater, 2013, p.54]:

$$P_S = \frac{F_S}{4\pi r^2} = \frac{1}{4\pi r^2} \cdot \frac{1}{c} \frac{d\mathcal{E}}{dt} = \frac{\mathcal{L}_\odot}{4\pi r^2 c} \quad (3.11)$$

and since by definition the solar flux is given by [Dodelson, 2003, p.35]:

$$S = \frac{\mathcal{L}_\odot}{4\pi r^2} \quad (3.12)$$

the SRP can be also expressed in a more compact way as:

$$P_S = \frac{S}{c} \quad (3.13)$$

Even though Equation 3.13 can already be used to compute the SRP at whichever distance from the Sun, in practice a different form of the same equation is usually exploited, which is found as follows [Dachwald, 2004, p.8]:

$$\mathcal{L}_{\odot} = S \cdot 4\pi r^2 = S_0 \cdot 4\pi r_0^2 \implies S = S_0 \left[ \frac{r_0}{r} \right]^2 \implies P_S = P_0 \left[ \frac{r_0}{r} \right]^2 \quad (3.14)$$

where

$$S_0 = \frac{\mathcal{L}_{\odot}}{4\pi r_0^2} = 1368 \text{ Wm}^{-2} \quad (3.15)$$

$$P_0 = \frac{S_0}{c} = 4.563 \cdot 10^{-6} \text{ Nm}^{-2} \quad (3.16)$$

In the above equations  $r_0 = 1 \text{ AU} = 1.49597870700 \cdot 10^{11} \text{ m}$  is the mean Sun-Earth distance [Wakker, 2015, p.671],  $P_0 = 4.563 \cdot 10^{-6} \text{ Nm}^{-2}$  is the SRP at Earth [Dachwald, 2004, p.8] and  $S_0 = 1368 \text{ Wm}^{-2}$  is the solar flux intercepted at Earth, also known as solar constant [Beatty et al., 1981, p.36].

### 3.4.2. FINITE SOLAR DISK SOLAR RADIATION PRESSURE MODEL

As already mentioned, the hypothesis on which the point-like SRP model is based is indeed that of assuming the Sun to be a point-like radiation source. At first glance, such an assumption seems realistic when  $r \gg R_{\odot} = 6.95700 \cdot 10^8 \text{ m}$  (with  $R_{\odot}$  being the mean solar radius [NASA, 2017c]), but this may not always be the case.

A more accurate model that takes into account the finite angular width of the solar disk as seen by the sailcraft is the so-called finite solar disk SRP model, whose extensive description is provided in [McInnes, 1999, pp.43-46] and [Rios-Reyes, 2006, pp.11-13]. Here the SRP of such a model is expressed as:

$$P_S = P_S^* \cdot \zeta \quad (3.17)$$

where

$$P_S^* = \frac{I_0 \pi}{c} \left( \frac{R_{\odot}}{r} \right)^2 \quad (3.18a)$$

$$\zeta = \frac{2}{3} \left( \frac{r}{R_{\odot}} \right)^2 \left\{ 1 - \left[ 1 - \left( \frac{R_{\odot}}{r} \right)^2 \right]^{\frac{3}{2}} \right\} \quad (3.18b)$$

In the above equations  $P_S^*$  is the point-like SRP,  $\zeta$  represents a factor that takes into account the solar disk finiteness effect on the SRP, while  $I_0$  is the solar specific intensity at Earth, equal to [Rios-Reyes, 2006, p.13]:

$$I_0 = \frac{\mathcal{L}_{\odot}}{4\pi^2 R_{\odot}^2} \quad (3.19)$$

### 3.4.3. CHOICE OF THE SOLAR RADIATION PRESSURE MODEL

In order to perform a first order analysis on the accuracy of the finite solar disk SRP model as compared to the point-like one, the parameter  $\zeta$  of Equation 3.18b can be

approximated through a Taylor series around the value  $(R_{\odot}/r) = 0$ , so that the following new expression is obtained [Rios-Reyes, 2006, p.13]:

$$\zeta = \frac{2}{3} \left( \frac{r}{R_{\odot}} \right)^2 \left[ 1 - 1 + \frac{3}{2} \left( \frac{R_{\odot}}{r} \right)^2 - O \left( \frac{R_{\odot}}{r} \right)^4 \right] = 1 - O \left( \frac{R_{\odot}}{r} \right)^2 \quad (3.20)$$

This equation shows that the error committed when using the point-like model instead of the finite solar disk one is  $O(R_{\odot}/r)^2$ . As expected, for  $r \rightarrow \infty$  it results  $\zeta \rightarrow 1$ , meaning that the SRPs given by the two models are equal. On the opposite, the difference between the SRPs becomes more evident as  $r$  decreases. A rapid analysis of this error variation with  $r$  shows that, however, even for a small orbital radius equal to Mercury's semi-major axis (i.e.  $a_{\text{Mer}} = 0.387099$  AU [Wakker, 2015, p.673]) the error is only 0.0145%, and gets even smaller for greater values of  $r$ . Since such an error is negligible and, furthermore, it is also an order of magnitude smaller than the solar flux short-time variability (which reaches maximum values equal to  $\sim 0.30\%$  on 27-day solar-rotation timescales [Kopp, 2016, p.4]), in the end it was decided to use for the present work a much simpler, yet accurate, point-like SRP model as this will not significantly affect the results achieved.

### 3.5. LASER RADIATION PRESSURE FORCE MODEL

By definition a laser beam is a concentrated beam of electromagnetic radiation having a unique wavelength. As for solar radiation, the laser photons illuminating the sail exchange momentum with it following the same physical mechanism discussed in Subsection 3.4.1, and therefore most of the considerations and conclusions drawn for the SRP are valid also for the LRP. However one major difference exists between the two, which is the region of space where the radiation is confined. In fact, while solar radiation propagates radially and isotropically in space, laser light is confined within a conical region of space that diverges in the direction of propagation. More specifically, the parameter determining how much the laser radiation diverges is the diffraction-limited divergence angle  $\theta$ , i.e the angle defining the cone within which 84% of the laser energy is confined [McInnes, 1999, p.272]. Hereafter such a conical region will be simply referred to as laser beam.  $\theta$  Can be expressed as a function of the laser wavelength  $\lambda$  and laser generator (LG) collimating lens diameter  $D$  as follows [McInnes, 1999, p.273][Moeckel, 1972, p.942]:

$$\theta \approx \sin\theta = 2.44 \frac{\lambda}{D} \quad (3.21)$$

By moving away from the LS the laser distance  $s$  increases and with it also the beam cross-section diameter  $d_L$ . Therefore, depending on the laser distance  $s$ , the laser beam may or may not impinge the sail entirely. In order to analyze these two circumstances, the concept of equivalent sail diameter  $d$  shall be introduced: given a sail with surface area  $A$ ,  $d$  is defined as the diameter such a sail would have if it were to be circular and were to keep the same area, i.e.:

$$d = 2\sqrt{\frac{A}{\pi}} \quad (3.22)$$

This value represents a characteristic length of the sail to be compared with the laser beam diameter in order to understand whether the sail is totally illuminated by the beam or not. In fact, by imposing  $d_L = d$  it is possible to calculate the critical laser distance  $\tilde{s}$ , which (for small divergence angles) results to be equal to [McInnes, 1999, p.274]:

$$\tilde{s} \approx \frac{d}{\theta} = \frac{dD}{2.44\lambda} \quad (3.23)$$

Given this result, the following holds: for distances  $s$  smaller than  $\tilde{s}$ , the laser beam impinges on the sail completely (if the two are oriented perpendicular with respect to each other), whereas beyond  $\tilde{s}$ , part of the beam energy is dispersed in space and not transferred to the sail, thus defining a smaller acceleration. Such a phenomenon is illustrated in Figure 3.10.

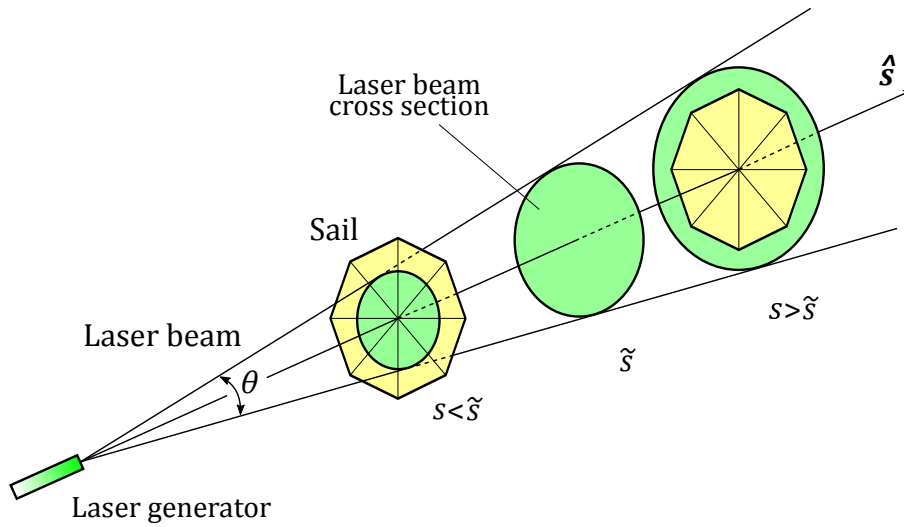


Figure 3.10: Representation of the laser beam cross-section area variation as compared to the sail dimensions.

In general, instead of  $d$  also other characteristic sail lengths could be considered for the comparison with the beam diameter  $d_L$ , which would yield slightly different values of  $\tilde{s}$ . However, in this work the sail equivalent diameter has been used as it represents a good characteristic length to consider for the general case (i.e. when no information on the sail shape is given).

As previously mentioned, the LRP exerted onto the sail (hereafter denoted with  $P_L$ ) can be computed in a similar fashion to the procedure explained in Subsection 3.4.1 for the SRP. In particular, Equation 3.10 can be readapted to this case by considering that the term  $d\mathcal{E}/dt$  now represents the optical laser power within the laser beam (hereafter referred to as  $W_L$ ), so that the maximum explicable LRP force is given by:

$$F_L = \frac{W_L}{c} \quad (3.24)$$

This result holds when the entire laser beam illuminates the sail ( $s \leq \tilde{s}$ ), hence transferring all of its energy to the sailcraft. In this case the average pressure acting on the sail is therefore found to be:

$$P_L = \frac{F_L}{A} = \frac{W_L}{Ac} \quad (3.25)$$

On the other hand, if the sail is totally illuminated and part of the laser beam is dispersed in space ( $s > \tilde{s}$ ), only a part of the total laser energy will be provided to the sail itself. This fraction of energy is proportional to the ratio of the sail area  $A$  to the laser beam cross section area  $A_L$ , meaning that the greater  $A_L$ , the less energy is transferred to the sail. Consequently, the following holds:

$$F_L = \frac{W_L}{c} \frac{A}{A_L} \quad (3.26)$$

and since

$$A_L = \pi \left( \frac{d_L}{2} \right)^2 \approx \pi \left( \frac{\theta s}{2} \right)^2 \quad (3.27a)$$

$$A = \pi \left( \frac{d}{2} \right)^2 \approx \pi \left( \frac{\theta \tilde{s}}{2} \right)^2 \quad (3.27b)$$

the following expressions for  $F_L$  and  $P_L$  are found for  $s > \tilde{s}$ :

$$F_L = \frac{W_L}{c} \left( \frac{\tilde{s}}{s} \right)^2 \quad (3.28)$$

$$P_L = \frac{F_L}{A} = \frac{W_L}{Ac} \left( \frac{\tilde{s}}{s} \right)^2 \quad (3.29)$$

By defining the laser power provision coefficient  $\xi$ , Equations 3.25 and 3.29 can be rewritten into one as follows:

$$P_L = \frac{W_L}{Ac} \xi^2 \quad \text{with} \quad \begin{cases} \xi = 1 & \text{for } s \leq \tilde{s} \\ \xi = \tilde{s}/s & \text{for } s > \tilde{s} \end{cases} \quad (3.30)$$

so that, by implementing also the LG throttle  $\chi$  (equal to 0 or 1 if the LG is respectively powered off or on), the following is found:

$$P_L = \chi \frac{W_L}{Ac} \xi^2 \quad (3.31)$$

As will be seen in Subsection 3.8.1, the above result is in accordance with [McInnes, 1999, pp.271-278], in which the laser-driven lightsail dynamics is discussed in detail. As previously mentioned, the term  $W_L$  given in the above equation represents the optical power confined inside the laser beam. Hence by assuming that the total power emitted by the LG in the form of radiation is  $W_{LG}^{out}$ , it results:

$$W_L = 0.84 W_{LG}^{out} \quad (3.32)$$

Furthermore, the output laser power  $W_{LG}^{out}$  depends on the LG electrical input power  $W_{LG}^{in}$  and wall-plug efficiency  $\eta_{wp}$  (i.e. “the ratio of optical output power to consumed electrical input power” [RP Photonics Encyclopedia, 2017]) as follows:

$$W_{LG}^{out} = \eta_{wp} W_{LG}^{in} \quad (3.33)$$

so that  $W_L$  can eventually be expressed as:

$$W_L = 0.84 \eta_{wp} W_{LG}^{in} \quad (3.34)$$

The LRP model given in Equation 3.31 will be used to compute the LRP thrust taking advantage of two main simplifications:

- The laser beam direction of propagation is always rectilinear and does not bend due to the presence of massive gravity fields as the solar one. Such an assumption has been exploited mainly to lower the computational burden of the simulations, despite it should be taken into account for real missions and especially in the case the laser beam is pointed relatively close to the solar disk. For the sake of comparison, it should be noted that the divergence angles of the laser beams exploited in the simulations provided in this work are equal to  $\sim 2.23 \cdot 10^{-6}$  deg, whereas in [Carzana, 2017, p.57] the deflection angle of a laser beam "touching" the solar surface (worst-case scenario) is shown to be  $\sim 4.4 \cdot 10^{-4}$  deg, i.e. about 200 times bigger.
- The laser light travels infinitely fast between the LS and the sailcraft, meaning that no delay is present due to the finiteness of the speed of light. As for the previous assumption, also this one has been taken into account mainly with a view to reducing the optimizations computational effort, although this "delay effect" shall be considered when designing real sailcraft missions.

If the above assumptions were not considered, the laser beam trajectory would be slightly deflected by the solar gravitational field, hence resulting in a slightly different laser distance and laser pitch angle. However, due to the small order of magnitude of the laser beam deflection angle, such differences would not affect the LRP significantly and, therefore, the use of the above-discussed simplification will not affect the results considerably.

### 3.6. RADIATION PRESSURE FORCE MODELS

In this section the most commonly used radiation pressure force models (also referred to as sail models) will be described, with a view to determining the best one to adopt for carrying out the traditional and laser-enhanced solar sailing optimizations within this work. In the following subsections the thrust will always be expressed by considering the Sun as only radiation source, meaning that the sunlight incidence angle  $\alpha$  and SRP will be considered inside the equations. However, it should be noted that such equations are valid also if a laser beam is considered instead of the Sun. In fact, in the latter case all equations found can be re-used simply by substituting the  $P_S$  and  $\alpha$  terms in the equations respectively with  $P_L$  and  $\alpha_L$ .

The sail models discussed in this section are always assumed to be flat (except for the generalized sail model) and do not degrade over time.

#### 3.6.1. IDEAL REFLECTION MODELS

##### BASIC IDEAL REFLECTION MODEL

As described in Subsection 3.4.1, when the sunlight illuminates a black body the momentum carried by the photons is totally transferred to the black body itself, yielding an SRP and hence a tiny force. In a similar fashion, such a momentum transfer mechanism takes place also when a flat and totally reflecting sail is considered, even though with some major differences. As shown in Figure 3.11 (adapted after [Dachwald, 2004, p.9]), in this case the total generated force is due both to the incident and reflected sunlight, whose force contributions are respectively given by:

$$\mathbf{F}_r = P_S A (\hat{\mathbf{r}} \cdot \hat{\mathbf{n}}) \hat{\mathbf{r}} = P_S A \cos \alpha \hat{\mathbf{r}} \quad (3.35)$$

and

$$\mathbf{F}_{r'} = -P_S A (\hat{\mathbf{r}} \cdot \hat{\mathbf{n}}) \hat{\mathbf{r}}' = -P_S A \cos \alpha \hat{\mathbf{r}}' \quad (3.36)$$

with  $A$ ,  $\hat{\mathbf{r}}$  and  $\hat{\mathbf{r}}'$  representing the sail surface area, radial unit vector and unit vector in the direction of reflected sunlight [Dachwald, 2004, p.9].

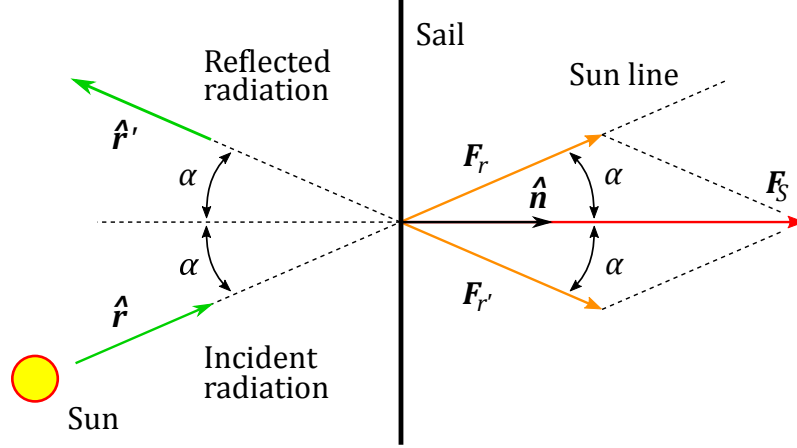


Figure 3.11: SRP force generated when the sunlight illuminates a flat ideal solar sail (adapted from [Dachwald, 2004, p.9]).

The total SRP force  $\mathbf{F}_S$  acting upon the sail is therefore given by the sum of these two vectors:

$$\mathbf{F}_S = \mathbf{F}_r + \mathbf{F}_{r'} = P_S A (\hat{\mathbf{r}} \cdot \hat{\mathbf{n}}) (\hat{\mathbf{r}} - \hat{\mathbf{r}}') \quad (3.37)$$

which, by using the relations  $\hat{\mathbf{r}} - \hat{\mathbf{r}}' = 2(\hat{\mathbf{r}} \cdot \hat{\mathbf{n}}) \hat{\mathbf{n}}$  and  $\hat{\mathbf{r}} \cdot \hat{\mathbf{n}} = \cos \alpha$ , can also be written as [Dachwald, 2004, p.9]:

$$\mathbf{F}_S = 2P_S A \cos^2 \alpha \hat{\mathbf{n}} \quad (3.38)$$

#### $\eta$ -IDEAL REFLECTION MODEL

Apart from the ideal reflection (IR) model, in [Dachwald, 2010] also the so-called  $\eta$ IR model is presented. This model is based on the IR one, but it takes advantage of a sail efficiency parameter  $\eta \in [0, 1]$  that accounts for the sail non-perfect reflectivity and deflection (usually a conservative value of  $\sim 0.85$  is considered for design purposes [McInnes, 1999, p.14]). Therefore  $\mathbf{F}_S$  is defined as:

$$\mathbf{F}_S = 2\eta P_S A \cos^2 \alpha \hat{\mathbf{n}} \quad (3.39)$$

The main advantage of these two IR models is that they allow to analyze the preliminary feasibility of a solar sailing mission in an easy way, thanks to their simple mathematical expressions of the force  $\mathbf{F}_S$ . However, this simplicity is mainly due to the assumption that  $\mathbf{F}_S$  points always along  $\hat{\mathbf{n}}$  (regardless of the sail attitude), which is something not strictly true in reality.

### 3.6.2. OPTICAL RADIATION MODELS

#### SIMPLIFIED OPTICAL RADIATION MODEL

In order to also take into account the effects of radiation absorption and transmission on the sail, a simplified optical radiation (OR) model can be exploited. This, as the

name suggests, takes into account the sail material optical properties to determine a more accurate equation for estimating the SRP (or LRP) force generated. As given in [Wie, 2004, pp.529-530], if one assumes that no radiation is transmitted by the sail and that no back reflection takes place, the following holds for  $F_S$ :

$$F_S = P_S A \cos \alpha \left\{ (1 - \rho_s) \hat{r} + \left[ 2\rho_s \cos \alpha + \frac{2}{3}\rho_d \right] \hat{n} \right\} \quad (3.40)$$

where  $\rho_s$  and  $\rho_d$  are called specular reflection and diffuse reflection coefficients and represent the fraction of reflected radiation that is specularly and diffusely reflected, respectively.

The main difference between this model and the IR ones is that, due to the non-ideal reflection coefficients considered, the SRP force direction  $\hat{f}_S$  is not coincident with the sail normal. Besides this, the use of a non-perfect sail also affects the thrust magnitude which results to be smaller compared to an ideal sail model.

### REFINED OPTICAL RADIATION MODEL

As presented in [Wie, 2004, p.529] (based on [McInnes, 1999, pp.47-51]), a more accurate OR model than the one previously discussed exists, which hereafter will be referred to as refined OR model. Such a model takes advantage of four additional parameters to define the sailcraft thrust, namely the sail's front and back surface emission coefficients  $\varepsilon_f$  and  $\varepsilon_b$ , and the front and back surface non-Lambertian coefficients  $B_f$  and  $B_b$  (which give information on the angular distribution of the radiation emitted and diffusely reflected by the two sides). Therefore the set of six parameters that uniquely defines the sail optical properties is found to be  $[\rho, s, \varepsilon_f, \varepsilon_b, B_f, B_b]$  (where the global reflection coefficient  $\rho = \rho_s + \rho_d$  and the alternative definition of the specular reflection coefficient  $s = \rho_s / \rho$  are used instead of  $\rho_s$  and  $\rho_d$ ).

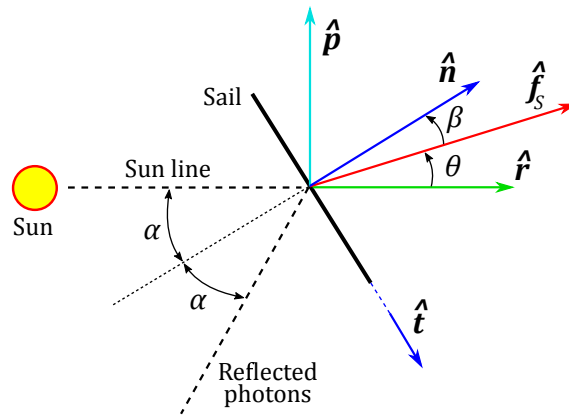


Figure 3.12: Representation of the sail vectors and angles lying in the  $\hat{r}$ - $\hat{n}$  plane (adapted after [Wie, 2004, p.529]).

When only the SRP is considered, the sailcraft thrust components along the sail normal direction  $\hat{n}$  and in-plane transversal direction  $\hat{t}$  (shown in Figure 3.12) are given by [Wie, 2004, p.529]:

$$F_n = P_S A \left[ (1 + \rho_s) \cos^2 \alpha + B_f \rho (1 - s) \cos \alpha + \frac{\varepsilon_f B_f - \varepsilon_b B_b}{\varepsilon_f + \varepsilon_b} (1 - \rho) \cos \alpha \right] \quad (3.41a)$$

$$F_t = P_S A [(1 - \rho_s) \cos \alpha \sin \alpha] \quad (3.41b)$$

and, therefore, the SRP thrust magnitude is equal to:

$$F_S = \sqrt{F_n^2 + F_t^2} = 2P_S A \Psi \cos \alpha \quad (3.42)$$

where

$$\Psi = \sqrt{(a_1 \cos \alpha + a_2)^2 + (a_3 \sin \alpha)^2} \quad (3.43)$$

with  $a_1$ ,  $a_2$  and  $a_3$  being

$$a_1 = \frac{1}{2}(1 + \rho s) \quad (3.44a)$$

$$a_2 = \frac{1}{2} \left[ B_f(1 - s)\rho + (1 - \rho) \frac{\varepsilon_f B_f - \varepsilon_b B_b}{\varepsilon_f + \varepsilon_b} \right] \quad (3.44b)$$

$$a_3 = \frac{1}{2}(1 - \rho s) \quad (3.44c)$$

As for the simplified OR model, also in the refined one the thrust does not always point along the sail normal direction, and this translates into having the so-called centerline angle  $\beta = \alpha - \theta$  usually not equal to zero. Besides its physical meaning, the centerline angle can also be intended as a measure of how much the thrust magnitude of an OR model differs from the one of an ideal sail. As shown in the exemplary Figure 3.13 from [Dachwald, 2004, p.13],  $\beta$  increases with the pitch angle so that, in turn,  $\theta$  reaches a maximum of roughly 55 deg for  $\alpha = 72.6$  deg. As a consequence the thrust magnitude difference is more evident for missions requiring highly tilted sails and more demanding steering strategies in general.

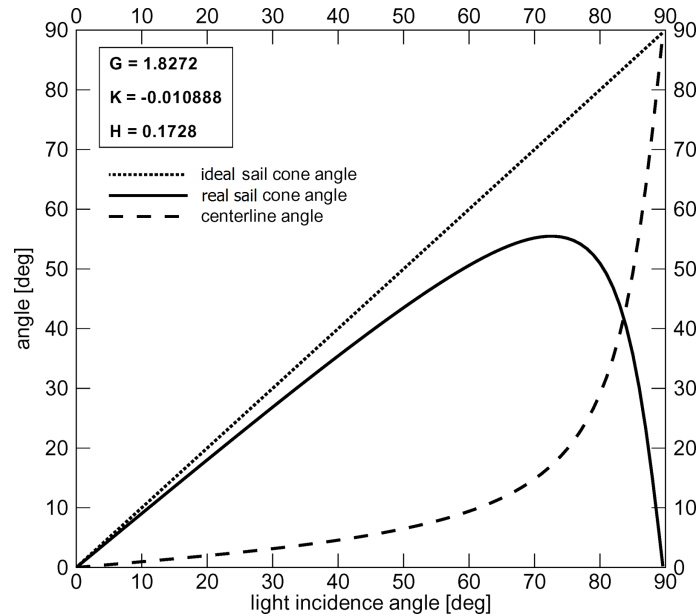


Figure 3.13: Sail cone angle  $\theta$  and centerline angle  $\beta$  as functions of the pitch angle  $\alpha$  for an ideal and non-ideal sail [Dachwald, 2004, p.13].

By varying the coefficients  $\varepsilon_f$ ,  $\varepsilon_b$ ,  $B_f$  and  $B_b$ , the centerline angle always shows a trend similar to the one of Figure 3.13, hence suggesting that these parameters do not strongly affect the thrust direction deflection from the sail normal. On the opposite, a

considerable difference is achieved when the coefficients  $\rho$  and  $s$  tend to 1 simultaneously, as in this case the impinging radiation is totally reflected, making the OR model act as an IR one. Indeed, in this case it results that the tangential force component  $F_t$  (given in Equation 3.41b) tends to 0, making the OR model force vector point along the normal direction, so that the centerline angle is always equal to 0.

### 3.6.3. GENERALIZED SAIL MODEL

Both the IR and OR models described above assume the solar sails to be flat. In reality, however, this is not strictly true, since sails always slightly billow when under load. Originally designed by [Rios-Reyes, 2006, pp.21-36], the generalized sail model is used for accurately estimating the SRP (or LRP) thrust of non-ideal solar sails having a curved surface. Consequently, in this case an accurate sail shape-model needs to be provided beforehand to compute the thrust. In order to take into account the sail deflection effects, the approach used in [Rios-Reyes, 2006, pp.21-36] (which constitutes the theoretical basis of this model) is that of considering the sail made up of infinitesimal elements of sail area  $dA$ , each having its own local normal unit vector  $\check{\mathbf{n}}$  and local in-plane transversal unit vector  $\check{\mathbf{t}}$  (similar to the  $\hat{\mathbf{n}}$  and  $\hat{\mathbf{t}}$  vectors shown in Figure 3.12). Since the thrust provided by each of these infinitesimal sail surface elements can be computed using Equations 3.41a and 3.41b valid for the refined OR model, the following holds [Rios-Reyes, 2006, p.22]:

$$d\mathbf{F}_n = 2P_S [a_1 \cos^2 \alpha + a_2 \cos \alpha] dA \check{\mathbf{n}} \quad (3.45)$$

$$d\mathbf{F}_t = 2P_S a_3 \cos \alpha \sin \alpha dA \check{\mathbf{t}} \quad (3.46)$$

with the  $a_i$  coefficients as given in Equations 3.44.

By integrating the infinitesimal force contribution over the whole sail area the total exerted force is obtained [Rios-Reyes, 2006, p.23]:

$$\mathbf{F}_S = \int_A (d\mathbf{F}_n + d\mathbf{F}_t) = \int_A d\mathbf{F}_n + \int_A d\mathbf{F}_t \quad (3.47)$$

It is important to underline that, using this model, a closed-form solution for  $\mathbf{F}_S$  is obtained only if the integral shown in Equation 3.47 can be performed analytically. However, often this is not the case. To overcome this problem the so-called surface normal distribution integrals  $\mathbf{J}^m$  (with  $m \in [1, 2, 3]$ ) are exploited, which represent the integral outer products of the normal vectors calculated over the entire sail surface area  $A$  [Dachwald, 2010, p.8]:

$$\mathbf{J}^m = \int_A \check{\mathbf{n}}^m dA = \int_A \underbrace{\check{\mathbf{n}}\check{\mathbf{n}}\dots\check{\mathbf{n}}}_m dA \quad (3.48)$$

In this way, Equation 3.47 can be rewritten as:

$$\mathbf{F}_S = 2P_S [a_2 \mathbf{J}^2 \cdot \hat{\mathbf{r}} - 2\rho s \hat{\mathbf{r}} \cdot \mathbf{J}^3 \cdot \hat{\mathbf{r}} - a_3 (\mathbf{J}^1 \cdot \hat{\mathbf{r}}) \hat{\mathbf{r}}] \quad (3.49)$$

This new expression for  $\mathbf{F}_S$  allows a more trivial computation of the sail thrust which, thanks to the symmetry properties of the  $\mathbf{J}^m$  tensors, can be evaluated by knowing 19 coefficients at most [Rios-Reyes, 2006, p.26].

### 3.6.4. CHOICE OF SAIL MODEL

The sail force models presented in this section have been discussed highlighting both their mathematical complexity and the precision of the results they can provide. Indeed it was shown that realistic/accurate SRP (or LRP) force estimates can be achieved only by exploiting complex models, which in turn automatically increase the complexity of the EoM to numerically integrate and thus the computational effort required. As will be explained in Chapter 4, the trajectory optimizer used for this project has already been used to optimize solar sailing trajectories. Consequently, already before this thesis project it had available some SRP force models, such as the basic IR and OR ones. On the other hand, no LRP force model was available, and therefore its implementation from the ground up has been required. Given these considerations, besides the accuracy and complexity of the sail models, also the availability in the optimizer of the SRP force models and the effort required for the LRP force model implementation have been taken into account when choosing the sail model to exploit for the optimizations.

The trade-off procedure carried out to choose such a sail model is summarized in the Pugh matrix in Table 3.1.

Table 3.1: Pugh matrix used for comparing different solar sail models.

Criteria	Weights	Basic IR	$\eta$ IR	Simpl. OR	Ref. OR	Generalized
Accuracy	2	-1	0	0	+1	+1
Complexity	2	+1	+1	0	0	-1
SRP force model availability	3	+1	-1	+1	+1	-1
LRP force model implementation effort	3	+1	+1	0	-1	-1
	<b>Sum</b>	+6	+2	+3	+2	-6

Since the implementation of the SRP or LRP force models from the ground up requires a significant amount of time spent on programming (while a limited time has been given to perform the entire thesis project), the weights assigned to the "SRP force model availability" and "LRP force model implementation effort" criteria are the highest. Nonetheless, relatively high weights have also been given to the "Accuracy" and "Complexity" criteria, as the reliability of the solutions found and the time required for computing them is also considerably relevant.

The results of the trade-off given in Table 3.1 clearly show that the best possible model to choose is the basic IR one. Such a choice is in line with the fact that the main purpose of this work is to analyze laser-enhanced solar sailing only preliminary, in order to assess the advantages it can provide as compared to traditional solar sailing. On the other hand, in the case a positive outcome from such an analysis were provided, more complex sail models could be used for further studies.

Due to the ideal reflection assumption, the exploitation of such a model automat-

ically yields over-estimated thrust values (especially for large pitch angles) and thus a better performance with respect to real sails. This can be appreciated in the exemplary Figure 3.14 (based on [Dachwald, 2004, p.14]), where the envelope curves of all achievable SRP thrust vectors (defined by changing  $\alpha$ ) are given for different sail models.

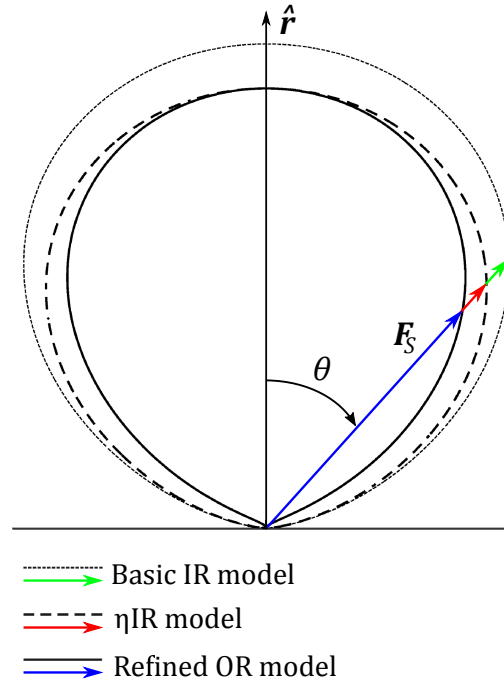


Figure 3.14: Envelope curves of all achievable SRP thrust vectors (defined by changing  $\alpha$ ) related to different sail models (based on [Dachwald, 2004, p.14]).

Using perfectly reflecting solar sails is not possible in reality but, thanks to the sail coating materials available nowadays (aluminium above all), the achievable reflectivity of solar sails can reach even 90% [McInnes, 1999, p.63]. In this way, the difference in the TOF of ideal and non-ideal solar sail optimal trajectories ranges between 5% and 15% (for trajectories requiring respectively small and large cone angles, on average) [Dachwald, 2004, p.88]. However it should be noted that, since this sail model will be used both for traditional and laser-enhanced solar sailing, either type of trajectories will be affected by the above-mentioned shortening in the flight time. This means that, on the opposite, the TOF difference between these trajectories will be less affected by such a flight time shortening, eventually. As a consequence, the flight time differences computed will still give valuable insights on the laser-enhanced solar sailing performance despite using an ideally perfectly reflecting sail.

Equation 3.31 found for the LRP is the equivalent of Equation 3.14 valid for the SRP, and therefore the basic IR SRP force model presented in Subsection 3.6.1 can be re-adapted to the LRP case simply by substituting the term  $P_S$  with  $P_L$ . However some attention should be paid concerning the radiation incidence angle in the equations since, in this case, the angle  $\alpha_L$  shall be considered instead of  $\alpha$ .

Based on these considerations and the above-discussed choice of the sail model to use, hereafter the SRP thrust will be expressed as given in Equation 3.38, while the following

expression will be used for the LRP thrust:

$$\mathbf{F}_L = 2P_L A \cos^2 \alpha_L \hat{\mathbf{n}} = 2\chi \frac{W_L}{c} \xi^2 \cos^2 \alpha_L \hat{\mathbf{n}} \quad (3.50)$$

### 3.7. PERTURBING FORCES

In order to correctly model the orbital dynamics of a sailcraft performing an interplanetary flight, one has to consider first of all the solar gravitational force, the SRP force, the LRP force (in the case a laser-enhanced sail is considered) and, eventually, other possible perturbing forces acting on the S/C. In particular, in order to choose which perturbations one should take into account, it is fundamental to analyze such forces in terms of their magnitude. As given in [Wakker, 2015, p.548] and [McInnes, 1999, p.54], the most relevant ones are related to atmospheric drag, solar wind, non-spherical gravitational potential of celestial bodies and gravitational forces of other bodies besides the Sun.

The atmospheric drag strongly affects the S/C motion when this travels within hundreds of kilometers above the Earth's surface, as happens for LEO satellites (although the same is valid also for other celestial bodies having an atmosphere). Consequently when dealing with interplanetary trajectories this perturbation can be neglected, since the S/C flies in vacuum and without performing such celestial body close approaches. In a similar fashion, the non-spherical gravitational potential perturbations (i.e. perturbations due to a body's gravity field "irregularities") become relevant only when orbiting about a celestial body at a low altitude and for a relatively long time. Since this will not be the case, also these perturbations can be neglected.

Another force to consider is the one given by the solar wind when impacting the sailcraft. As given in [McInnes, 1999, p.54], the solar wind is a stream of charged particles released from the upper layers of the solar atmosphere which yield a small pressure on the S/C in the order of  $3 \cdot 10^{-9} \text{ Nm}^{-1}$  at Earth. This value is  $\sim 1.4 \cdot 10^3$  times smaller than the SRP at Earth (given in Equation 3.16) and, as such, also the solar wind pressure force will be roughly  $1.4 \cdot 10^3$  smaller than the SRP one. Therefore, also the solar wind perturbation will be neglected.

Eventually the only perturbing force that may considerably affect a sailcraft motion during an interplanetary flight (and thus requires a more thorough analysis) is the gravitational force of a third (disturbing) body. Its expression in vector form is the following [Wakker, 2015, p.106]:

$$\mathbf{a}_d = \mu_d \left( \frac{\mathbf{r}_{S/C-d}}{\|\mathbf{r}_{S/C-d}\|^3} - \frac{\mathbf{r}_d}{\|\mathbf{r}_d\|^3} \right) \quad (3.51)$$

where  $\mu_d$  represents the gravitational parameter of the disturbing body,  $\mathbf{r}_d$  is the third-body position vector as seen from the central body (hereafter assumed to be the Sun) and  $\mathbf{r}_{S/C-d}$  is the S/C-disturbing body vector (see Figure 3.15, modified from [Wakker, 2015, p.107]). In general, the disturbing-body acceleration becomes significant in certain situations while it can be neglected in others. In particular, its magnitude depends on the S/C-disturbing body distance as  $1/r^2$ , meaning that it rapidly increases when approaching the disturbing body itself, e.g. entering its sphere of influence (SOI). Be-

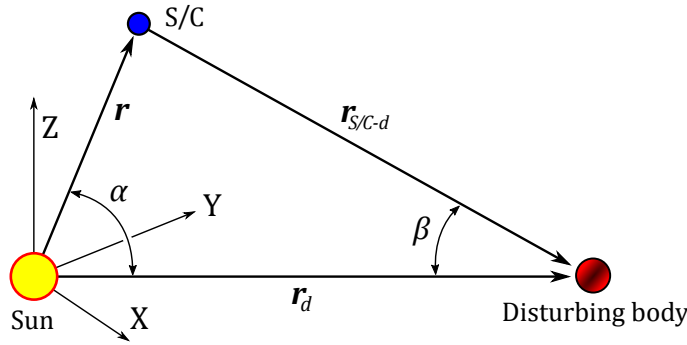


Figure 3.15: Geometrical configuration of a S/C, the central body (Sun) and a third disturbing body (modified from [Wakker, 2015, p.107]).

cause of this, attention should be paid when performing missions which require a celestial body close approach, such as rendezvous and flybys.

In the present work three mission scenarios will be analyzed: an orbit rendezvous to Mercury, an orbit rendezvous to Mars and a flyby to Neptune. For all these missions the starting point of the interplanetary flight segments will be at Earth, already outside its SOI and inserted in an interplanetary trajectory with a hyperbolic excess energy of  $0 \text{ km}^2\text{s}^{-2}$ . Moreover, for the orbit rendezvous to Mercury and Mars, the sailcraft simply inserts these celestial body orbits, hence without actually approaching their spheres of influence either. Therefore, for these two mission scenarios, no celestial body provides a significant disturbing acceleration to the sailcraft motion and hence  $\mathbf{a}_d$  can be neglected.

On the other hand, in the Neptune flyby mission the sailcraft actually enters the Neptunian SOI during the last phase of the flight. To analyze the effects of this additional gravitational acceleration, let us consider its magnitude in the worst-case scenario, achieved when the S/C lies in the  $\mathbf{r}_d$  direction (so that, with regard to Figure 3.15, it holds  $\alpha = \beta = 0$  deg). In this case, the magnitude of  $\mathbf{a}_d$  can be expressed as a function of  $r$  as follows [Wakker, 2015, p.107]:

$$a_d = \frac{\mu_d}{r_d^2} \left| \left( \frac{r_d}{r_d - r} \right)^2 - 1 \right| \quad (3.52)$$

with  $r_d = a_\psi = 30.069923 \text{ AU}$  and  $\mu_d = \mu_\psi = 6.8351 \cdot 10^{15} \text{ m}^3\text{s}^{-2}$  being Neptune's semi-major axis and gravitational parameter [Wakker, 2015, p.673][NASA, 2017b]. If one considers the flight segment within the SOI of Neptune, it holds that  $r \in [a_\psi - R_{SOI,\psi}, a_\psi]$ , with  $R_{SOI,\psi} = 8.66 \cdot 10^7 \text{ km}$  being the SOI radius [Wakker, 2015, p.115]. Moreover, it is reasonable to assume that the S/C enters the SOI with a relatively high excess velocity and that, once inside of it, the solar gravitational acceleration can be neglected. As demonstrated in Section A.1 of Appendix A, from these assumptions it is possible to numerically integrate Equation 3.52 to retrieve the TOF between the entering in the SOI and the actual approach to the planet. Moreover, the same calculations can be repeated under the simplistic hypothesis that Neptune yields no gravitational acceleration. By doing so, it results that the TOF difference defined by neglecting Neptune's gravity force is  $0.02 - 0.14$  days for excess velocities in the range  $15-30 \text{ km s}^{-1}$ . If one considers that the characteristic flight times for solar sailing missions to the outer Solar System are in the order of years [Dachwald, 2004, pp.80-83], it results that TOF dif-

Table 3.2: Orders of magnitude of the main perturbing accelerations acting on an ideal solar sail. The accelerations due to SRP, LRP and solar gravity are also given for comparison. The sail has a characteristic acceleration of  $0.5 \text{ mm s}^{-2}$  and the LS provides a laser flux equal to 2.76% the solar one.

Acceleration type	Magnitude [ $\text{mms}^{-2}$ ]	Notes
SRP	0.5	Calculated at Earth
LRP	$1.4 \cdot 10^{-2}$	Calculated at 1 AU from the LS
Solar gravity	5.93	Calculated at Earth
Atmospheric drag	$\sim 0.0$	Absent as interplanetary flights takes place in vacuum
Non-spherical gravity model	$\sim 0.0$	Relevant only for planetocentric flights
Solar wind	$3.5 \cdot 10^{-4}$	Calculated at Earth
Third-body gravity - Mercury, Mars	$\sim 0.0$	Negligible as no planet close approach takes place
Third-body gravity - Neptune	$9.1 \cdot 10^{-4}$	Computed at a distance from Neptune equal to $R_{SOL,\Psi}$

ferences of less than one day are definitely negligible and, for this reason, also for this mission scenario  $\mathbf{a}_d$  will not be considered.

Finally the conclusion drawn from these considerations is that none of the above-described major perturbing forces affects the sailcraft dynamics considerably, and thus these will not be taken into account for the simulations setup. For the sake of summary, the magnitudes of the SRP acceleration, LRP acceleration, solar gravitational acceleration and all above-presented disturbing accelerations have been calculated and shown in Table 3.2. In particular, the SRP and LRP accelerations have been computed using a solar sail with characteristic acceleration of  $0.5 \text{ mm s}^{-2}$  and an LS providing a laser flux equal to 2.76% the solar one (these parameters are the same used in Chapter 7 for the trajectory optimizations).

## 3.8. EQUATIONS OF MOTION

### 3.8.1. VECTORIAL FORM

Based on the SRP and LRP forces presented in the previous sections, the EoM for traditional and laser-enhanced solar sailing can be defined. In order to do so, let us firstly consider the perturbed form of the two-body problem (2BP) equation (modified from [Wakker, 2015, p.219]):

$$\ddot{\mathbf{r}} = -\frac{\mu_{\odot}}{r^3} \mathbf{r} + \mathbf{a} \quad (3.53)$$

with  $\mu_{\odot} = 1.327124421 \cdot 10^{20} \text{ m}^3 \text{ s}^{-2}$  representing the gravitational parameter of the Sun [Wakker, 2015, p.673]. Since the vector  $\mathbf{a}$  represents the sum of all accelerations different from the solar gravitational one, this equation can also be used to describe

the dynamics of a traditional or laser-enhanced solar sail. In fact, in the former case one simply needs to substitute  $\mathbf{a}$  with the SRP acceleration  $\mathbf{a}_S$ , whereas in the latter case also the LRP acceleration  $\mathbf{a}_L$  should be considered, so that  $\mathbf{a} = \mathbf{a}_S + \mathbf{a}_L$ . Although in theory the SRP and LRP acceleration vectors can be found by dividing the  $\mathbf{F}_S$  and  $\mathbf{F}_L$  force vectors presented in Sections 3.6 and 3.5 by the sailcraft total mass  $m$ , usually other expressions are exploited that are more suited to describe the solar sailing orbital dynamics. Such expressions make use of the sail loading parameter  $\sigma$ , characteristic acceleration  $a_c$ , or lightness number  $\beta$  defined hereafter.

The sail loading parameter  $\sigma$  is defined as the ratio of the sailcraft total mass to its sail area, i.e. [Dachwald, 2004, p.14]:

$$\sigma = \frac{m}{A} \quad (3.54)$$

By definition the characteristic acceleration is the SRP acceleration that a (traditional) solar sail experiences at a distance of 1 AU from the Sun when oriented perpendicularly with respect to the Sun line. Its expression is therefore given by [Dachwald, 2005, p.1188][McInnes, 1999, p.14]:

$$a_c = \frac{2P_0}{\sigma} \cdot \eta \quad \text{with} \quad \eta = \frac{F_S(\alpha = 0 \text{ deg})}{2P_S A} \quad (3.55)$$

For ideal sails as the one used within this work it results that  $\eta = 1$  always. However, if an  $\eta$ IR model is adopted, the parameter  $\eta$  given above represents the sail efficiency that characterizes the SRP force magnitude as given in Equation 3.39. Similarly, in the case an OR model is exploited,  $\eta$  is equal to the efficiency coefficient  $\Psi$  presented in Equation 3.43.

Eventually the lightness number  $\beta$  is defined as the ratio of the characteristic acceleration to the solar gravitational one at 1 AU. As both these accelerations vary as  $1/r^2$ , their ratio is not dependent on the heliocentric distance and thus  $\beta$  depends solely on the sailcraft characteristics. Its expression is given by [McInnes, 1999, p.40]:

$$\beta = \frac{\sigma^*}{\sigma} \quad (3.56)$$

where

$$\sigma^* = \frac{\mathcal{L}_\odot}{2\pi\mu_\odot c} \quad (3.57)$$

is referred to as critical sail loading parameter and is approximately equal to  $1.53 \text{ gm}^{-2}$  [McInnes, 1999, p.40].

By taking advantage of the parameters presented above, for an ideal sail  $\mathbf{a}_S$  can be defined as [McInnes, 1999, p.40]:

$$\mathbf{a}_S = \beta \frac{\mu_\odot}{r^2} \cos^2 \alpha \hat{\mathbf{n}} \quad (3.58)$$

whereas  $\mathbf{a}_L$  can be directly derived from Equation 3.50 as:

$$\mathbf{a}_L = 2\chi \frac{W_L}{Ac\sigma} \xi^2 \cos^2 \alpha_L \hat{\mathbf{n}} \quad (3.59)$$

The above formula is in accordance with [McInnes, 1999, pp.273-275], where the expression for the maximum LRP acceleration provided to a laser-driven sail placed normally with respect to laser light is given as:

$$\begin{cases} a_{L|max} = \frac{4}{\pi d^2} \frac{1 + \rho_s}{\sigma c} W_L & \text{for } s \leq \tilde{s} \\ a_{L|max} = \frac{4}{\pi d^2} \frac{1 + \rho_s}{\sigma c} W_L \left(\frac{\tilde{s}}{s}\right)^2 & \text{for } s > \tilde{s} \end{cases} \quad (3.60)$$

with  $\rho_s$  being the sail reflectivity used in the simplified OR force model. Indeed, if one considers that for an ideal sail  $\rho_s = 1$  and that  $A = \pi(d/2)^2$ , the above-presented  $a_{L|max}$  expressions become equal to the magnitude of  $\mathbf{a}_L$  as provided in Equation 3.59 with  $\alpha_L = 0$  deg and  $\chi = 1$ .

Given these results, the EoM for a traditional or laser-enhanced sailcraft can be found by respectively setting  $\mathbf{a} = \mathbf{a}_S$  or  $\mathbf{a} = \mathbf{a}_S + \mathbf{a}_L$  in Equation 3.53, eventually yielding to:

$$\ddot{\mathbf{r}} = -\frac{\mu_{\odot}}{r^3} \mathbf{r} + \beta \frac{\mu_{\odot}}{r^2} \cos^2 \alpha \hat{\mathbf{n}} \quad (3.61a)$$

$$\ddot{\mathbf{r}} = -\frac{\mu_{\odot}}{r^3} \mathbf{r} + \left[ \beta \frac{\mu_{\odot}}{r^2} \cos^2 \alpha + 2\chi \frac{W_L}{Ac\sigma} \xi^2 \cos^2 \alpha_L \right] \hat{\mathbf{n}} \quad (3.61b)$$

### 3.8.2. CHOICE OF THE COORDINATES SYSTEM

In order to retrieve the trajectories of traditional and laser-enhanced sailcraft in time, the EoM provided in Equations 3.61 shall be numerically integrated. The computational effort required to carry out this procedure is strictly related to the way the EoM are expressed, which in turn is something dependent both on the reference frame and coordinate system used. As already mentioned in Section 3.1, in this work interplanetary trajectories will be analyzed and therefore the most logical choice is to express the sailcraft motion from within a heliocentric  $\mathcal{F}$ -frame. On the opposite, concerning the coordinate system to use, a preliminary analysis should be conducted to determine which is best to exploit. As many different parameters affect this decision-making process, the Pugh matrix presented in Table 3.3 has been used to effectively summarize all of them and eventually pick up the most promising option.

Table 3.3: Pugh matrix used for comparing different coordinate systems.

Criteria	Weights	Cartesian	Spherical	Keplerian	Equinoctial
Physical meaning	1	-1	0	+1	-1
EoM complexity	3	-1	+1	-1	-1
Singularities	2	+1	0	-1	+1
Programming effort for implementation	3	0	+1	-1	-1
	<b>Sum</b>	-2	+6	-7	-5

As can be seen in the above matrix, the spherical coordinates outperform Cartesian coordinates, Keplerian elements and modified equinoctial elements for various reasons.

Concerning the physical meaning of the EoM solutions, trajectories expressed in terms of equinoctial elements and Cartesian coordinates result by far the less straightforward to interpret and, not by chance, conversion routines to retrieve Keplerian elements from these two coordinate sets are usually exploited in astrodynamics. On the other hand, the physical interpretation of the solution given in spherical coordinates is slightly more straightforward, while it is even easier for trajectories expressed through Keplerian elements, as these provide valuable information regarding the orbit dimensions, shape and orientation.

Moving to the actual shapes of the EoM defined by each coordinate set, both the equations complexity and absence/presence of singularities have been considered. Despite being singularity-free, the Cartesian EoM are relatively complex, mainly because the unit vector  $\hat{n}$  cannot be expressed in a straightforward way unless a computationally expensive 1-2-3 frame rotation is carried out. On the opposite, when using Keplerian elements  $\hat{n}$  can be easily retrieved and used within the planetary equations which, however, are relatively complex and become singular for eccentricity or inclination values (almost) equal to zero. The latter problem is solved when using modified equinoctial elements, although they yield complex EoM as well. The equations defined by spherical coordinates are instead relatively simple and become singular only if the S/C passes through the celestial north pole ( $\phi = 90$  deg), which is a circumstance unlikely to take place for rendezvous or flyby missions as the ones presented in this work. Eventually, the last criterion considered concerns the programming effort required for implementing the EoM within InTrance, i.e. the software presented in the next chapter through which trajectory propagation and optimization have been performed. As explained in [Dachwald and Ohndorf, 2010, p.3], InTrance has been designed to propagate the solar sailing EoM for interplanetary trajectories using spherical coordinates, while Cartesian coordinates are used only for planetocentric problems. As a consequence, based on the above-presented considerations, it results that the use of spherical coordinates to integrate the EoM represents the option requiring the smallest implementation effort, followed by the use of Cartesian coordinates and, lastly, of the Keplerian and modified equinoctial elements (for which the EoM implementation should be carried out from the ground up).

Given all these considerations, it was therefore chosen to express the EoM using spherical coordinates. The related differential equation systems (DEs) used to describe the traditional and laser-enhanced sailcraft dynamics are presented in the following subsection.

### 3.8.3. EQUATIONS OF MOTION IN SPHERICAL COORDINATES

The general form of the EoM in spherical coordinates can be retrieved by rewriting the perturbed 2BP equation using the unit vectors and their derivatives as presented in Subsection 3.2.2. In particular, by using the definition of  $\hat{r}$  given in Equation 3.2, the first and second derivative of  $\mathbf{r}$  with respect to time can be expressed as [Dachwald,

2004, p.122]:

$$\dot{\mathbf{r}} = \frac{d}{dt}(r\hat{\mathbf{r}}) = \dot{r}\hat{\mathbf{r}} + r\dot{\theta}\cos\phi\hat{\boldsymbol{\theta}} + r\dot{\phi}\hat{\boldsymbol{\phi}} \quad (3.62a)$$

$$\begin{aligned} \ddot{\mathbf{r}} = & \hat{\mathbf{r}}[\ddot{r} - r\dot{\theta}^2\cos^2\phi - r\dot{\phi}^2] + \\ & \hat{\boldsymbol{\theta}}[2\dot{r}\dot{\theta}\cos\phi - 2r\dot{\theta}\dot{\phi}\sin\phi + r\ddot{\theta}\cos\phi] + \\ & \hat{\boldsymbol{\phi}}[2\dot{r}\dot{\phi} + r\ddot{\phi} + r\dot{\theta}^2\cos\phi\sin\phi] \end{aligned} \quad (3.62b)$$

By including these results into Equation 3.53, the following differential equations describing the sailcraft motion in terms of  $r$ ,  $\theta$  and  $\phi$  are found [Dachwald, 2004, p.17]:

$$\begin{cases} \ddot{r} = r\dot{\phi}^2 + r\dot{\theta}^2\cos\phi - \frac{\mu}{r^2} + a_r \\ \ddot{\theta} = 2\dot{\theta}\dot{\phi}\tan\phi - 2\frac{\dot{r}\dot{\phi}}{r} + \frac{a_\theta}{r\cos\phi} \\ \ddot{\phi} = -2\frac{\dot{r}\dot{\phi}}{r} - \dot{\theta}^2\sin\phi\cos\phi + \frac{a_\phi}{r} \end{cases} \quad (3.63)$$

The terms  $a_r$ ,  $a_\theta$  and  $a_\phi$  on the right-hand side (RHS) of the above equations represent the components of the sailcraft acceleration vector  $\mathbf{a}$  in the  $\hat{\mathbf{r}}$ ,  $\hat{\boldsymbol{\theta}}$  and  $\hat{\boldsymbol{\phi}}$  directions. Since  $\mathbf{a}$  is given only by the SRP and LRP accelerations which both point along the sail normal unit vector, defining the latter in spherical coordinates is of fundamental importance to obtain the DES sought.

Let us consider the vector  $\hat{\mathbf{n}}$  as defined within an  $\mathcal{O}$ -frame [McInnes, 1999, p.115]:

$$\hat{\mathbf{n}}_{\mathcal{O}} = [n_r, n_d, n_h]^T = [\cos\alpha, \sin\alpha\cos\delta, \sin\alpha\sin\delta]^T \quad (3.64)$$

From here the normal unit vector expressed in an  $\mathcal{S}$ -frame (i.e. a spherical coordinate  $\mathcal{S}$ -frame) can be retrieved by means of a single axis rotation about the  $\hat{\mathbf{r}}$  direction, as shown in Figure 3.16.

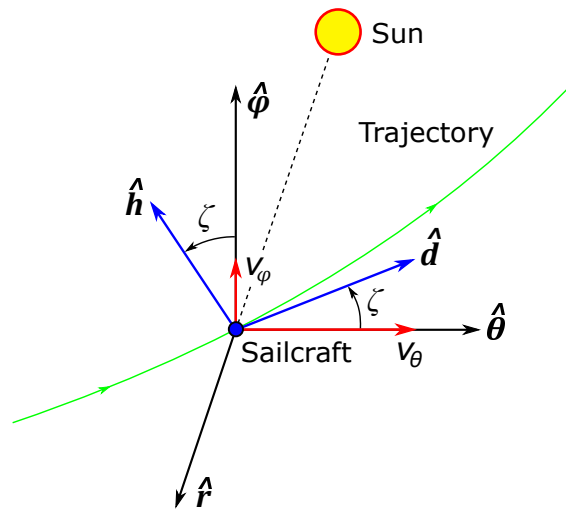


Figure 3.16: Orbital reference frame unit vectors and spherical coordinates' unit vectors. The former can be computed from the latter ones by performing a rotation of an angle  $\zeta$  about the  $\hat{\mathbf{r}}$  direction.

The rotation angle associated to such a reference transformation is the orbit angle  $\zeta = \text{atan2}(v_\phi, v_\theta)$ , which can also be expressed as  $\zeta = \text{atan2}(\dot{\phi}, \dot{\theta} \cos\phi)$ , since  $v_\phi = r\dot{\phi}$  and  $v_\theta = r\dot{\theta} \cos\phi$  [Dachwald, 2004, p.123]. Consequently the frame rotation can be performed as follows:

$$\begin{bmatrix} n_r \\ n_\theta \\ n_\phi \end{bmatrix} = \begin{bmatrix} 1 & 0 & 0 \\ 0 & C_\zeta & -S_\zeta \\ 0 & S_\zeta & C_\zeta \end{bmatrix} \begin{bmatrix} n_r \\ n_d \\ n_h \end{bmatrix} \quad (3.65)$$

Eventually, by taking advantage of Equation 3.64 and applying some trigonometric properties, the following expression for  $\hat{\mathbf{n}}$  within the  $\mathcal{F}_s$ -frame is found:

$$\hat{\mathbf{n}}_{\mathcal{F}_s} = [n_r, n_\theta, n_\phi]^T = [\cos\alpha, \sin\alpha \cos(\delta + \zeta), \sin\alpha \sin(\delta + \zeta)]^T \quad (3.66)$$

Given this result, the SRP and LRP acceleration vectors defined in Subsection 3.8.1 can be firstly expressed inside of the  $\mathcal{F}_s$ -frame and, successively, used to define the total radiation pressure acceleration  $\mathbf{a}$  both for traditional and laser-enhanced solar sails. In this way the  $a_r$ ,  $a_\theta$  and  $a_\phi$  acceleration components are automatically found and can be used inside Equations 3.63. More specifically, for a traditional solar sail the above-mentioned acceleration components are equal to:

$$\begin{cases} a_r = \beta \frac{\mu_\odot}{r^2} \cos^3 \alpha \\ a_\theta = \beta \frac{\mu_\odot}{r^2} \cos^2 \alpha \sin\alpha \cos(\delta + \zeta) \\ a_\phi = \beta \frac{\mu_\odot}{r^2} \cos^2 \alpha \sin\alpha \sin(\delta + \zeta) \end{cases} \quad (3.67)$$

whereas for a laser-enhanced sailcraft the following holds:

$$\begin{cases} a_r = \beta \frac{\mu_\odot}{r^2} \cos^3 \alpha + 2\chi \frac{W_L}{Ac\sigma} \xi^2 \cos^2 \alpha_L \cos\alpha \\ a_\theta = \beta \frac{\mu_\odot}{r^2} \cos^2 \alpha \sin\alpha \cos(\delta + \zeta) + 2\chi \frac{W_L}{Ac\sigma} \xi^2 \cos^2 \alpha_L \sin\alpha \cos(\delta + \zeta) \\ a_\phi = \beta \frac{\mu_\odot}{r^2} \cos^2 \alpha \sin\alpha \sin(\delta + \zeta) + 2\chi \frac{W_L}{Ac\sigma} \xi^2 \cos^2 \alpha_L \sin\alpha \sin(\delta + \zeta) \end{cases} \quad (3.68)$$

Using the above-presented expressions for  $a_r$ ,  $a_\theta$  and  $a_\phi$  in the RHS of Equations 3.63 yields to the final EoM valid for ideal traditional and laser-enhanced solar sails.

# 4

## OPTIMIZATION

In order to find traditional and laser-enhanced sailcraft time flight-optimal trajectory, an optimization software has been used. In this chapter the trade-off at the base of the choice of this optimizer is presented and, afterwards, its functioning explained in detail. In particular, the theory behind the optimization procedure is described, together with the optimizer architecture and types of output returned, in order easily discuss the laser-enhanced solar sailing implementation and validation given in the next chapter.

### 4.1. CHOICE OF OPTIMIZER

In order to determine the best software to integrate and optimize traditional and laser-enhanced solar sail trajectories, many different factors have to be taken into account. More specifically, in [Carzana, 2017, pp.79-101] an extensive discussion concerning different optimization methods and optimization software has been carried out, which yielded the conclusions summarized hereafter.

Since the main purpose of this work is to carry out a first-order analysis of laser-enhanced solar sailing to assess its potential advantages as compared to traditional solar sailing, the use of global trajectory optimization methods (GTOMs) has been preferred over local trajectory optimization methods (LTOMs). Indeed, even though global techniques are usually less accurate compared to local optimization methods (such as sequential quadratic programming), by definition they can be successfully used to extensively scan the solution search space and thus find the global optima sought. On the other hand, LTOMs can easily fall into local minima and therefore they can be used best only once the search space near-global optimum region has been located (which might be found through a GTOM, for instance).

Given this, a comparison between two available global trajectory optimization software programs has been carried out: InTrance (standing for “intelligent trajectory optimization using neurocontroller evolution”), developed by Bernd Dachwald from FH Aachen University and Andreas Ohndorf from DLR, and PaGMO (acronym of “Parallel Global Multiobjective Optimiser”), from ESA’s Advanced Concept Team, to be used in conjunction with the TU Delft Astrodynamics Toolbox (TUDAT). Despite PaGMO

being capable of finding near-global optima by taking advantage of different optimization techniques simultaneously, hence making it highly versatile and suited to solve high-dimensional global optimization problems, ultimately it has been chosen to use InTrance for optimizing the traditional and laser-enhanced solar sailing trajectories presented in this report. The main reasons behind this choice are essentially three: a verified efficiency to begin with, since this software has already been successfully used in [Dachwald, 2004] to optimize interplanetary solar sailing trajectories; secondly, major technical support which has been available for InTrance compared to the one available for TUDAT (since the entire project has been carried out at the FH Aachen University); and, lastly, TUDAT missed implementation of a (traditional) solar sailing propulsion system [TUDAT, 2017].

The main advantages of the evolutionary neurocontrol (ENC) optimization technique used by InTrance are represented by its high reliability (given by its ability to exhaustively scan the solution search space), the easy constraint handling and the automatic retrieval of the optimal initial conditions (ICs). On the other hand, drawbacks of this GTOM are its mathematical complexity and the relatively high computational effort required.

These characteristics will be discussed in the next sections, where the structure of InTrance and its main features are presented.

## 4.2. INTRANCE OVERVIEW

### 4.2.1. EVOLUTIONARY NEUROCONTROL

ENC is a sophisticated technique which allows the computing of near-global optimal solutions through the exploitation of artificial neural networks (ANNs), machine learning and evolutionary algorithms (EAs) at the same time. Compared to other global optimization techniques, within ENC the optimization problem is formulated through different means so that it is also approached from a completely different perspective. Defining  $X$  as a situation and  $A$  as an action, what ENC does is finding a time-independent associative mapping  $S : X \rightarrow A$  (called strategy) that links situations to actions. For example, when trajectory optimization is concerned,  $X$  may represent both the S/C state  $\mathbf{x}_{SC}$  and target body state  $\mathbf{x}_T$ , whereas  $A$  and  $S$  would represent the S/C control function  $\mathbf{u}$  and steering strategy, respectively. The "optimality" of a strategy is measured based on how this interacts with the environment (which is modeled through the EoM); this means that, for each situation  $X$  and corresponding action  $A$  determined by a strategy  $S$ , an evaluation  $J(X, A)$  (equivalent to the cost function) can be computed that expresses how much the considered strategy is optimal. As a consequence, from this perspective, the problem of finding an optimal trajectory translates into finding the optimal (steering) strategy  $S^*$  that yields the optimal control history  $\mathbf{u}^*[t]$  and corresponding trajectory  $\mathbf{x}^*[t]$  (note that here  $[t]$  indicates the history of the corresponding variable) [Dachwald, 2004, pp.37-38].

In order to tackle the optimization problem from the above-presented perspective, neural networks can be used as they represent a way to actually codify the concept of steering strategy  $S$ . By definition a neural network is a structure made up of multiple

processing elements called neurons linked together by connections which regulate the exchange of information between them. The number of neurons and the way they are connected define the ANN's topology, which strictly affects how information flows from input to output. As an example, Figure 4.1 (adapted from [Dachwald, 2004, p.53]) shows an ANN with feed-forward neural topology, which has a characteristic layered structure.

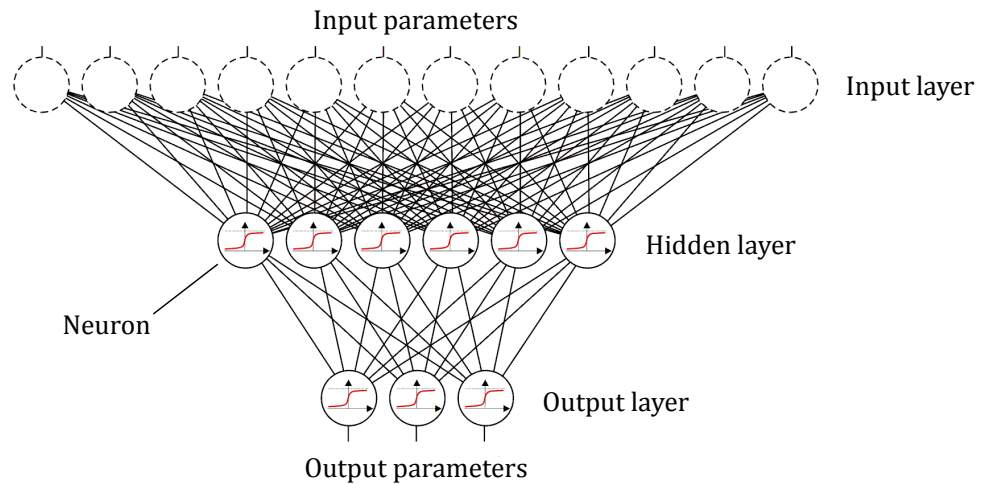


Figure 4.1: ANN with feed-forward layered structure topology (adapted from [Dachwald, 2004, p.53]).

Despite its intrinsic complexity, a neural network can always be regarded as a function  $N_{\pi}$  (called network function) which transforms input parameters into output parameters. Its functioning is totally based on a set of neural parameters  $\pi = [\pi_1, \dots, \pi_n]$  capable of regulating how neurons process the information and how they interact with each other through neural connections. In this way, once given a parameter set  $\pi$ , the ANN is automatically defined, and in turn the associated strategy  $S$  is specified as well (for the sake of clarity a graphical illustration showing how the ANN neurons' parameters are mapped onto a vector  $\pi$  is provided in Figure 4.2 [Dachwald, 2004, p.50]). Therefore, thanks to ANNs, the abstract problem of finding  $S^*$  gets translated into a computationally solvable problem, that is retrieving the optimal parameter vector  $\pi^*$  [Dachwald, 2004, p.37].

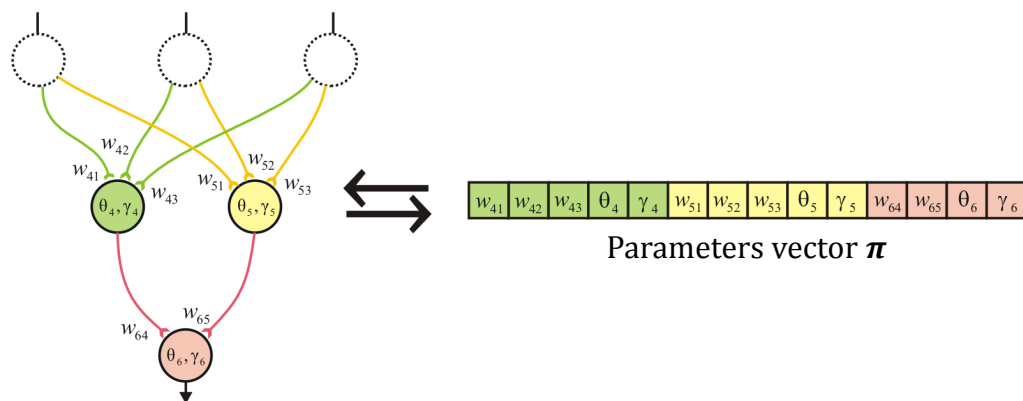


Figure 4.2: Mapping of a neural network neurons' parameters onto a parameter vector  $\pi$  [Dachwald, 2004, p.50].

To fulfill the latter task, ENC exploits an EA. Indeed, any vector  $\boldsymbol{\pi}$  can be mapped onto a chromosome  $\boldsymbol{\xi}$  (i.e. a real-valued string) so that, when considering a population of  $n$  different chromosomes,  $n$  different types of ANN can actually be retrieved from these. Given such a population, the chromosomes evaluation, selection and reproduction are carried out iteratively in order to obtain, after a certain number of generations, an optimal chromosome  $\boldsymbol{\xi}^*$  corresponding to the optimal parameter set  $\boldsymbol{\pi}^*$ . In this way the optimal steering strategy  $S^*$  is also found and the optimization problem solved [Dachwald, 2004, p.37].

#### 4.2.2. ARCHITECTURE

The ENC optimization presented in the previous section constitutes the basic working principle of InTrance. Being an optimizer that makes use of both ANNs and EAs, this software results useful in solving many different trajectory optimization problems and, in order to effectively tackle them, it leaves plenty of freedom to the user in choosing parameters such as the ANN topology, neuron activation function, type of numerical integrator used for propagating the EoM, EA parameters and so forth. However, in spite of this strong versatility, InTrance always works in a recursive fashion by following the optimization procedure pattern schematically shown in Figure 4.3 [Dachwald, 2004, p.58] and described hereafter.

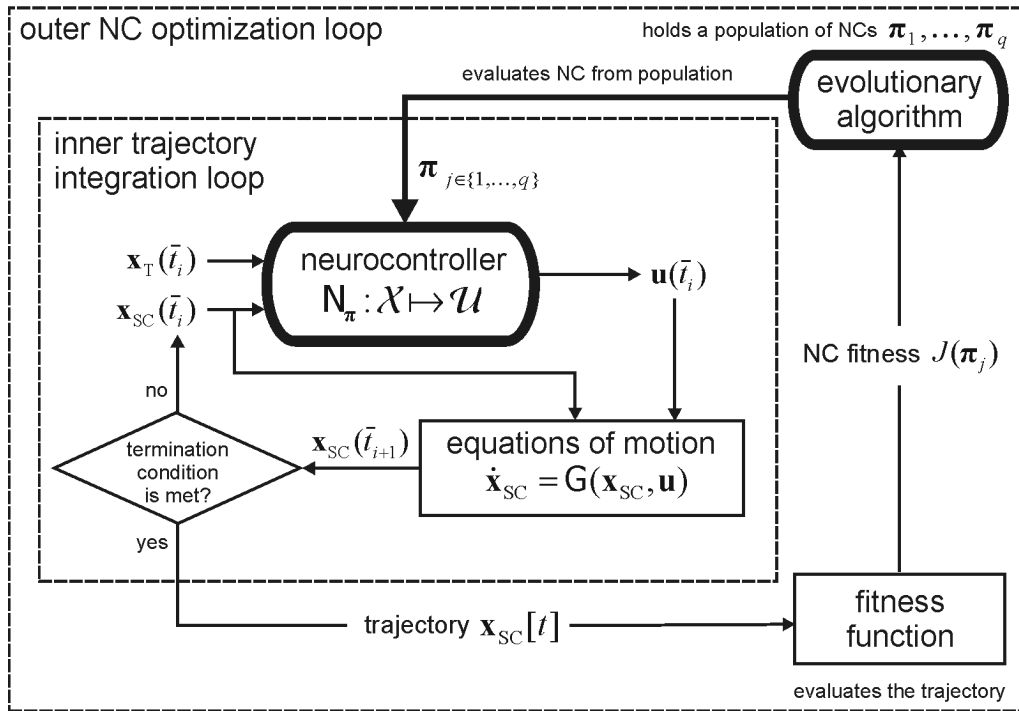


Figure 4.3: Representation of the iterative-fashioned optimization procedure used by InTrance, based on inner and outer optimization loops [Dachwald, 2004, p.58].

The optimization procedure is divided into an inner integration loop and an outer optimization loop used for different purposes. Within the inner loop, a parameter set  $\boldsymbol{\pi}_j$  selected from a population  $\Xi_{\boldsymbol{\pi}}^k = \{\boldsymbol{\pi}_1, \dots, \boldsymbol{\pi}_q\}$  is used to "create" a neural network that in turn is exploited to compute the control history of a S/C from departure until arrival at target. For each integration time instant  $\bar{t}_i$ , the ANN is exploited to compute the

control vector  $\mathbf{u}(\bar{t}_i)$  based on the S/C state  $\mathbf{x}_{SC}(\bar{t}_i)$ , target body state  $\mathbf{x}_T(\bar{t}_i)$  and possibly other input parameters (e.g. the S/C propellant mass). The control vector retrieved is then used together with the S/C state to integrate the EoM to the next time instant  $\bar{t}_{i+1}$  and therefore obtain a propagated state  $\mathbf{x}_{SC}(\bar{t}_{i+1})$  to be given as input to the neurocontroller once again. Such a process is recursively carried out until a termination condition is met, meaning that the trajectory has either reached the pursued target state (within a certain tolerance) or a user-defined maximum TOF limit.

After this phase, the flow of information moves out of the inner integration loop, where the computed trajectory  $\mathbf{x}[t]$  is evaluated by means of a fitness function  $J$ . The way such a function is defined depends on the type of optimization problem concerned; e.g. in the case a flight time-optimal rendezvous trajectory is sought,  $J$  obviously considers the TOF required but also other parameters such as the S/C final distance or relative velocity with respect to the target body. In this way the trajectory can be effectively evaluated and, with it, the set of neural parameters  $\boldsymbol{\pi}_j$  used to compute the trajectory itself.

The above-presented procedure leading to an evaluation  $J(\boldsymbol{\pi}_j)$  can be repeated for all parameter sets of the population  $\Xi_{\boldsymbol{\pi}}^k$ . The main reason for which such evaluations are computed is to associate each parameter vector to a reproduction probability value that can be successively used to perform an EA. Indeed, after having evaluated them, all vectors  $\boldsymbol{\pi}_j$  of the population  $\Xi_{\boldsymbol{\pi}}^k$  are mapped onto different chromosomes, hence creating a chromosome population  $\Xi_{\boldsymbol{\xi}}^k$  on which an EA can be carried out to yield an offspring. In this way a new population  $\Xi_{\boldsymbol{\xi}}^{k+1}$  of (improved) chromosomes is obtained which can be mapped back into parameter sets, hence yielding a new population  $\Xi_{\boldsymbol{\pi}}^{k+1}$  of  $\boldsymbol{\pi}$  vectors. Eventually, such a population can be exploited once again to run another iteration of the outer optimization loop and repeat the entire process from the start. In such a way new populations of neural parameter sets are recursively created and their fitness continuously improved, so that, after a certain number of iterations, the process converges and the optimal set  $\boldsymbol{\pi}^*$  corresponding to the near-globally optimal trajectory  $\mathbf{x}_{SC}^*$  is found [Dachwald, 2004, pp.57-58].

The above-presented optimization procedure can be carried out once an initial chromosome population  $\Xi_{\boldsymbol{\xi}}^0$  is provided. To retrieve this, InTrance considers a number  $n_H$  of different randomly chosen regions  $H$  of the chromosome search space and, for each of them, assesses the regional best chromosome  $\boldsymbol{\xi}_H$ . A comparison of these sub-optimal chromosomes is then used to understand which region of the search space is most promising so that, after the choice is made, the real optimization procedure as represented in Figure 4.3 can take place.

Hereafter these assessment procedures used to retrieve the regional optimal chromosomes will be referred to as search scan epochs (SSEs).

### 4.2.3. OPTIMIZATION OUTPUTS

Another important aspect to discuss concerns the output information returned by InTrance at the end of each optimization run. This optimizer creates a "comma-separated values" file with different parameters stored inside of it, used to define the control variables' histories and the corresponding (optimal) trajectory found. For example, in the case traditional solar sailing is concerned, the control variables are the pitch angle  $\alpha$

and clock angle  $\delta$ , which are stored in the form of arrays. In particular, within each integration step these attitude angles are considered to be fixed and, therefore, if the trajectory is divided into  $N$  steps,  $N + 1$  values of  $\alpha$  and  $\delta$  are returned by the optimizer (since their initial and terminal values are also included). Hence their histories  $\alpha[t]$  and  $\delta[t]$  will be arrays of  $(N + 1)$  values, indeed. Besides these angles, the output file also provides other useful information through other  $(N + 1)$ -dimensional vectors, such as the sailcraft acceleration components, Cartesian coordinates, spherical coordinates and Keplerian elements, hence making it possible to unequivocally define the final (optimal) trajectory  $\mathbf{x}[t]$  found.

All the above holds also for laser-enhanced sails, with the only difference being that, in this case, also other variables are returned after each time step. These are the LS state components (in Cartesian and spherical coordinates), LRP acceleration components, the laser pitch angle, and different boolean variables used to determine when the LG is powered off (i.e. when  $\chi = 0$ ).

# 5

## IMPLEMENTATION AND VALIDATION

Since laser-enhanced solar sailing has been implemented within InTrance from the ground up, in this chapter the C++ architecture of the program is described, and all modifications actually pursued are presented. In addition to this, also the validations of the LRP acceleration model, LG powering-off scenarios and laser-enhanced solar sailing optimization procedure are discussed, with a view to showing the correct implementations of all these newly added functionalities.

### 5.1. LASER-ENHANCED SOLAR SAILING IMPLEMENTATION WITHIN INTRANCE

InTrance is a software written in C++ and, as such, it can be compiled through commercially available development environments such as Microsoft Visual Studio to yield an executable file. However, in order to generate such a file, three other C++ libraries must be compiled first, which form the computational core of the software. These are:

- SpaceLib: Within this library all classes used for defining space objects like planets, moons, asteroids and comets in terms of dimensions, gravity potential and ephemeris are given. Apart from this, also mathematical constants, planetary constants and classes for numerical integrators, reference frames and rotation models are provided.
- SCLib: Here the classes used to define and fully characterize a S/C are given. Among these are the ones to model propulsion systems, solar sails, steering control and attitude control.
- ENCLib: This library contains all functionalities actually related to ENC and therefore all C++ interfaces for ANNs, neurons, chromosomes, EA operations (such as mutation, crossover, selection, etc.), evaluation functions and so forth.

Since SCLib contains classes to model only traditional solar sails but not laser-enhanced ones, one of the first tasks to fulfill has been the C++ design of laser-enhanced sailcraft as a new propulsion system to implement within InTrance. Such a design has

been carried out following the same object-oriented programming philosophy used to design many other classes within SCLib, among which is also the traditional solar sail one, for instance.

From a general point of view, the laser-enhanced solar sailing implementation process may be considered to be divided into three phases: creation of the LG subsystem class and of the S/C used as LS, creation of the laser-enhanced solar sail propulsion system class, and actual implementation of these classes within InTrance to perform trajectory optimization.

### LASER GENERATOR SUBSYSTEM AND LASER SOURCE DESIGNS

Within this phase the first design step has been the creation of the LG subsystem class, characterized by parameters such as the laser wavelength  $\lambda$ , collimating lens diameter  $D$ , wall-plug efficiency  $\eta_{wp}$ , required power  $W_{LG}^{in}$  and throttle  $\chi$ . Secondly, a S/C object mounting this LG subsystem has been created with a view to representing the LS. In this context the major design choice concerned the way the LS orbit has been defined, i.e. by means of user-defined Keplerian elements and their rates of change, rather than through numerical propagation of the LS state. Despite the latter method is theoretically more accurate (as the LS state is retrieved directly from its EoM), the use of orbital elements yields a strong reduction of the overall computational effort required to run the optimizations, while providing realistic and easily interpretable trajectories. This applies particularly to the mission scenarios analyzed within this work, as for all of them the LSs have been placed in the Earth or Venus orbits and thus their orbital elements could be easily retrieved from the planetary ephemeris.

### LASER-ENHANCED SOLAR SAIL DESIGN

In order to create the laser-enhanced solar sailing propulsion system class, the entire design has been based on the already-existing traditional solar sail class, with the only difference being that, to make a laser-enhanced solar sail actually work, an LS object has to be necessarily specified. Moreover, it should be noted that such a design has been carried out implementing only the IR sail model, as the use of other (more complex) sail models was out of the scope of this work.

An important characteristic of this propulsion system design concerns the way the LG throttle  $\chi$  is determined during the sailcraft flight. In fact, it was decided to let InTrance determine when to set  $\chi$  equal to 0 or 1 (LG powered off or on, respectively), depending on the Sun-sailcraft-LS relative position. More specifically, the LG is always assumed to be powered on, unless one of the following situations takes place:

- The laser beam is directed towards the back-side of the sail and therefore it is powered off to prevent the back-side material from getting damaged. From a mathematical point of view, this situation translates into having  $\alpha_L \geq 90$  deg so that, to avoid this, it was decided to set  $\chi = 0$  any time that  $\alpha_L > (90 \text{ deg} - \varepsilon)$ , with  $\varepsilon$  being a safety margin equal to 5 deg.
- The laser beam is directed towards the Sun which prevents it from reaching the sailcraft. According to [Davidovich and Whittington, 1999, p.217], the solar radiation interference (SRI) region can be modeled as a sphere centered in the Sun with radius ranging between  $7.86 \cdot 10^6$  km and  $18.06 \cdot 10^6$  km, depending on the solar activity. Based on these values, it was decided to consider an average SRI radius  $R_{SRI}$  of  $12.96 \cdot 10^6$  km so that, any time the laser vector  $\mathbf{s}$  intersects such sphere,  $\chi = 0$

automatically set.

- The LS is too close to the sailcraft and therefore the sum of laser and solar fluxes impinging the sail gets greater than a given threshold, imposed to prevent the sail material to get damaged. Such a threshold value was determined based on the minimum heliocentric distance usually allowed for traditional solar sails. As given in [Dachwald, 2005, p.1191], at a distance of 0.2 AU from the Sun the temperature of a solar sail can reach values in the order of 260 °C but, nonetheless, sail film materials as Kapton can safely withstand temperatures in the range 250 – 290 °C, even for large periods of time [McInnes, 1999, p.62]. Therefore the above-mentioned threshold was chosen to be equal to the solar flux achieved at 0.2 AU, i.e.  $25S_0$ .

### LASER-ENHANCED SOLAR SAILING IMPLEMENTATION WITHIN INTRANCE

The implementation of the above-mentioned classes within InTrance has been carried out with the aim of letting the user easily setup the simulations through input files. In fact InTrance has been designed in order to receive inputs from the user by means of different text files containing parameter specifications concerning the simulation setup, propulsion system characteristic, the EA used within ENC and so forth. In this context it was decided to give a large amount of freedom to the user to choose the LS trajectory (from a list of predefined available orbits), the solar sail characteristics (in terms of sail equivalent diameter and characteristic acceleration) and LG specifics (i.e. the variables  $\lambda$ ,  $D$ ,  $\eta_{wp}$  and  $W_{LG}^{in}$ ).

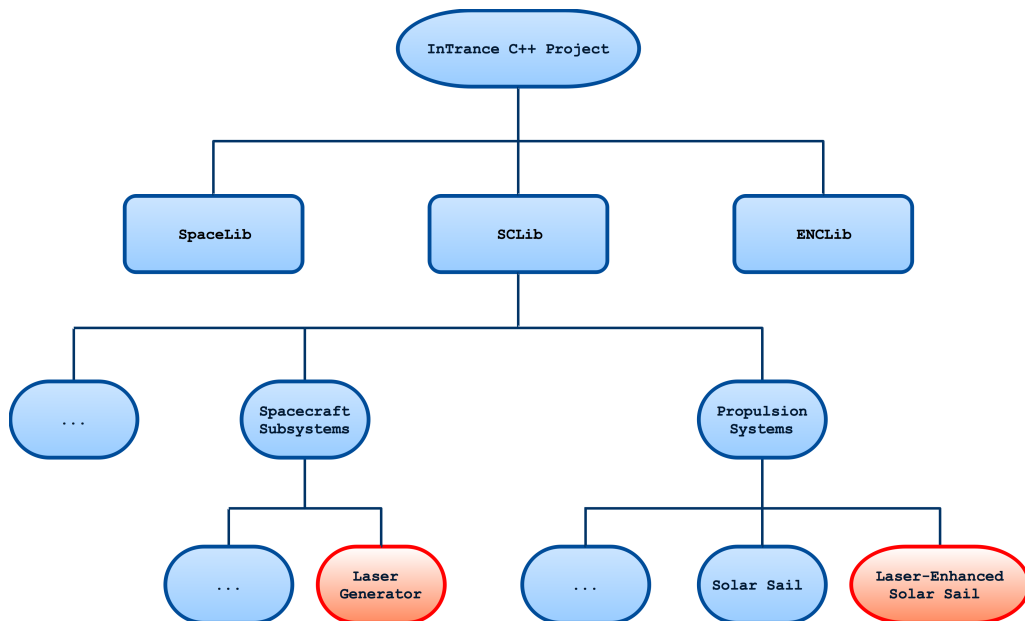


Figure 5.1: Diagram showing the InTrance program architecture. The red boxes indicate the new classes implemented.

For the sake of clarity, Figure 5.1 shows a sketch of the program architecture while Section A.2 of Appendix A provides a list of all files created and modified to implement laser-enhanced solar sailing within InTrance. As can be seen, most of the newly added files and modifications regard SCLib and the InTrance project. In particular ENCLib has been the only library not being edited, meaning that the optimizer itself has not

been modified and therefore that the optimization procedure presented in Section 4.2 has been exploited for the simulations. More specifically, the ANN structure used for optimizing traditional and laser-enhanced solar sailing trajectories has been the same. This comprises a user-defined number of input neurons that represent the sailcraft and target states (which can be expressed in Cartesian coordinates, spherical coordinates, Keplerian elements or combinations of these), a user-defined number of hidden layers and an output layer made up by three neurons which provide the control vector  $\mathbf{u}$  representing the direction in which the sail unit vector  $\hat{\mathbf{n}}$  shall point.

Since such an ANN structure has been specifically designed for traditional solar sails but not for laser-enhanced ones, its exploitation also for laser-enhanced solar sailing trajectories actually affects the optimizer robustness. Such an issue is due to the fact that the neural network bases its steering strategy on the information passed on by the input neurons, which is only related to the sailcraft and target states but not to the LS state. In other words, this means that the ANN finds the optimal trajectories by "reasoning" only on the position of one of the two radiation sources, i.e. the Sun, but not on the LS. However, on the other hand, the EA selects the best network function based on the trajectories' flight times, which are indeed influenced by the presence of the LS. This problem related to the optimization process has been identified after having implemented the laser-enhanced solar sailing propulsion system, mainly thanks to the results provided by preliminary optimization runs. However, since the design of a new type of neural network required a high amount of time and was out of the scope of this project, it was decided nonetheless to use the same ANN exploited for traditional solar sails also for laser-enhanced ones. To counteract the reduced robustness of the optimizer, a high number of laser-enhanced solar sailing trajectory optimization runs have been carried out, with a view to increasing the total number of SSEs performed and thus scan the search space more extensively in a similar fashion to Monte Carlo optimization. Moreover, as will be seen in Chapter 7, the solutions found in this way have also been refined by shrinking the allowed sailcraft departure date time span and exploiting sub-optimal chromosomes, with a view to performing sort-of local optimizations.

## 5.2. VALIDATION OF LASER RADIATION PRESSURE ACCELERATION MODEL

In order to actually exploit laser-enhanced solar sailing within InTrance, the LRP acceleration model has been implemented within SCLib and validated. In particular, two different validation tests have been designed: a first one used to verify the correct encoding of the LRP acceleration dependency on the critical laser distance, and a second one designed to actually validate the entire LRP acceleration model itself.

### 5.2.1. DEPENDENCY ON CRITICAL LASER DISTANCE

As presented in Section 3.5, depending on the ratio  $\tilde{s}/s$ ,  $P_L$  can be either a constant value or an inverse square law function of  $s$ . As a consequence, within SCLib a specific function used for determining the right expression of  $P_L$  based on  $\tilde{s}/s$  has been designed and its validation is presented hereafter.

In the scenario used, the LS is fixed in the origin of a Cartesian inertial frame, generating a laser beam with divergence equal to  $\theta = 10^{-8}$  rad and beam power  $W_L$  of  $8 \cdot 10^6$  W. The sailcraft is initially placed normally with respect to the laser light at a distance  $s_0$  of only  $\sim 1.5$  m ( $10^{-11}$  AU) from the LS, has a lightness number  $\beta$  of 0.1 and an equivalent diameter of 150 m. In this way it results that the critical laser distance is  $\tilde{s} = 1.5 \cdot 10^{10}$  m  $\approx 0.10027$  AU, i.e. much greater than  $s_0$ . In particular, such a small value of  $s_0$  has been used as an approximation to make the sailcraft and LS share the same position at departure, as setting  $s_0 = 0$  AU led to singularities in the integration of the EoM. Eventually it should be noted that, for this test case, the LG powering-off functionalities presented in Section 5.4 have not been used.

Within this scenario, as soon as the LG is activated, the sailcraft experiences a constant acceleration until reaching the critical laser distance  $\tilde{s}$ , whereas afterwards the acceleration is proportional to  $1/s^2$ . Based on this theoretical modeling, [McInnes, 1999, p.275-278] provides the equations for computing the time instant  $\tilde{t}$  at which  $s = \tilde{s}$ , i.e.:

$$\tilde{t} = \sqrt{\frac{2\tilde{s}}{a_{L,0}}} \quad (5.1)$$

where

$$a_{L,0} = a_L(s < \tilde{s}) = 2 \frac{W_L}{\sigma c A} \quad (5.2)$$

is the constant LRP acceleration achieved for  $s < \tilde{s}$ . Substitution of the simulation setup parameters into Equation 5.2 and implementation into Equation 5.1 eventually yields  $\tilde{t} = 143.104$  days. This means that, for the present scenario, the LRP acceleration shall theoretically experience a discontinuous change for  $t = \tilde{t}$ .

To verify whether this is the case, the sailcraft EoM have been integrated over a 2-year time span using a Runge-Kutta (RK) integrator of order 4 with a step-size of 0.01 days. The integration results given in Figures 5.2 and 5.3 show that  $a_L$  remains constant for 143.1 days, hence defining a linear growth of the sailcraft velocity and a parabolic increase of the distance traveled. On the other hand, beyond  $t = 143.1$  days the LRP acceleration suddenly decreases as  $1/s^2$ , thus making  $\dot{s}$  to stabilize and  $s$  to become almost linear in time. The LRP variation in time can be better appreciated in

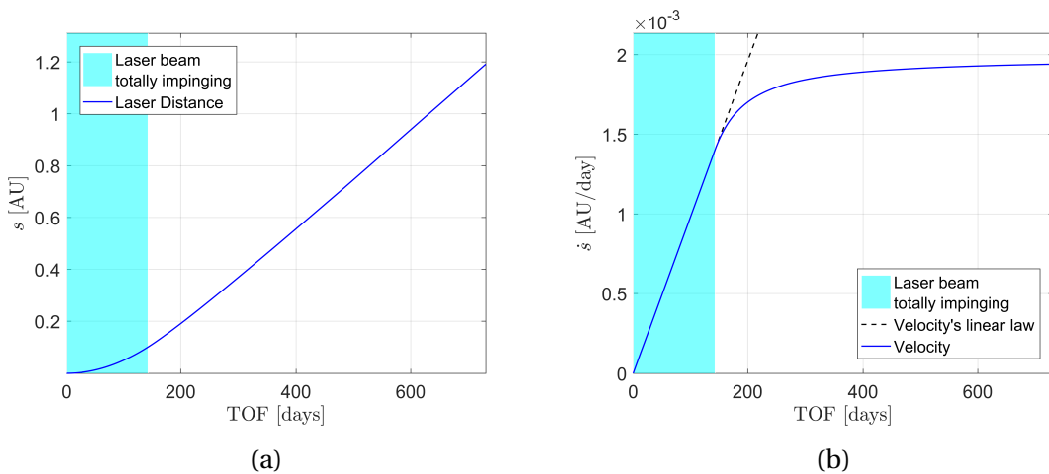


Figure 5.2: Distance travelled (a) and velocity (b) of the sailcraft as a function of time.

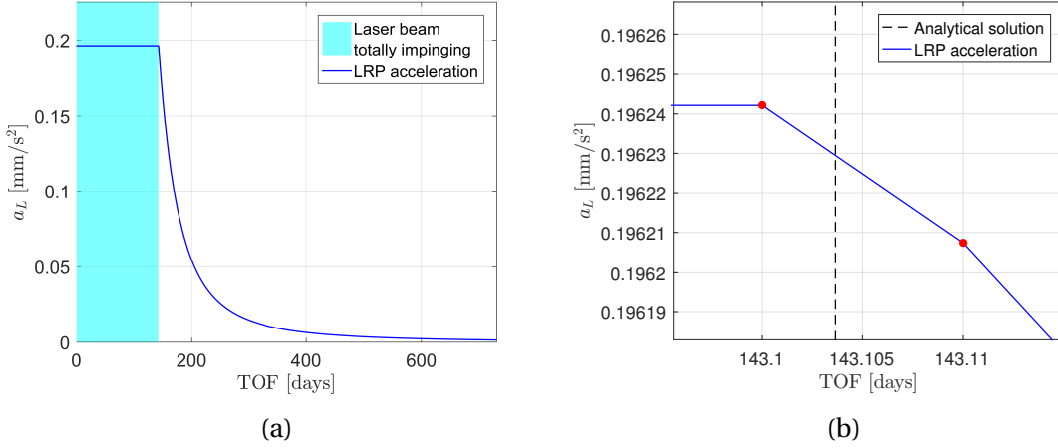


Figure 5.3: LRP acceleration as a function of time (a) and comparison between analytical and numerical solutions found for  $\tilde{t}$  (b).

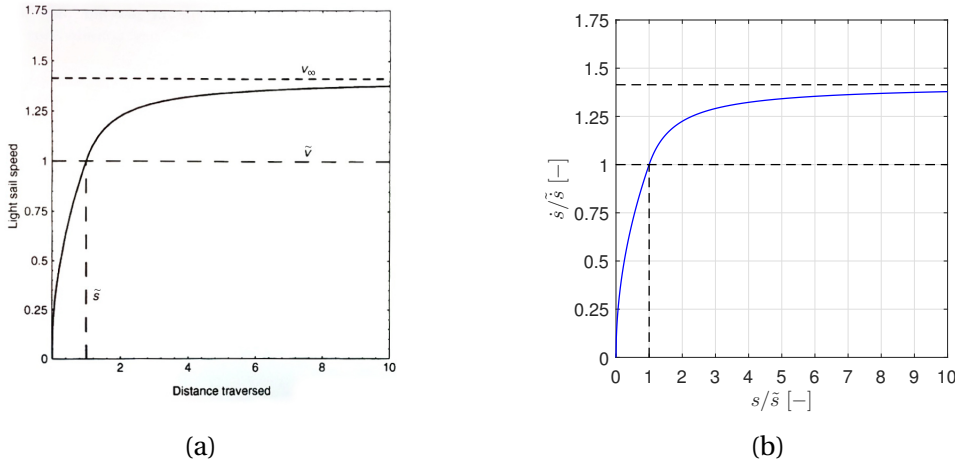


Figure 5.4: Laser-pushed sailcraft velocity as a function of the distance traveled (both given in adimensional units). (a) shows the graph provided in [McInnes, 1999, p.277], (b) is the result of numerical computation.

Figure 5.3a while, on the other hand, Figure 5.3b shows the comparison between the analytical solution found for  $\tilde{t}$  and the numerical one, respectively represented by the dashed line and the red marks. It can be seen that the last integration step for which  $a_L$  is constant is at  $t_a = 143.10$  day, whereas for  $t_b = 143.11$  day it has already started decreasing. Since  $t_a < \tilde{t} < t_b$ , such numerical results are in accordance with the expectations and prove the correct implementation of the laser distance check to compute the LRP.

After having proven that a sudden decrease in the LRP acceleration takes place, it is also possible to verify the correctness of the integration results achieved in terms of  $s$  and  $\dot{s}$ . In fact, in [McInnes, 1999, pp.275-278] the same scenario as discussed above is analyzed, and the dependency of  $\dot{s}$  as a function of  $s$  is represented as given in Subfigure 5.4a. The same graph has been reproduced also with the numerical integration results achieved, shown in Subfigure 5.4b. As can be seen, the results found in the simulation agree with the theoretical ones as both graphs show the same depen-

dency. In particular, both plots show that the adimensional velocity rapidly increases until  $s/\tilde{s} = 1$ , while beyond this value it decreases its rate of change in order to tend to  $\dot{s}/\tilde{s} = \sqrt{2}$ . Such a value is indeed a maximum (asymptotic) velocity, as given in [McInnes, 1999, p.276].

### 5.2.2. LASER RADIATION PRESSURE ACCELERATION

Although the graphic-based validation presented above gives confidence that the LRP acceleration implementation within SCLib is correct, also a more detailed test has been designed to actually validate this numerically. To fulfill this task, two different trajectories have been compared:

- (A) The trajectory of a traditional solar sail accelerated only by the SRP and solar gravitational force
- (B) The trajectory of a laser-enhanced sailcraft accelerated by the LRP and solar gravitational force, but not by the SRP

Although scenario (B) is unrealistic as the Sun irradiates isotropically in space, it serves for the purpose of validating the LRP acceleration model. In fact, the LS has been put at the center of the Solar System with values of  $W_L$ ,  $D$  and  $\lambda$  specifically chosen to make it irradiate the sailcraft with a laser flux exactly equal to the solar one. In this way, in both scenarios the amount of photons impinging the sail is the same. Therefore, in spite of the different EoM used, the corresponding trajectories should be equal.

The LS power required for the trajectory (B) has been calculated by equating the amount of radiation power per unit of solid angle provided by the LS and the Sun, i.e.:

$$\frac{\mathcal{L}_{\odot}}{4\pi} = \frac{W_L}{\Omega} \quad (5.3)$$

with  $\Omega$  being the solid angle defined by the laser beam diffraction angle  $\theta$ , i.e. [Schubert et al., 2005, p.270]:

$$\Omega = 2\pi [1 - \cos(\theta/2)] = 4\pi \sin^2(\theta/4) \quad (5.4)$$

where the trigonometric relation  $1 - \cos x = 2\sin^2(x/2)$  has been because, in this way, the expression on the RHS of Equation 5.4 is less affected by numerical errors, especially for small values of  $\theta$  [Hatch, 2017]. The above equation has been used to compute  $\Omega$  and therefore  $W_L$ . In particular,  $\theta$  was set to  $10^{-8}$  rad  $\approx 5.73 \cdot 10^{-7}$  deg since in this way the constraint given in Equation 5.3 has been numerically respected (meaning that the difference between left-hand side (LHS) and RHS of the equation was numerically equal to 0).

In both scenarios (A) and (B) the sailcraft has an equivalent sail diameter of 150 m, a lightness number of 0.1 and is supposed to depart from a circular orbit with radius of 1 AU, inclined by 30 deg. Along the trajectories the pitch angle is kept constant with a value of 35.26 deg (i.e. the optimal pitch angle for maximizing the acceleration in the transversal direction  $\hat{\mathbf{d}}$  of the  $\mathcal{O}$ -frame [Wie, 2004, p.529]), while the clock angle varies in the range  $[-45$  deg,  $+45$  deg] as a sinusoid with a period of 1 year. The trajectories have been numerically integrated over a time span of 10 years using an RK integrator of the 4<sup>th</sup> order with step-size of 1 day. The simulation parameters for both case scenarios are also presented in Table 5.1.

Table 5.1: Simulation parameters used for the scenarios (A) and (B).

Scenario	Parameter	Value
(A) and (B)	Sail equivalent diameter	150 m
	Lightness number	0.1
	Pitch angle	35.26 deg
	Clock angle	$45 \text{ deg} \cdot \sin\left(\frac{2\pi t}{1 \text{ year}}\right)$
	Initial semi-major axis	1 AU
	Departure orbit radius	1 AU
	Departure orbit eccentricity	0
	Departure orbit inclination	30 deg
	Integrator	RK4, step-size 1 day
	Integration time	3653 days (~10 years)
(B)	LS position	Origin of $\mathcal{S}$ -frame
	Laser beam divergence angle	$5.73 \cdot 10^{-7} \text{ deg}$ ( $10^{-8} \text{ rad}$ )
	Laser beam power	$2.40 \cdot 10^9 \text{ W}$
	Laser flux at 1 AU	$1368 \text{ Wm}^{-2}$

In order to validate the LRP acceleration implementation, the sailcraft trajectory (B) has been integrated using spherical coordinates and the achieved results have been subtracted from the ones of scenario (A). This has been done using two different rotation methods to calculate  $\alpha_L$  (as will be discussed in the next section), resulting in the plots given in Figure 5.5 (with the axis units being the same used for the numerical integration of the EoM).

These graphs show that the errors defined are always smaller than  $10^{-13}$  AU or  $10^{-13}$  rad for the position coordinates, and that their rates of change are always smaller than  $10^{-15}$  AU/day or  $10^{-15}$  rad/day. The small magnitude of these errors and their irregular trends (especially during the first days of flight) suggest that these errors are mostly due to floating-point inaccuracies, which in turn are due to the different operations performed for retrieving the SRP and LRP accelerations in the scenarios (A) and (B), respectively. However, since the error magnitudes are small and, more specifically, in the order of the machine epsilon  $\epsilon = 2.2204 \cdot 10^{-16}$ , they prove the correct modeling and implementation of the LRP acceleration within SCLib.

### 5.3. COMPUTATIONAL PERFORMANCES OF DIFFERENT FRAME ROTATION METHODS

Besides validating the LRP acceleration model, the above simulations have also been run for comparing the performance of two different methods used for computing the laser pitch angle  $\alpha_L$  during trajectory integration. Since  $\alpha_L$  represents the angle between  $\hat{\mathbf{s}}$  and  $\hat{\mathbf{n}}$ , one way to retrieve it is by expressing both these unit vectors within the  $\mathcal{O}$ -frame to determine the angle between them as:

$$\alpha_L = \text{atan2}(\|\hat{\mathbf{n}} \times \hat{\mathbf{s}}\|, \hat{\mathbf{n}} \cdot \hat{\mathbf{s}}) \quad (5.5)$$

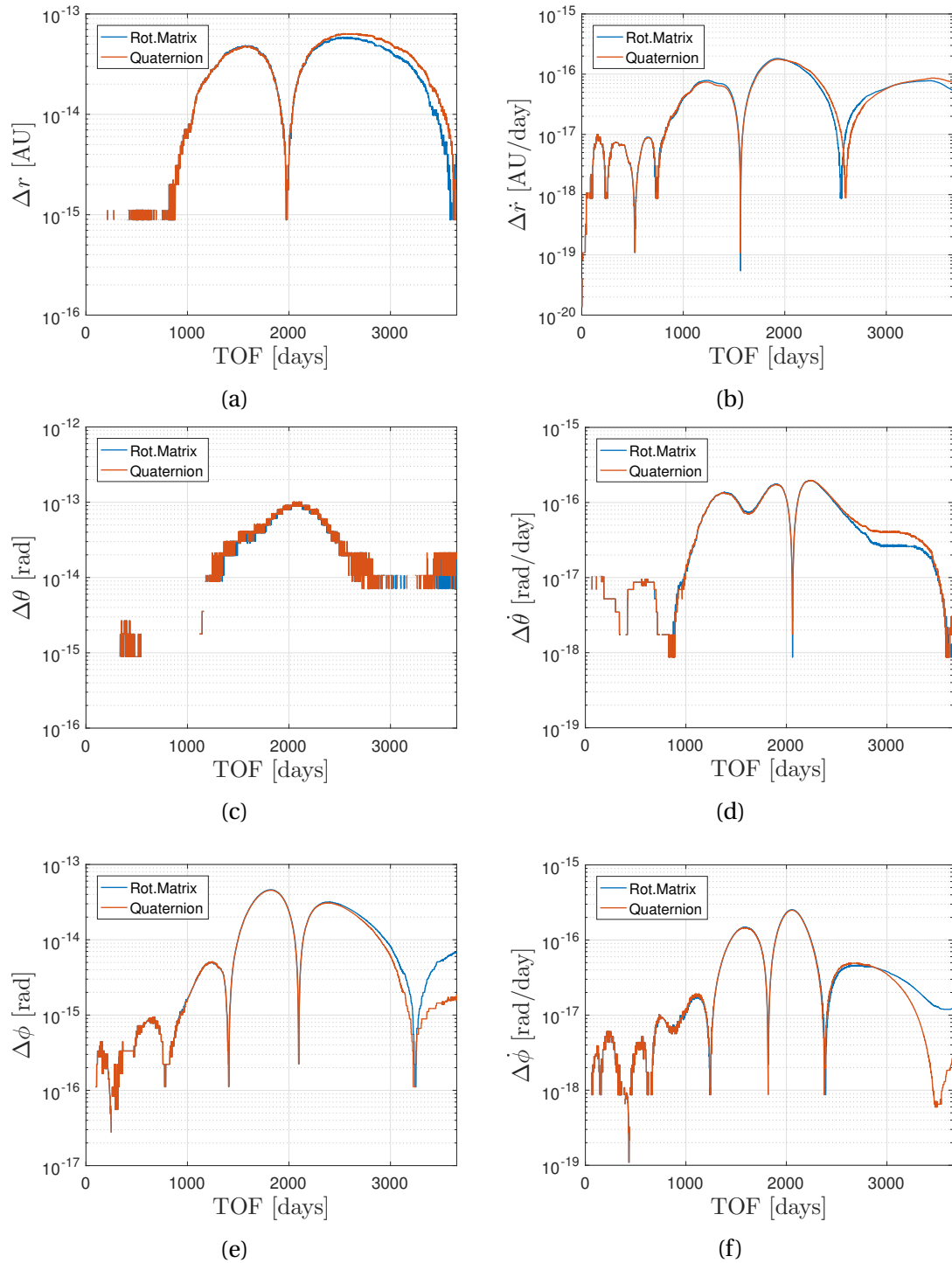


Figure 5.5: Difference between the sailcraft spherical coordinates computed in scenarios (A) and (B). Subfigures (a) to (f) show the differences in the orbital radius, orbital radius rate of change, azimuth, azimuth rate of change, elevation and elevation rate of change, respectively. The plots' axis units are the same used for the numerical integration of the EoM.



during the integration process, which are due to the different operations actually performed when rotating the  $\mathcal{F}$ -frame using quaternions or rotation matrices. Besides the numerical precision, these rotation methods have been compared also in terms of computational speed. More specifically, the numerical integration of trajectory (B) has been performed 1000 times using both methods while measuring the total computational time required for the operation. A comparison of these time lapses showed that quaternion-based rotations are on average 6.5% faster than the rotation-matrix-based ones. As a consequence, despite such a small computational gain, it was decided to implement the quaternion-based rotation method inside SCLib for computing  $\alpha_L$ .

## 5.4. VALIDATION OF LASER GENERATOR POWERING-OFF SCENARIOS

The following validations have been carried out considering only the in-plane motion of sailcraft and LSs, with a view to making the problem treatment bi-dimensional. The laser-enhanced sailcraft considered have a lightness number  $\beta$  equal to 0.1 and a sail equivalent diameter  $d = 150$  m, whereas the laser beams' power  $W_L$  and divergence angle  $\theta$  have been set respectively to  $1.20 \cdot 10^9$  W and  $10^{-8}$  rad in order to provide a laser flux at 1 AU (hereafter referred to as laser constant  $L_0$ ) equal to  $0.5S_0$ . For all scenarios the laser-enhanced sailcraft EoM have been integrated using an RK4 integrator with a step-size of 0.05 days.

### 5.4.1. SOLAR SAIL BACK-SIDE EXPOSURE

To validate the implementation of this LG powering-off scenario, a laser-enhanced sailcraft placed in a circular orbit at a distance  $r_{sc} = 1$  AU from the Sun and oriented normally with respect to the Sun line ( $\alpha = 0$  deg) has been considered. On the other hand, the LS has been placed in a circular orbit at a distance  $r_{LS} = 1.5$  AU in such a way as to make its location being exactly on the Sun-sailcraft direction at departure.

When considering a rotating frame centered in the Sun with an axis fixed along the Sun-LS direction, the geometry of the problem can be represented as given in Figure 5.7. Since at departure the LS is placed behind the sailcraft in the along-track direction, in the first flight segment the LG will be powered off until the moment in which the laser pitch angle gets equal to  $\alpha_{L,lim} = 85$  deg (since the safety margin  $\varepsilon$  is equal to 5 deg). In such a situation the following relations describing the sailcraft-LS-Sun configuration hold:

$$\begin{cases} s^2 = r_{sc}^2 + r_{LS}^2 - 2r_{sc}r_{LS} \cos(\gamma_{lim}) \\ r_{sc} = r_{LS} \cos(\gamma_{lim}) + s \cos(\alpha_{L,lim}) \end{cases} \quad (5.8)$$

so that, by solving this system of equations with respect to  $\gamma_{lim}$  one finds:

$$\gamma_{lim} = \arccos\left(\frac{r_{sc} - s \cos(\alpha_{L,lim})}{r_{LS}}\right) \quad \text{or} \quad \gamma_{lim} = 2\pi - \arccos\left(\frac{r_{sc} - s \cos(\alpha_{L,lim})}{r_{LS}}\right) \quad (5.9)$$

with

$$s = r_{sc} \left( \cos(\alpha_{L,lim}) + \sqrt{\frac{r_{LS}^2}{r_{sc}^2} + \cos^2(\alpha_{L,lim}) - 1} \right) \quad (5.10)$$

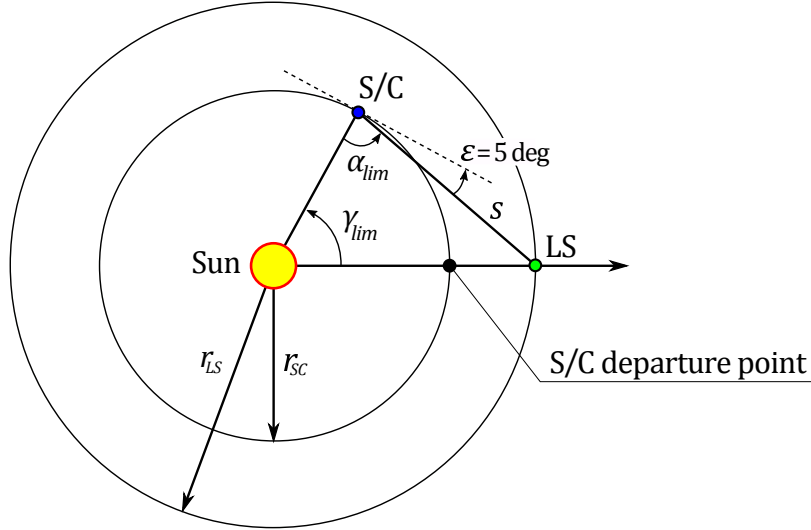


Figure 5.7: Geometry of the scenario considered for validating the powering-off due to solar sail back-side exposure.

If one substitutes  $r_{sc} = 1$  AU,  $r_{LS} = 1.5$  AU,  $\alpha_{L,lim} = 85$  deg, and considers only the solution for which  $\gamma_{lim} < 180$  deg, eventually it results  $\gamma_{lim} = 53.384$  deg.

Due to the SRP acceleration exerted on the sail and the different orbital radii, the sailcraft and LS have mean motions respectively equal to [Wakker, 2015, p.164][McInnes, 1999, p.123]:

$$n_{sc} = \sqrt{\frac{\mu_{\odot} (1 - \beta)}{r_{sc}^3}} \quad (5.11a)$$

$$n_{LS} = \sqrt{\frac{\mu_{\odot}}{r_{LS}^3}} \quad (5.11b)$$

Given these, the relative angular velocity of the sailcraft with respect to the Sun-LS axis can be expressed as:

$$n_{rel} = n_{sc} - n_{LS} \quad (5.12)$$

so that, eventually, it results that  $n_{rel} = 4.612 \cdot 10^{-6}$  degs<sup>-1</sup>.

The  $\gamma_{lim}$  and  $n_{rel}$  values computed above can be used to determine the time between departure and LG powering-on as  $\Delta t = \gamma_{lim} / n_{rel}$ , so that eventually it results  $\Delta t = 133.952$  days. As a consequence the correct implementation of the sail back-side exposure check within SCLib will be verified by simulating the above-discussed scenario and verifying that the LG gets switched-on exactly after a time lapse equal to  $\Delta t$ . As given in Figure 5.8, the integration results show that the angle  $\alpha_L$  decrease from 180 deg until the limit value 85 deg after 133.952 days, as expected. More specifically, due to the discretization using a step-size of 0.05 days, the last time step for which the LG is powered off is achieved for  $t = 133.95$  days, while it gets powered on at  $t = 134.00$  days (these events are represented through the red dots in Figure 5.8b).

As can be seen in Figure 5.9, the LG activation defines a sudden rise of the LRP acceleration. Such an acceleration takes place discontinuously due to the presence of

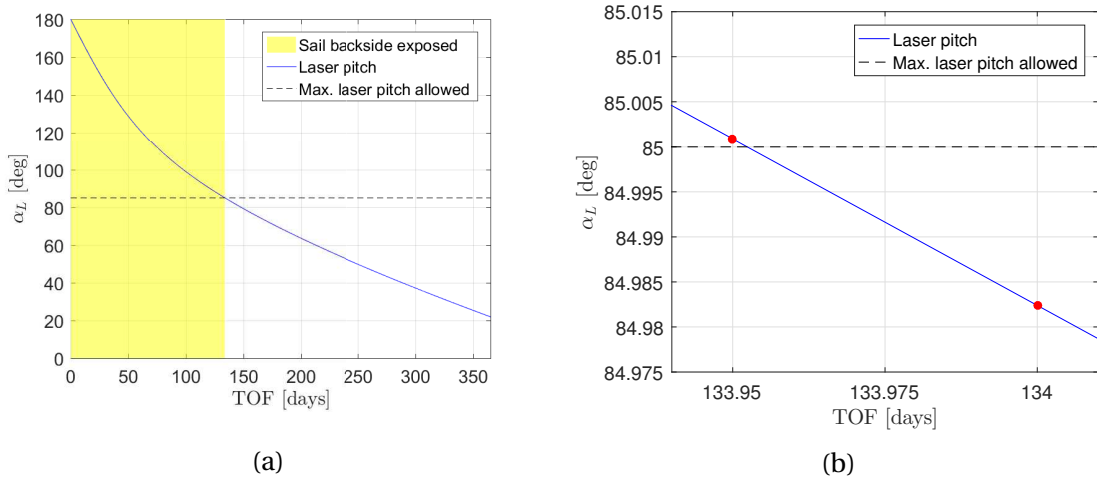


Figure 5.8: Laser pitch angle as a function of time (a) and visualization of the time step within which the LG is activated (b).

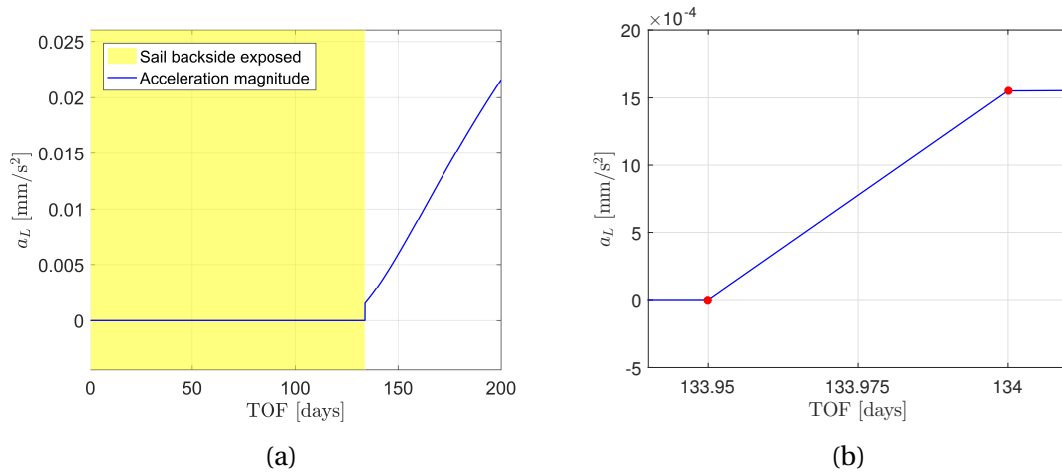


Figure 5.9: LRP acceleration as a function of time (a) and visualization of the discontinuity due to the LG activation (b).

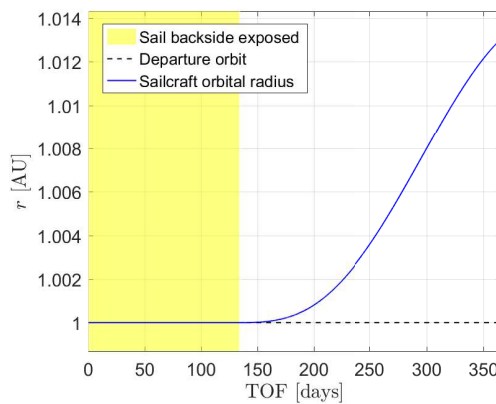


Figure 5.10: Orbital radius as a function of time.

the safety margin angle which makes the sail get illuminated when already tilted by 5 deg with respect to the laser direction. In order to better appreciate the effects of the LG activation, Figure 5.10 is also provided which shows the variation of the sailcraft orbital radius as compared to the one of the departure orbit. The continuous increase for  $t > 134.00$  days is uniquely due to the LRP acceleration, as without it the sailcraft would continue to orbit at 1 AU as done for  $t < 134.00$  days.

As the achieved numerical results match the analytical ones and actually show the clear performance difference due to the LG activation, the implementation of this LG deactivation scenario has been validated.

#### 5.4.2. SOLAR OCCULTATION

To validate the correct implementation of the LG deactivation in the case the laser direction intersects the SRI sphere, a simulation setup slightly different from the one presented in the last subsection has been exploited. In fact, the only difference concerns the departure positions of the satellites, since this time it was decided to put the sailcraft and LS both at 1 AU and diametrically opposed with respect to the Sun. In this way the latter lies in-between the sailcraft and LS, meaning that during the first flight phase the LG is powered off due to a solar occultation taking place. The geometry of this configuration is given in Figure 5.11. Based on the geometry of the problem it is possible to analytically compute the  $\Delta t$  required for exiting the "solar occultation" region. To this aim, it is possible to exploit the rotating reference frame presented in Subsection 5.4.1, so that Equations 5.11 and 5.12 can be reused by setting  $r_{SC} = r_{LS} = 1$  AU. This results in a relative mean motion of the sailcraft with respect to the LS equal to  $5.85395 \cdot 10^{-7}$  degs $^{-1}$ . As can be derived from Figure 5.11, the minimum Sun-LS-sailcraft angle required for exiting the "solar occultation" region is given by:

$$r_{LS} \sin(\phi_{lim}) = R_{SRI} \quad \Rightarrow \quad \phi_{lim} = \text{asin}\left(\frac{R_{SRI}}{r_{LS}}\right) \quad (5.13)$$

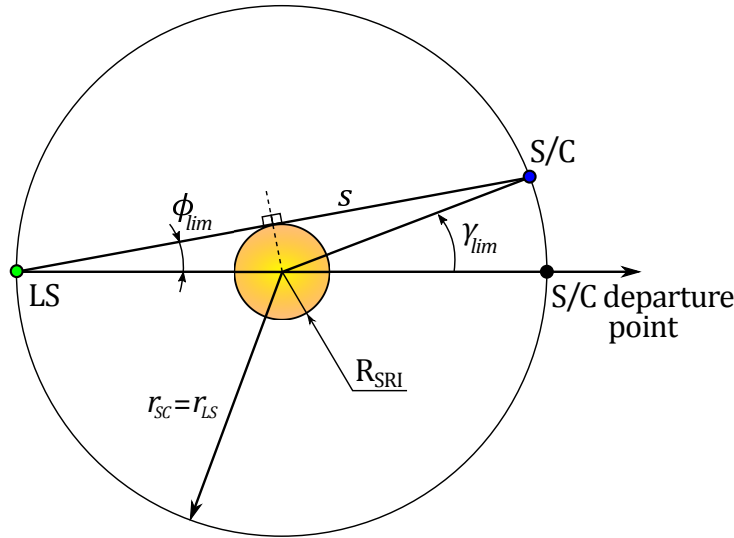


Figure 5.11: Geometry of the scenario considered for validating the powering-off due to solar occultation.

and therefore:

$$\gamma_{lim} = 2\phi_{lim} = 2 \operatorname{asin}\left(\frac{R_{SRI}}{r_{LS}}\right) \quad (5.14)$$

Since  $R_{SRI} \approx 8.6632 \cdot 10^{-2}$  AU while  $r_{LS} = 1.0$  AU,  $\gamma_{lim}$  is found to be 9.9398 deg. In the end, based on the values of  $n_{rel}$  and  $\gamma_{lim}$  found, it is possible to evaluate the time between departure and LG activation, which results to be  $\Delta t = \gamma_{lim} / n_{rel} = 196.52344$  days.

In order to validate the correct implementation of the LG powering-off due to solar occultation, the theoretical results shown above have been reproduced by numerically integrating the sailcraft EoM. The results of such an integration are given in Figures 5.12 to 5.14, which provide the variation of the LRP acceleration and orbital radius in time. As expected, these plots show that the LG is activated after 196.52344 days, hence yielding a discontinuity in the LRP acceleration and a strong increase of the orbital radius. In particular, by looking at Figure 5.13 it can be noted that, within the numerical approximation, the LG is activated between  $t = 196.5$  days and  $t = 196.55$  days. Since the analytical solution is right in-between these values, such a result validates the solar occultation check implemented within SCLib.

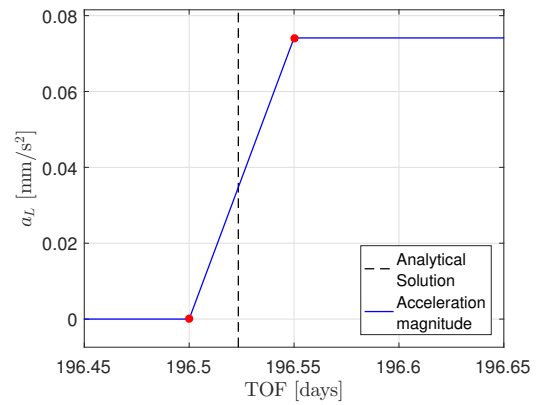
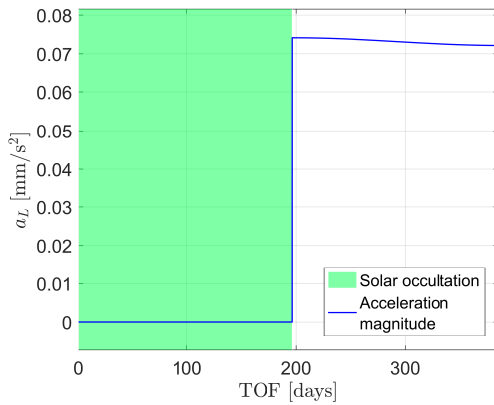


Figure 5.12: LRP acceleration as a function of time. Figure 5.13: LRP acceleration discontinuity due to the LG activation.

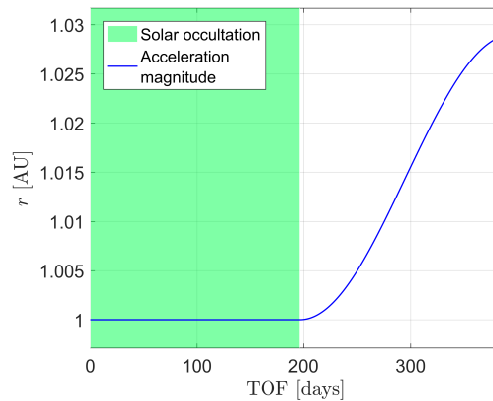


Figure 5.14: Orbital radius as a function of time.

### 5.4.3. EXTREMELY HIGH LASER FLUX IMPINGING

The third case in which the LG is powered-off is when the LS is relatively close to the sailcraft, so that the flux arriving at the sail gets greater than a certain threshold. As already mentioned in Section 5.1, this threshold has been put equal to the solar flux provided at  $r_{min} = 0.2$  AU, i.e.  $25S_0$ , and therefore the following relation holds:

$$S(r) + L(s) \leq S(r_{min}) = 25S_0 \quad (5.15)$$

where  $S(r)$  and  $L(s)$  are respectively given by:

$$S(r) = S_0 \left( \frac{r_0}{r} \right)^2 \quad (5.16)$$

$$L(s) = \frac{W_L}{2\pi [1 - \cos(\theta/2)] s^2} = \frac{W_L}{4\pi \sin^2(\theta/4) s^2} \quad (5.17)$$

In order to express  $L(s)$  in a similar fashion to Equation 5.16, the above formula for the laser flux can also be rewritten as:

$$L(s) = L_0 \left( \frac{r_0}{s} \right)^2 \quad \text{with} \quad L_0 = \frac{W_L}{4\pi \sin^2(\theta/4) r_0^2} \quad (5.18)$$

where, similar to  $S_0$ ,  $L_0$  is the already mentioned laser constant, i.e. the laser flux provided at a laser distance of 1 AU.

By using Equations 5.16 and 5.18, the inequality given in Equation 5.15 can be rearranged to define the range of laser distances in which the LG shall be activated, i.e.:

$$s \geq s_{min} = s_{min}|_{\infty} \cdot \Gamma \quad \text{with} \quad \begin{cases} s_{min}|_{\infty} = r_{min} \sqrt{L_0/S_0} \\ \Gamma = \left( 1 - \frac{r_{min}^2}{r^2} \right)^{-1/2} \end{cases} \quad (5.19)$$

In the above equation the minimum allowed laser distance  $s_{min}$  is expressed by means of a constant part  $s_{min}|_{\infty}$ , representing the  $s_{min}$  achieved if only the laser flux and no solar flux were considered, and a second part  $\Gamma$  which solely expresses the effect of the solar flux. An exemplary graph showing  $s_{min}$  as a function of the orbital distance  $r_0$  for different values of  $L_0$  is provided in Figure 5.15 (assuming  $r_{min} = 0.2$  AU). As can be seen the flux-limited laser distance highly increases only for values of the orbital radius approaching  $r_{min}$ , meaning that the solar flux is already relatively high and thus the LS shall be placed far enough from the sailcraft to prevent surpassing the limit flux of  $25S_0$ . On the other hand, for increasing  $r$  values,  $s_{min}$  asymptotically tends to  $s_{min}|_{\infty}$ , i.e. the minimum laser distance achieved when no solar flux is considered.

In order to validate the correct implementation of the above LG activation criteria, the following simulation has been setup. Once again the sailcraft and LS specifics given at the beginning of this section have been used. The solar sail and LS have been placed in a circular orbit with radius  $r = r_{sc} = r_{ls} = 5$  AU, ideally sharing the same position at departure, but heading to different directions (the LS moves clockwise while the sailcraft counter-clockwise), as shown in Figure 5.16. The sail is oriented parallel with respect to the Sun line (i.e. with  $\alpha = 90$  deg), so that no SRP acceleration is provided. Taking advantage of Equation 5.19, the minimum flux-limited laser distance  $s_{min}$  allowed is found to be 0.141535 AU. Because of the particular orientation of the sail,

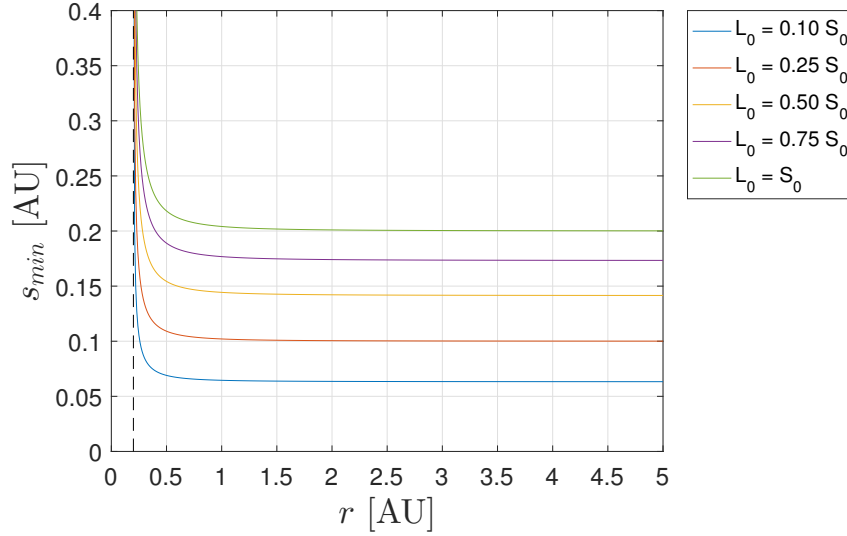


Figure 5.15: Flux-limited minimum laser distance as a function of the heliocentric distance.

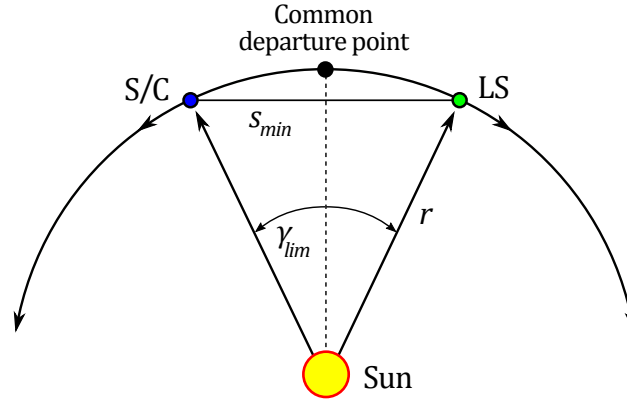


Figure 5.16: Geometry of the scenario considered for validating the powering-off due to extremely high laser flux impinging.

no SRP acceleration is provided and therefore both the sailcraft and LS have the same mean motion  $n$ , as expressed in Equation 5.11b. Therefore, due to the opposite travel directions, the relative mean motion  $n_{rel}$  of the solar sail and LS is given by  $2n$ , i.e.  $2.040635 \text{ degs}^{-1}$ . Given such values of  $s_{min}$  and  $n_{rel}$ , the time between departure and activation of the LG can be computed based on the Sun-LS-sailcraft geometrical configuration. In fact if one takes into account the geometry shown in Figure 5.16 and defines  $\gamma_{lim}$  as the angular distance between LS and sailcraft for which the LG is powered on, the following relations hold:

$$s_{min} = 2r \tan\left(\frac{\gamma_{lim}}{2}\right) \implies \gamma_{lim} = 2 \operatorname{atan}\left(\frac{s_{min}}{2r}\right) \quad (5.20)$$

which yields  $\gamma_{lim} = 1.621759 \text{ deg}$ . Hence, the time to pass before the LG is activated is  $\Delta t = \gamma_{lim} / n_{rel} = 9.198294 \text{ days}$ .

The above scenario has been simulated by numerically integrating the sailcraft EoM, yielding the results shown in Figures 5.17 to 5.20. As expected, Figures 5.17

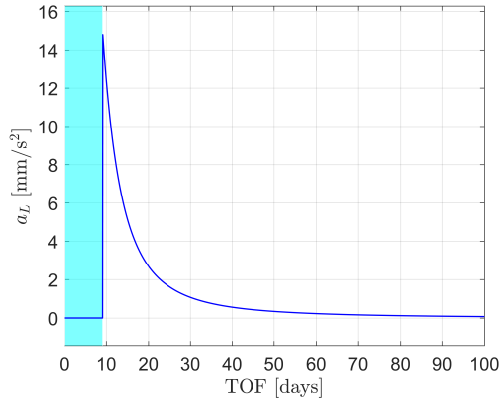


Figure 5.17: LRP acceleration with as a function of time.

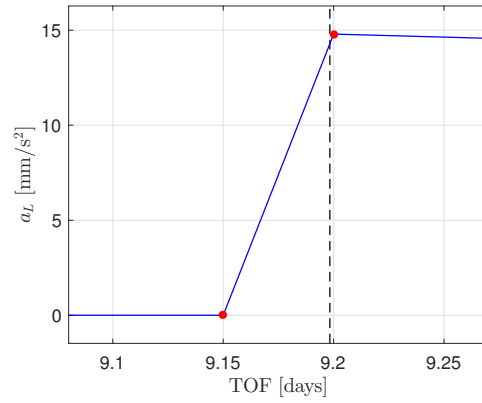


Figure 5.18: LRP acceleration discontinuity due to the LG activation.

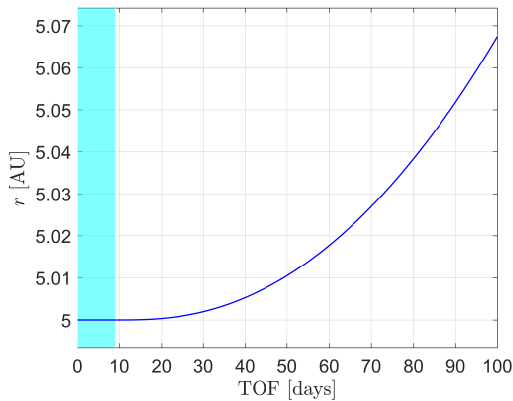


Figure 5.19: Orbital radius as a function of time.

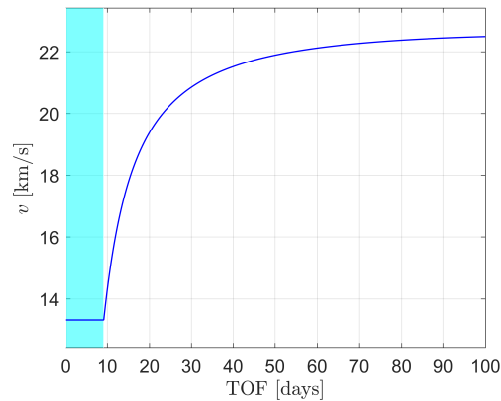


Figure 5.20: Orbital speed as a function of time.

and 5.18 show that the LG is activated within the time step that goes from  $t = 9.15$  days to  $t = 9.20$  days. This time range comprises also the analytical solution  $\Delta t = 9.198294$  days and thus such a numerical results validates the correct implementation of the LG flux-limited deactivation within SCLib. Eventually it can be noted that the sudden LG activation at a laser distance as small as 0.141535 AU yields a high increase in  $a_L$  which affects both the orbital radius and speed, as given in Figures 5.19 and 5.20.

## 5.5. VALIDATION OF LASER-ENHANCED SOLAR SAILING OPTIMIZATION

Once having implemented all laser-enhanced solar sailing functionalities within SCLib, the implementation of these within the InTrance C++ project has been carried out and validated. In order to do so, InTrance has been used to optimize solar sailing and laser-enhanced solar sailing trajectories, with a view to comparing them in a similar fashion to the validation presented in Subsection 5.2.2.

The mission to optimize was chosen to be an orbit rendezvous to Mercury with departure at Earth, meaning that the sailcraft is only required to insert the orbit of Mercury without actually having to rendezvous the celestial body itself. For this type of mission, InTrance allows to set tolerances on the sailcraft final position and velocity, based

on the ones theoretically required to perform the orbit insertion. If the sailcraft were to actually perform a Mercury rendezvous, a final distance from the body smaller than  $R_{SOI,\text{☿}} = 1.1 \cdot 10^5$  km (i.e. Mercury's SOI radius [Wakker, 2015, p.115]) would be required. Based on this value, it was chosen to set a maximum distance from Mercury's orbit of  $10^5$  km. In turn, given this distance constraint, it was also decided to set a final velocity difference of  $470 \text{ ms}^{-1}$ , as this is roughly equal to Mercury's circular velocity  $v_{circ,\text{☿}}$  at a planetocentric distance of  $10^5$  km, i.e.:

$$v_{circ,\text{☿}} = \sqrt{\frac{\mu_{\text{☿}}}{r}} = \sqrt{\frac{2.2032 \cdot 10^{13} \text{ m}^3\text{s}^{-2}}{10^8 \text{ m}}} \approx 469.4 \text{ ms}^{-1} \quad (5.21)$$

where  $r$  represents the above-mentioned planetocentric distance and  $\mu_{\text{☿}} = 2.2032 \cdot 10^{13} \text{ m}^3\text{s}^{-2}$  is Mercury's gravitational parameter [NASA, 2017a].

The traditional and laser-enhanced solar sails considered for this mission have characteristic accelerations respectively equal to  $1.0 \text{ mm s}^{-1}$  and  $0.5 \text{ mm s}^{-1}$ , while both have a diameter of 150 m. The LS is placed at the center of the  $\mathcal{S}$ -frame, with a laser constant  $L_0$  equal to  $S_0$  and a laser beam divergence of  $10^{-8}$  rad, so that the critical laser distance is  $\tilde{s} = 0.10027$  AU. Moreover, for this test case the LG powering-off due to solar occultations has not been used.

Having a traditional solar sail with characteristic acceleration being twice the laser-enhanced one means that, if only the solar radiation were considered, the former would experience an acceleration twice as big as the latter. On the other hand, however, the radiation flux actually impinging the laser-enhanced sail is also given by the LS, and therefore the total flux in this case is twice the one provided to the traditional sailcraft. Hence the use of the above simulation parameters allows to have a traditional and laser-enhanced sailcraft having the same performance. In turn this means that the traditional and laser-enhanced optimal trajectories shall be theoretically equal for the above-described mission. Therefore, based on this reasoning, the validation was carried out in order to assess whether such an expectation was met or not.

Since each optimization run of InTrance is initialized by means of randomly generated chromosome populations, different runs can provide different near-global optimum trajectories. As a consequence, the optimizer was used to perform a total of 10 traditional solar sailing and 10 laser-enhanced solar sailing trajectory optimizations, with a view to actually finding the best trajectories in both cases. Moreover, as InTrance automatically finds the initial conditions that yield the optimal trajectories, a time span of 1 year was set for the departure date, in order to consider all possible positions along the Earth orbit as departure points.

Table 5.2 shows the results of the optimization runs in terms of flight times, their mean

Table 5.2: Flight time-optimal trajectories found for the validation of the laser-enhanced solar sailing implementation in InTrance.

Simulation Number	1	2	3	4	5	6	7	8	9	10	Mean	Std.
Traditional solar sail TOF [days]	308	319	305	291	303	294	<b>289</b>	306	<b>289</b>	294	299.8	9.94
Laser-enhanced solar sail TOF [days]	291	300	304	325	292	314	315	<b>289</b>	295	307	303.1	12.02

and standard deviation. As can be seen all flight times are limited within the range 291 – 325 days, with the laser-enhanced trajectories having a slightly higher mean and standard deviation as compared to the traditional solar sail ones. In spite of this, however, for both traditional and laser enhanced sailcraft the best trajectories have a TOF of 289 days. In order to analyze such results more in-depth, the best five trajectories of each propulsion system have been plotted, as given in Figures 5.21 and 5.22.

As shown in these graphs, all transfer trajectory departure points are relatively close to each other and, not by chance, all sailcraft rendezvous the target orbit close to its pericenter region, where the orbital radius and speed required are respectively the highest and the lowest. All trajectories are confined in a specific region of space and, for both

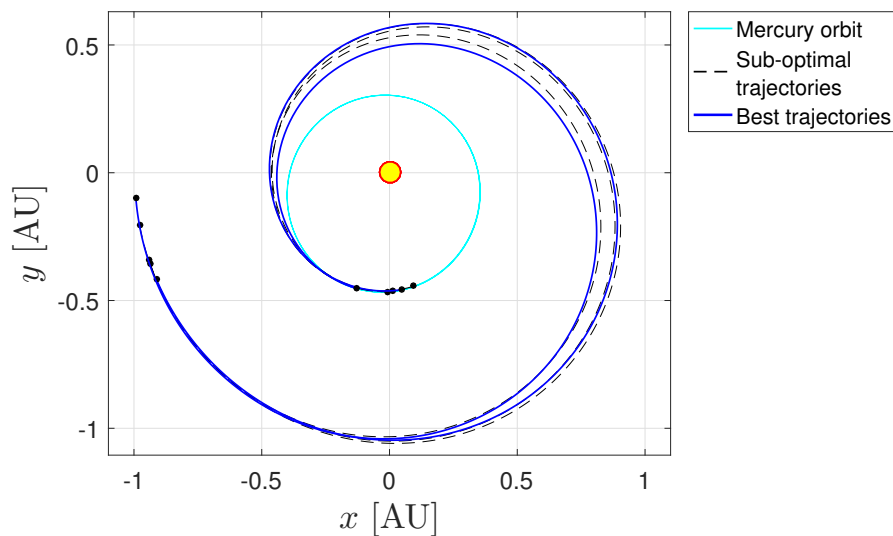


Figure 5.21: Traditional solar sail trajectories found for the Mercury orbit rendezvous scenario used to validate the laser-enhanced solar sailing implementation into InTrance.

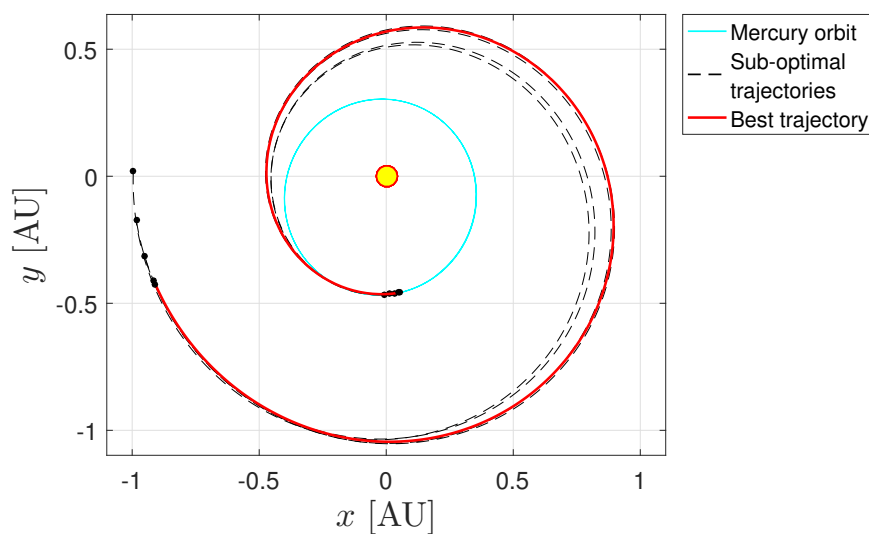


Figure 5.22: Laser-enhanced solar sail trajectories found for the Mercury orbit rendezvous scenario used to validate the laser-enhanced solar sailing implementation into InTrance.

traditional and laser-enhanced sails, two slightly different sub-optimal types of trajectory are found: the ones with a higher or smaller average orbital radius. These can be clearly distinguished in Figure 5.21, where the two best trajectories (in blue) are relatively distant from each other. The same holds also for Figure 5.21, even though in this case only one 289 day-TOF trajectory was found.

All best trajectories found for either propulsion system have TOFs within the range 289 – 295 days. Such a result, together with the similarities in the flight time means, flight time standard deviations and trajectories shapes, allows to conclude that the expectations discussed in the beginning of this section have been met, hence validating the laser-enhanced solar sailing optimization procedure.



# 6

## SIMULATION SETUP AND PARAMETER TUNING

The current chapter provides all information regarding the simulation parameters used and the main design choice taken to setup the simulations. In particular, firstly the choices of the mission scenarios, LS positions, sailcraft and LS parameters to consider will be discussed, while successively the tuning of the integrators used and ENC parameters will be presented.

### 6.1. SIMULATION SCENARIOS

Since laser-enhanced solar sailing has never been used in practice nor analyzed in-depth, the main aim of this work is to provide a first-order analysis of such a propulsion system performance. As a consequence, in order to assess its potential in the most thorough way as possible, three very different mission scenarios have been considered: an orbit rendezvous mission to Mercury, an orbit rendezvous mission to Mars and a flyby to Neptune.

As already mentioned in Section 5.5, performing an orbit rendezvous simply translates into inserting the sailcraft in a target orbit. The main advantage of performing such a maneuver instead of an actual planet rendezvous is that there is no real constraint on the terminal position of the sailcraft along the target orbit. In this way the optimal trajectory retrieved represents an absolute lower bound valid only for the best possible Earth-target body constellation.

The three case studies chosen differ from one another mainly for the type of orbits they involve. In fact, while a solar sailing mission to Mercury requires an inward spiral trajectory which yields a gradual increase in the SRP magnitude, the opposite takes place for transfer trajectories to the Mars orbit, as the sailcraft gets further away from the Sun. Therefore, such mission scenarios were chosen to analyze how the additional LRP affects the transfers' flight time both in the case a relatively high or low SRP is already available.

As for the Neptune flyby, such a mission was chosen to be analyzed with a view to assessing the advantages given by laser-enhanced solar sailing in missions to distant

targets, such as planets in the outer Solar System indeed.

All three mission scenarios assume that the sailcraft depart from Earth, while already inserted in an interplanetary trajectory with a zero hyperbolic excess energy (meaning that the initial velocity as seen from the  $\mathcal{S}$ -frame is the same as the Earth). On the other hand the sailcraft terminal state is determined both by the type of mission considered (orbit rendezvous or flyby) and by the user-defined maximum relative distance  $\Delta r_{max}$  and velocity  $\Delta v_{max}$  computed with respect to the target state/planet. As an example, for the mission to Neptune a  $\Delta r_{max}$  has been set of  $= 10^6$  km, meaning that the flyby is considered successful if the S/C flies at least at a distance of  $10^6$  km from the planet. Although  $10^6$  km is a large distance to actually perform a flyby, this  $\Delta r_{max}$  value was chosen because an accurate enough estimate of the real flyby flight-time is provided nonetheless, as the total travel distance is many orders of magnitude greater than  $\Delta r_{max}$ . Moreover, by performing preliminary simulations, it was found that the use of a smaller  $\Delta r_{max}$  significantly increases the required computational time, which is already non-trivial for trajectory optimizations to the outer Solar System.

On the other hand, the way  $\Delta r_{max}$  and  $\Delta v_{max}$  have been chosen for the orbit rendezvous missions to Mercury and Mars follows the same reasoning described in Section 5.5 based on the dimensions of these planets' spheres of influence. Since the radius of the Martian SOI is  $R_{SOI,\oplus} = 5.8 \cdot 10^5$  km [Wakker, 2015, p.115],  $\Delta r_{max}$  was set equal to  $5.5 \cdot 10^5$  km. On the other hand, since the Mars-centric circular and escape velocities at such a distance are respectively  $279 \text{ ms}^{-1}$  and  $395 \text{ ms}^{-1}$ , the  $\Delta v_{max}$  was set to  $300 \text{ ms}^{-1}$ , so that if the sailcraft were to actually rendezvous the planet, it would be able to orbit about it. In a similar fashion,  $\Delta r_{max} = 10^5$  km and  $\Delta v_{max} = 500 \text{ ms}^{-1}$  were set for the Mercury orbit rendezvous since the planet's SOI radius is  $R_{SOI,\text{☿}} = 1.1 \cdot 10^5$  km [Wakker, 2015, p.115], while the circular and escape velocities at a distance of  $10^5$  km are roughly  $469 \text{ ms}^{-1}$  and  $664 \text{ ms}^{-1}$ , respectively.

For the sake of clarity, Table 6.1 provides all  $\Delta r_{max}$  and  $\Delta v_{max}$  values used for the study cases analyzed.

Table 6.1: Flight time-optimal trajectories found for the validation of the laser-enhanced solar sailing implementation into InTrance.

Mission Scenario	Mercury orbit rendezvous	Mars orbit rendezvous	Neptune flyby
$\Delta r_{max}$ [km]	$1.0 \cdot 10^5$	$5.5 \cdot 10^5$	$1.0 \cdot 10^6$
$\Delta v_{max}$ [ $\text{ms}^{-1}$ ]	500	300	–

Even though for the Neptune flyby optimizations no  $\Delta v_{max}$  had to be set, the specification of another parameter has been required, i.e. the minimum solar distance  $r_{min}$  at which the sailcraft is allowed to orbit. This parameter can highly affect the TOF achieved because, for missions to the outer Solar System, sailcraft usually perform solar photonic assists (SPAs) and the orbital energy acquired in this way is dependent on  $r_{min}$ , indeed. In particular, for the Neptune flyby missions analyzed within this report such a minimum solar distance has been set to 0.3 AU, both for traditional and laser-enhanced sailcraft.

## 6.2. LASER SOURCE AND SAILCRAFT PARAMETERS

Apart from the characteristic acceleration, what strongly influences the amount of thrust induced by a laser beam on a sail is the laser flux provided to the sail itself which, in turn, can be measured by means of the laser constant  $L_0$ . In particular, when Equations 3.34 and 3.21 are used to express  $W_L$  and  $\theta$ ,  $L_0$  can be approximated for small divergence angles as:

$$L_0 = \frac{W_L}{4\pi \sin^2(\theta/4) r_0^2} \approx \frac{0.84 \eta_{wp} W_{LG}^{in}}{(\pi/4) \theta^2 r_0^2} = \frac{4 \cdot 0.84}{\pi \cdot 2.44^2 r_0^2} \cdot \frac{D^2 \eta_{wp} W_{LG}^{in}}{\lambda^2} \quad (6.1)$$

The above formula makes clear the dependency of laser-enhanced sailcraft performance on all LS parameters. In particular, the latter have been chosen based on different considerations, as discussed hereafter.

### WALL-PLUG EFFICIENCY

The wall-plug efficiency of an LG strictly depends on the type of laser generation system it adopts. The current state-of-the-art knowledge in the design and development of diode-pumped laser systems allows to reach a maximum efficiency in the order of 30%, where this value is expected to increase in the future [RP Photonics Encyclopedia, 2017]. On the other hand, high-power free electron laser systems and high-power fiber laser systems can also attain maximum  $\eta_{wp}$  values respectively in the order of 25 and 50% [Sprangle et al., 2009, pp.9-10][RP Photonics Encyclopedia, 2017].

Even though no high-power LG has ever been used to propel sailcraft at interplanetary distances and a detailed analysis of its design is out of scope of this work, based on the above values it was chosen to adopt a wall-plug efficiency value of 0.40 for all simulations. Indeed, based on the current state-of-the-art technology discussed above, such a value might be realistic especially with regard to future missions.

### LASER GENERATOR INPUT POWER

In order to provide a considerable amount of LRP, high-power generation systems are required on-board the LS. In particular, among all possible ones it was decided to focus the attention on nuclear thermal reactors, as these can provide more power compared to solar arrays. As an example the nuclear reactors of the PHOEBUS family (designed and ground-tested for NASA's ROVER nuclear rocket engine program in the 1960s) were capable of providing power levels even in the order of 5 GW which, if used for powering an LG, might generate high-power laser beams [Finseth, 1991, pp.11,70,144]. A sketch representing these nuclear reactors to scale is given in Figure 6.1 [Finseth, 1991, p.79]. As given in [Honorio et al., 2003, p.9], nuclear reactors available nowadays are able to convert the heat released by Uranium-235 ( $U_{235}$ ) fission into electrical energy with an efficiency of only 33 – 36%. Nonetheless, this allows to obtain a constant electrical power of 1 GW for an entire day requiring approximately 3.2 kg of  $U_{235}$ . Therefore, if for instance one considers an electrical power output of 3 GW (i.e. in the same order of magnitude as the PHOEBUS reactors) and a total LG active time of 500 days (which is a value comparable with the TOF of orbit rendezvous missions to Mercury or Mars), a first-order estimate of the total mass of  $U_{235}$  required is  $3 \cdot (500 \text{ days}) \cdot (3.2 \text{ kg day}^{-1}) \approx 4800 \text{ kg}$ . Such an amount of  $U_{235}$  is considerable and its launch into space challenging due to the high risk related to possible launcher failures and scattering of radioactive debris. However, except for this issue, the dispatch of tons of material is something

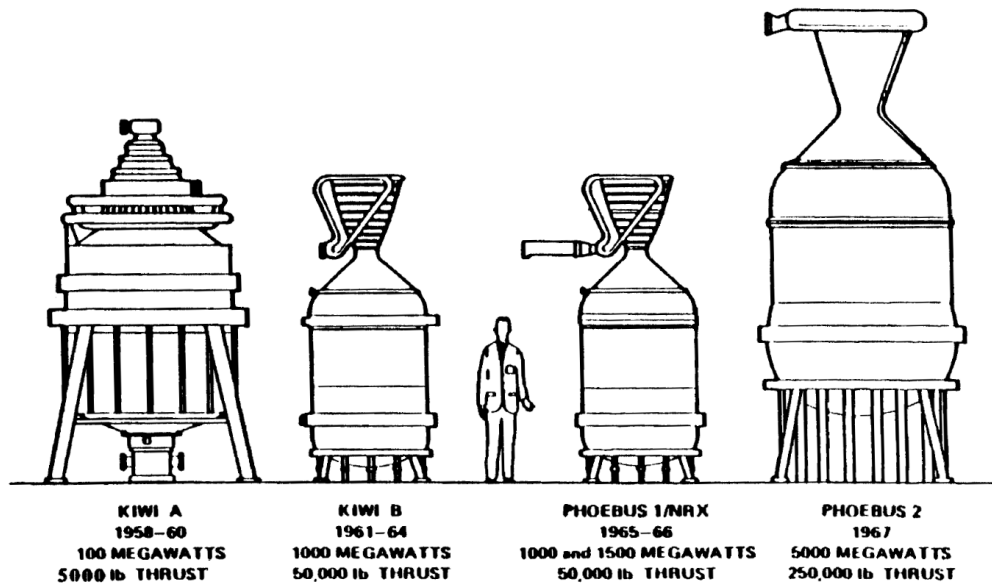


Figure 6.1: Relative size of KIWI and PHOEBUS reactors of NASA's ROVER nuclear rocket engine program [Finseth, 1991, p.79].

feasible using currently available launchers.

As a consequence the above-mentioned value of 3 GW was chosen as  $W_{LG}^{in}$  to be used for the simulations, since it may represent a realistic value for future laser-enhanced sailcraft missions.

#### LASER WAVELENGTH AND LENS DIAMETER

Since from Equation 6.1 it results that  $L_0 \propto (D/\lambda)^2$ , in order to obtain a relatively high laser flux an ultraviolet (UV) laser radiation with a wavelength of 200 nm has been adopted, collimated by means of a 12.5 m-diameter lens. Exploiting such a high-frequency laser requires the usage of proper sail film and coating materials. As given in [McInnes, 1999, pp.60-64], Kapton is by far the most used sail film material adopted for solar sailing and has a good UV resistance (unlike Mylar, for instance). On the other hand, coatings made of aluminium are usually exploited for sailcraft because of their high reflectivity in the visible spectrum (in the order of 90%) [McInnes, 1999, p.63]. However, aluminium reflectivity can reach values in the same range also for smaller wavelengths such as 200 nm, as shown in Figure 6.2 taken after [Hennessy et al., 2016, p.5] (in the graph the term "ideal" is used to refer to unoxidized aluminium, while the blue curves and marks are used to indicate different types of oxidized aluminium).

Although the use of smaller and smaller wavelengths yield a considerable increase in the laser flux (as shown in Equation 6.1), it was decided to set  $\lambda = 200$  nm because for even shorter wavelengths the aluminium reflectivity diminishes. On the other hand, a lens diameter of 12.5 m was considered in order to yield a small enough laser divergence and thus provide an exploitable amount of laser radiation to the sail, while not requiring LG or sailcraft dimensions in the order of kilometers. It should be noted that, since  $L_0 \propto (D/\lambda)^2$ , the LG thrusting capabilities depend on the ratio  $D/\lambda$  which, in this case, is equal to  $1.6 \cdot 10^{-8}$ . As a consequence the validity of the results provided in this work holds also for different  $(D, \lambda)$  pairs, as long as their ratio is indeed about  $1.6 \cdot 10^{-8}$ .

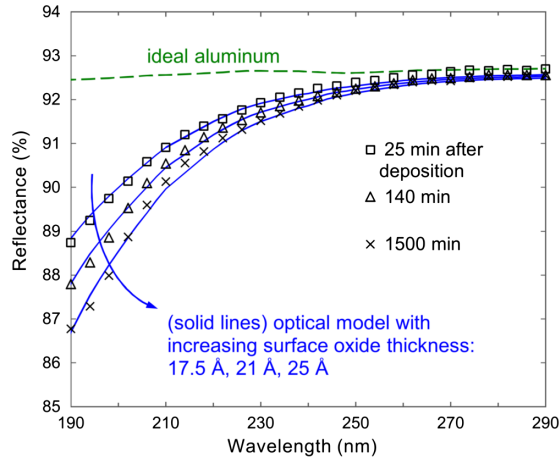


Figure 6.2: Reflectivity of ideal (unoxidized) aluminium and other types of oxidized aluminium [Hennessy et al., 2016, p.5].

### SAILCRAFT CHARACTERISTICS

The specifics of a sailcraft that affect its performance are the characteristic acceleration  $a_c$  and the sail equivalent diameter  $d$ . Based on the state-of-the-art technology related to sailcraft manufacturing as presented in Chapter 2, it was decided to set  $a_c = 0.5 \text{ mm s}^{-2}$  and  $d = 100 \text{ m}$  for the Mars and Mercury orbit rendezvous trajectory optimizations. These values turn out to be realistic for future solar sailing missions if one considers that already in 2013 Sunjammer was manufactured, having a sail loading parameter of  $36 \text{ gm}^{-2}$  (corresponding to  $a_c = 0.254 \text{ mm s}^{-2}$ ) and a surface area of  $1208 \text{ m}^2$  (corresponding to  $d \approx 39 \text{ m}$ ). Besides this, for the Neptune flyby trajectory optimization a more advanced sail with  $a_c = 1.00 \text{ mm s}^{-2}$  has been adopted, once again with  $d = 100 \text{ m}$ . The main reason for this choice is that, unlike the missions to Mercury and Mars, sailcraft missions to the outer Solar System are more probable to take place in a distant future, when the technology readiness level in terms of solar sail manufacturing will be higher (see Figure 2.6 from [Herbeck et al., 2002, p.2] in Section 2.2).

Using the  $\eta_{wp}$ ,  $W_{LG}^{in}$ ,  $\lambda$ ,  $D$  and  $d$  values presented in this section yields a laser constant equal to 2.76% of  $S_0$  and a laser beam divergence angle  $\theta$  of  $3.904 \cdot 10^{-8} \text{ rad} \approx 2.237 \cdot 10^{-6} \text{ deg}$ . Having such a divergence angle does not provide any challenging requirement on the pointing accuracy, since the currently achievable pointing accuracies are indeed in the order of  $10^{-8} \text{ rad}$ , as explained in Section 2.2. On the other hand, however, this value of  $\theta$  yields a small critical laser distance of only 0.017 AU. Consequently, making the sailcraft fly at a small distance from the LS plays a central role if one wants to collect as much laser radiation as possible and thus best exploit the laser power provided. Such a result will be also highlighted by the simulation results, as given in the next chapter.

## 6.3. LASER SOURCE POSITION

As stated in the previous section, having a favorable sailcraft-LS configuration is of fundamental importance to achieve high LRP values. As a consequence the LS positioning represents a crucial aspect of the simulations setup.

To identify the best LS positions many different preliminary optimization runs have been performed. Based on these results and other practical considerations, trade-offs to determine the final best LS orbits to adopt for all mission scenarios have been carried out. Most of the considerations made for choosing such LS positions are similar for all three case studies analyzed. Therefore, for the sake of summary, hereafter only the trade-off process relative to Mercury’s orbit rendezvous is presented. The other two trade-offs related to the missions to Neptune and Mars are instead discussed in Section A.3 of Appendix A.

The LS positioning options discussed and compared are four: LS orbiting in LEO, in a high Earth orbit (HEO) (i.e. an Earth-centered orbit with orbital radius greater than the geostationary one), LS placed in the Sun-Earth  $L_4$  Lagrange point, and in an inner Solar System orbit. The criteria considered in order to trade-off the above options are the  $\Delta V$  budget required for placing the LS in the given orbit, the LS eclipse due to the Earth obstruction, the obstruction due to the presence of other satellites between the LS and sailcraft, the relative Sun-sailcraft-LS geometry, and the suitability of the optimizer in optimizing the given trajectory. In particular the latter criterion has been taken into account because, as explained in Section 5.1, rather than a laser-enhanced solar sailing-specific neural network, an ANN designed for traditional solar sailing has been used. Due to this reason, the LS positioning strongly affects the optimizer robustness and results provided.

The above-mentioned criteria have been used to design a Pugh matrix as can be seen in Table 6.2.

Table 6.2: Pugh matrix used for comparing different LS positioning options for the Mercury orbit rendezvous mission.

Criteria	Weights	LEO	HEO	$L_4$	< 1 AU
$\Delta V$ budget	1	+1	0	0	-1
LS Eclipse	3	-1	+1	+1	+1
Obstruction from other S/C	1	-1	0	+1	+1
Relative geometry	3	+1	+1	-1	0
Optimization	4	-1	-1	+1	+1
	<b>Sum</b>	-4	+2	+5	+7

Among all options presented in the table above, the  $\Delta V$  budget required for placing the LS in LEO results to be by far the smallest one. In fact, in order to fly to HEO or escape Earth from LEO, an additional  $\Delta V$  in the order of  $4 - 5 \text{ km s}^{-1}$  is required [Turner et al., 2011, p.2][Llanos et al., 2012, pp.3-10]. On the other hand, to reach inner Solar System orbits such as the Venus one, the  $\Delta V$  required after having already escaped LEO can even be in the order of  $5 \text{ km s}^{-1}$  [CCAR, 2017].

The relatively close vicinity of Earth represents a real problem only if the LS orbits in LEO, since for all other options the LS is placed relatively far away from the planet.

The same is valid also for the obstruction yielded by other S/C on the laser beam. In this case however, placing the LS in HEO might possibly yield some problems due to the massive presence of satellites in the geostationary Earth orbit (GEO) belt.

Concerning the relative geometry a more in-depth analysis of the options should be carried out. Since the sailcraft departs at Earth already inserted within an interplan-

etary trajectory, having the LS placed in LEO or HEO may come especially useful in the first part of the flight, since the laser distance is relatively small and thus a high LRP thrust is exerted on the sail. Theoretically a similar reasoning holds also for the LS placed in the Sun-Earth  $L_4$  point, since in this case the LS is placed ahead of the sailcraft in the along-track direction for a long time, hence making it possible for the LRP to gradually decelerate the sailcraft. However, in spite of this, by performing preliminary simulations it was found that the LRP acceleration is relatively low due to the high angle  $\alpha_L$  achieved along the trajectory, on average. Therefore, placing the LS in such an orbit yielded a small flight time gain (in the order of maximum 6 days), as will be shown by the results of Tables 6.6 and 6.7. On the other hand, other preliminary simulations showed that placing the LS in an inner Solar System orbit can provide good results in the case a close approach between the sailcraft and LS takes place.

Eventually a last fundamental criterion considered was related to the suitability of the optimizer in actually optimizing trajectories with the LS placed in the given orbits. Having an LS orbiting close to the sailcraft departure position yields problems to the optimizer because of the high LRP acceleration which, however, cannot be optimally exploited. In fact, since such a huge initial acceleration strongly affects the trajectories but cannot be controlled by the neural network (for the reasons explained in Section 5.1), the optimizer results to be totally ineffective in actually optimizing such trajectories. On the other hand, taking advantage of the LS placed in the Sun-Earth  $L_4$  point or in an inner Solar System orbit does not yield such problems, hence making it possible to refine the solutions as explained in Section 5.1, and actually seek for the global optimum.

Given the above considerations valid for the Mercury orbit rendezvous mission, eventually the LS was chosen to be placed in an inner Solar System orbit. Since the sailcraft departs from Earth and has to reach Mercury's orbit, it was decided to place such an LS in the Venus orbit, more specifically in the Sun-Venus  $L_4$  point, as this is a stable Lagrange point.

As discussed in Section A.3 of Appendix A, a similar reasoning has been carried out to determine the best LS position for the Neptune flyby mission. In fact, when dealing with solar sailing missions to the outer Solar System, maneuvers used to direct the sailcraft towards the Sun are usually exploited, in a similar fashion to Mercury orbit rendezvous. Therefore, in this way the possibility of approaching the LS placed in an inner Solar System orbit arises again and, due to this reason, also for this scenario it was indeed decided to place the LS in the Sun-Venus  $L_4$  point. The trajectories defined by exploiting the above-mentioned maneuvers are similar to the one given in Figure 6.3 [Dachwald, 2004, p.82], and their properties will be analyzed more in-depth in the next chapter.

Eventually, concerning the orbit rendezvous mission to Mars, it was chosen to place the LS in the Sun-Earth  $L_5$  point, mainly because of the favorable LS-sailcraft geometry achieved. In fact in this way the LS is placed behind the sailcraft in the along-track direction for a long period of time, hence giving the chance to continuously accelerate the sail.

Even though the LEO and HEO options have been discarded for the missions analyzed in this work, placing the LS in such orbits may actually yield advantages for a variety of missions. In fact, having an LS orbiting about Earth may come in useful to

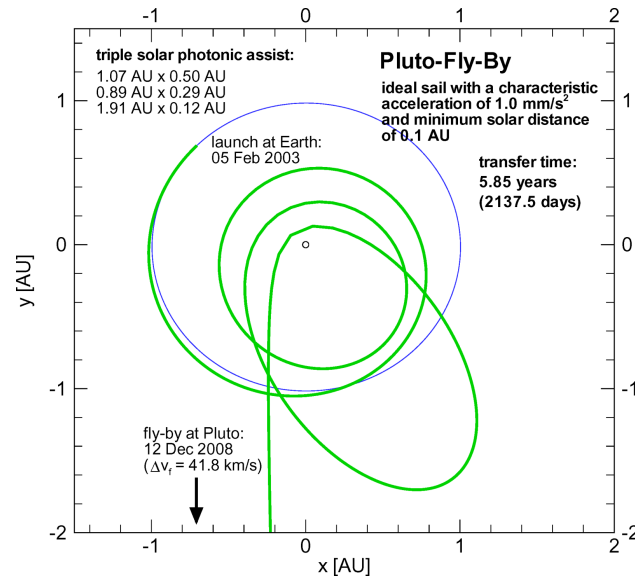


Figure 6.3: Exemplary solar sailing flyby trajectory to Pluto [Dachwald, 2004, p.82].

help sailcraft perform orbit raising, for example. As a consequence, placing an LS in HEO might represent a versatile choice, since in this way the LS could be used to provide thrust both for sailcraft interplanetary trajectories and Earth-centric ones.

## 6.4. INTEGRATOR CHOICE AND TUNING

Since the EoM presented in Subsection 3.8.3 cannot be solved analytically to explicitly retrieve the sailcraft state as a function of time, InTrance takes advantage of numerical integrators to propagate the S/C state. These can be either fixed or variable step-size integrators, which correspond to different accuracies and required computational effort. In particular, the integrators implemented within InTrance are the following:

- RK4: fixed step-size integrator belonging to the Runge-Kutta family. It uses a method of order 4 to perform the step, meaning that such a technique is accurate to the order  $\mathcal{O}(h^4)$  and yields a local truncation error of  $\mathcal{O}(h^5)$  (where  $h$  is the step-size) [Montenbruck and Gill, 2012, p.119].
- RKF54: RK integrator using a step-size control method formulated by Erwin Fehlberg. Here the step is performed using an RK method of order 5 and, afterwards, another RK technique of order 4 is used to estimate the truncation error and adapt the step-size accordingly. In particular, the way the step-size is changed during the integration depends on relative and absolute tolerance values which can be set by the user [Montenbruck and Gill, 2012, p.131].
- RK87DP: integrator belonging to the RK family using a variable step-size technique initially conceived by Dormand & Prince. Here the step computation and error estimation are performed respectively by means of a method of order 8 and 7. As for the RKF54 technique, also in this case relative and absolute tolerances can be set by the user [Montenbruck and Gill, 2012, p.131].

All the above integration techniques are usually exploited in different situations, mainly depending on the required results accuracy. However, in order to choose the best integrators to use for the study cases analyzed in this report, also the integration time has been considered, as this strongly affects the overall optimizations runtime. As a consequence, given these two criteria the integrators to use have been determined through a trade-off.

As already explained in Section 6.1, within this work three missions to Mercury, Mars and Neptune have been studied. In general solar sailing missions to the outer Solar System (like the one to Neptune) require a flight time and a trajectory complexity that is far greater compared to missions to the inner Solar System. This is mainly due to the considerable travel distance and the need of performing SPAs, i.e. solar flybys like the ones shown in Figure 6.3 used to highly increase the solar sail orbital energy. As a consequence, given this preliminary analysis, it was decided to compare the integrators' performances with respect to two different mission scenarios, as presented in the following subsections. Moreover, it should be noted that in both these scenarios laser-enhanced solar sails have been considered rather than traditional ones, simply because their EoM are more complex and thus can be used more efficiently in order to test the integrators.

#### 6.4.1. MISSION TO THE INNER SOLAR SYSTEM

In order to choose which integrator to use for the missions to Mercury and Mars, a relatively simple trajectory spiraling inward the Solar System has been considered. In this way the SRP acceleration exerted gradually increases with time, hence making it easier to highlight the differences in the accuracy of different integrators.

The parameters used for such a simulation are given in Table 6.3, whereas the corresponding trajectory is shown in Figure 6.4.

At departure both the sailcraft and the LS share the same circular trajectory, inclined by 30 deg with respect to the  $XY$ -plane. However the LS is placed ahead in the

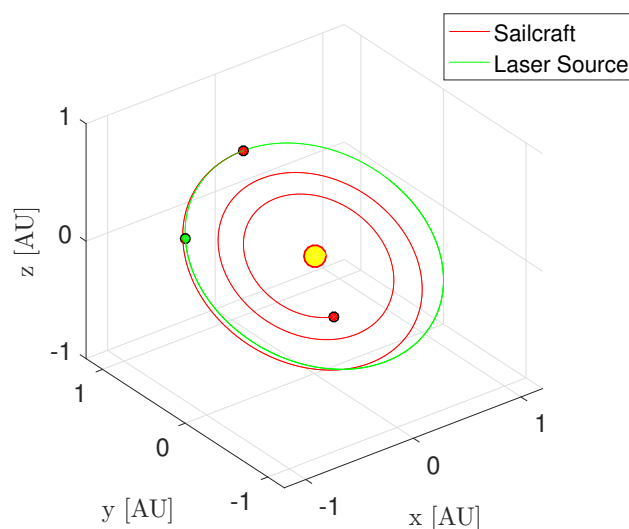


Figure 6.4: Trajectory to the inner Solar System used to test the integrators' performance.

Table 6.3: Simulation parameters of the mission to the inner Solar System used to test the integrators' performance.

Parameter	Symbol	Value
Departure orbit semi-major axis	$a_0$	1 AU
Departure orbit eccentricity	$e_0$	0
Departure orbit inclination	$i_0$	30 deg
LS orbit semi-major axis	$a_{LS}$	1 AU
LS orbit eccentricity	$e_{LS}$	0
LS orbit inclination	$i_{LS}$	30 deg
Initial LS-S/C true anomaly difference	$\Delta\vartheta_0$	60 deg
Pitch angle	$\alpha$	35.26 deg
Clock angle	$\delta$	225 deg
Characteristic acceleration	$a_c$	$0.5 \text{ mm s}^{-1}$
Sailcraft equivalent diameter	$d$	100 m
Laser beam divergence angle	$\theta$	$2.237 \cdot 10^{-6} \text{ deg}$
Critical laser distance	$\bar{s}$	0.017 AU
Laser beam power	$W_L$	$3 \cdot 10^9 \text{ W}$
Laser constant	$L_0$	$0.0276 \cdot S_0$
Total integration time	$\Delta t$	600 days

along-track direction in order to achieve an initial true anomaly difference between the two of 60 deg. In this way the LS can more easily define a braking effect on the solar sail, as it is tilted with a clock angle greater than 180 deg (see Figure 3.8). In particular a clock angle of 225 deg was set in order to make the sailcraft motion non-planar, and a pitch angle of 35.26 deg was chosen as in this way the transversal acceleration component is maximized. Based on the optimal flight times of solar sail transfers to Mercury given in [Dachwald, 2004, p.68], it was decided to set the final integration time to 600 days. Eventually all parameters presented in Section 6.2 were used for the sailcraft and LS characterization.

To test the accuracy of different integrators, the solutions they found were compared with another previously computed reference trajectory. Since no analytical solution of the EoM exists, such a reference trajectory was computed by means of an RK87DP integrator with relative and absolute tolerances set to  $10\epsilon$ , where  $\epsilon = 2.2204 \cdot 10^{-16}$  represents the machine epsilon. Moreover, although variable step-size techniques as the RK87DP automatically compute the optimal step-size to use, in order to compute this reference solution a maximum step-size of 0.5 days has been set as an upper bound, regardless of the fact that such an integrator can then exploit a smaller step-size within the range 0 – 0.5 days if needed. Such a logic has been used also for testing the integrators themselves, which are the RK4, RKF54 and RK87DP, with the latter two having relative and absolute tolerances  $\delta$  set either to  $10^{-8}$ ,  $10^{-10}$  or  $10^{-12}$  (note that hereafter the absolute and relative tolerances will both be indicated as  $\delta$  and simply referred to as "tolerance"). If one considers that during an integration step the sail attitude is fixed, setting a fixed step-size  $h$  (or a maximum step-size  $h_{max}$ ) gives the user freedom to specify how frequently the sail is allowed to change its orientation.

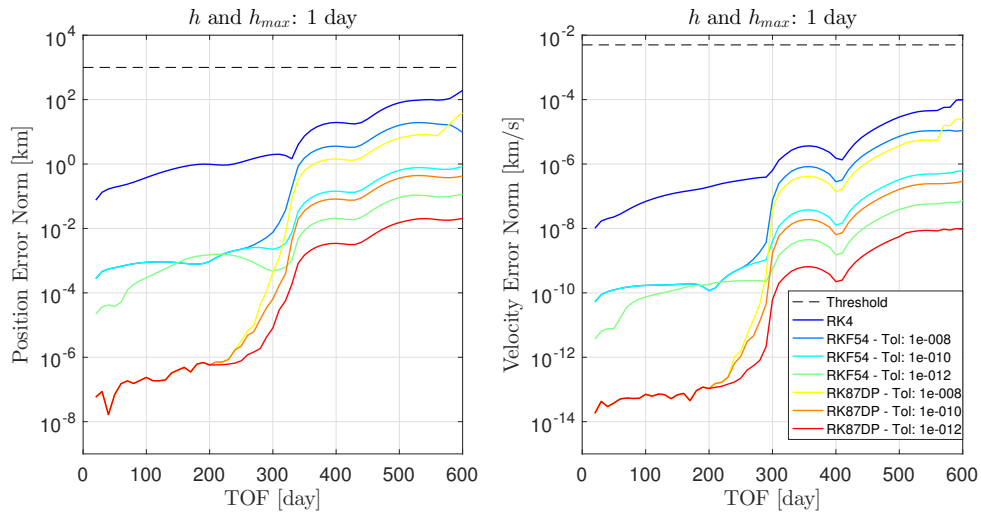


Figure 6.5: Position and velocity errors determined by different integrators for propagating a sailcraft trajectory towards the inner Solar System. Fixed and maximum step-sizes are set to 1 day for all integrators tested, while the reference solution has been computed using an RK87DP integrator with  $\delta = 10\epsilon$  and maximum step-size of 0.5 days.

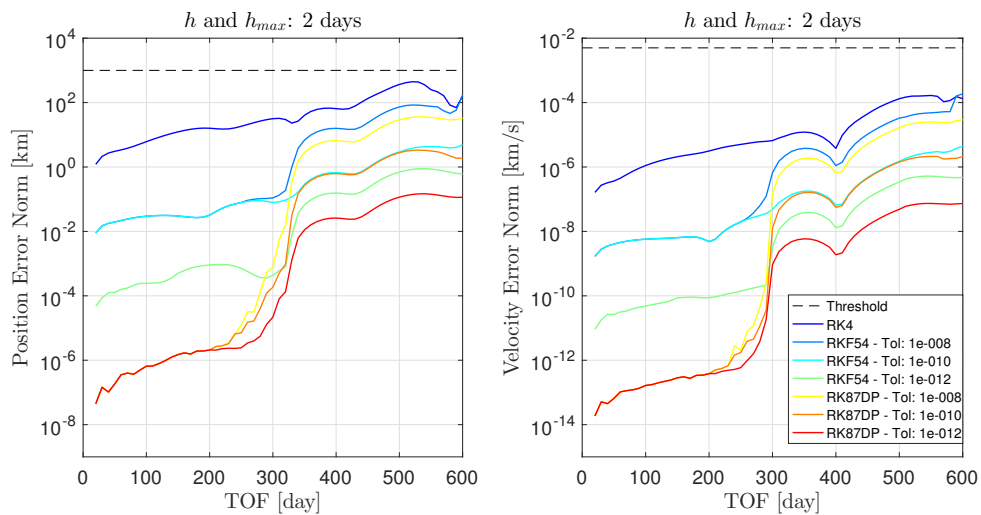


Figure 6.6: Position and velocity errors determined by different integrators for propagating a sailcraft trajectory towards the inner Solar System. Fixed and maximum step-sizes are set to 2 days for all integrators tested, while the reference solution has been computed using an RK87DP integrator with  $\delta = 10\epsilon$  and maximum step-size of 0.5 days.

Since solar sailing missions to Mercury or Mars require flight times in the order of hundreds of days, it was decided to test the integrators by setting  $h$  and  $h_{max}$  equal to 1 and 2 days.

The errors in the position and velocity of the sailcraft resulting from the integration using different techniques are shown in Figures 6.5 and 6.6. In addition, Figure 6.7 shows the computational times required for the integrations, which have been computed by integrating the trajectories 100 times and then averaging the total runtime. In Figures 6.5 and 6.6 also reference threshold values  $\epsilon_{r,ref}$  and  $\epsilon_{v,ref}$  are shown (dashed lines) with respect to which the error curves can be compared. In particular these

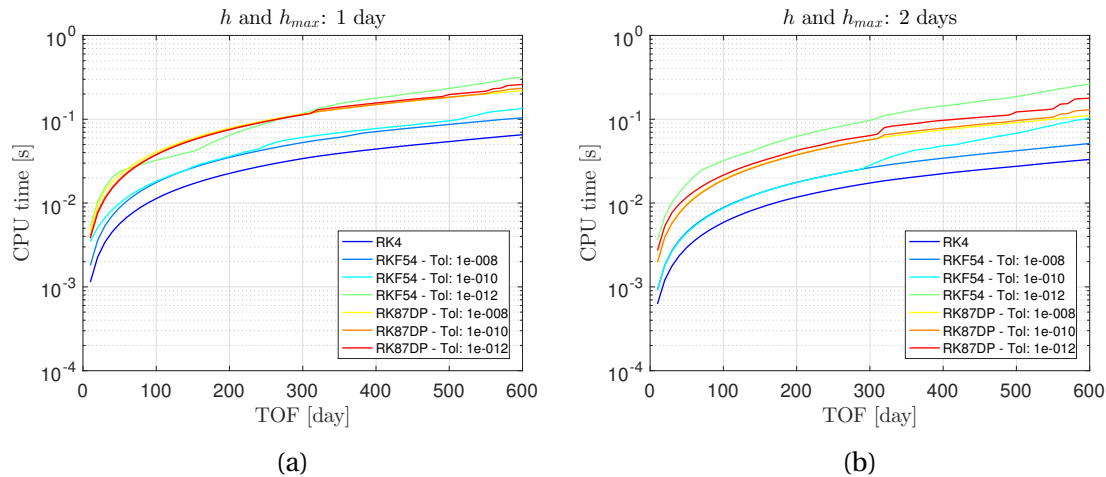


Figure 6.7: Computational time required by different integrators to propagate a sailcraft trajectory towards the inner Solar System with fixed and maximum step-sizes set to 1 day (a) or 2 days (b).

thresholds have been set equal to one hundredth of the maximum relative distance and velocity presented in Section 6.1 for the Mercury study, so that  $\varepsilon_{r,ref} = \Delta r_{max}/100 = 10^3$  km and  $\varepsilon_{v,ref} = \Delta v_{ref}/100 = 5$  ms<sup>-1</sup>. As can be seen, for both step-sizes considered the results achieved are well within such error bounds. Therefore, for the Mercury and Mars scenarios the choice of which integrator to use has been completely driven by the computational time required for the integration. The graphs given in Figures 6.7a and 6.7b clearly show how the RK4 technique is by far the fastest one, as it does not require a double evaluation of the step for controlling the step-size.

Since the RK4 integration using  $h = 2$  days is approximately twice as fast as the RK4 using  $h = 1$  day, in first place it was decided to take advantage of the former option for integrating the laser-enhanced sail trajectories. On the other hand however, in order to provide more accurate results in terms of TOF gain achieved by laser-enhanced solar sailing as compared to traditional solar sailing, it was also decided to perform refinements of the solutions using an RK4 method with a step-size of 1 day. As will be seen in the next section, such refinements have been performed by narrowing the search space around the preliminary optimal solutions found, which in turn has been done by shrinking the time span set for departure. Evaluating the optimal trajectories using a step-size of 2 days for a global scan of the search space and a step-size of 1 day to locally refine the solutions resulted in a considerable amount of computational time saved which, especially for laser-enhanced solar sail trajectory optimization, is usually non-trivial. Instead, with regard to traditional solar sailing trajectory optimization, there was no need for using a step-size of 2 days, since the computational time required in this case is relatively small. Therefore in this case only an RK4 technique with  $h = 1$  day has been used.

In this regard, more details on the computational time required for the traditional and laser-enhanced sailcraft trajectory optimizations will be given in Section 6.5.

#### 6.4.2. MISSION TO THE OUTER SOLAR SYSTEM

In order to choose the most suitable integrator to exploit for the Neptune flyby mission, another test was set up. The main difference with respect to the test case discussed in

Subsection 6.4.1 is that, this time, the simulation parameters have been chosen with a view to making the sailcraft simulate a trajectory similar to the one shown in Figure 6.3, i.e. a trajectory with SPAs. Such simulation parameters are given in Table 6.4. Once again departure orbits inclined by 30 deg have been used for both the LS and the sailcraft, even though in this case the LS one is circular while the (osculating) sailcraft one is elliptic with its pericenter corresponding to the sailcraft initial position. Having  $e > 0$  with  $\delta = 45$  deg and  $\alpha = 35.26$  deg makes the solar sail accelerate while reaching a minimum heliocentric distance of about 0.40 AU, thus simulating an SPA (as illustrated in Figure 6.8). The LS has been set at an initial angular distance  $\Delta\vartheta_0$  from the sailcraft equal to  $-60$  deg, meaning that the LS is placed behind the sailcraft in the along-track direction and therefore is in a favorable position to accelerate the solar sail. The total integration time has been set to 3660 days (approximately 10 years) in order to simulate the long TOF usually required for sailcraft missions to the outer Solar System (see [Dachwald, 2004, pp.80-83]), whereas the parameters used to characterize the sailcraft and LS specifics are the same already used for the test case discussed in the previous subsection.

Since the flight time required for missions to the outer Solar System are in the order of years, this time larger step-sizes have been considered by posing  $h$  and  $h_{max}$  equal to 5, 10 and 15 days. On the other hand, the reference solution has been computed through an RK87DP integrator with  $\delta = 10\epsilon$  and a step-size of 0.5 days. The integration errors given in Figures 6.9 to 6.11 show a fast increase during the first phase of the flight which is due to the SPA performed. As can be seen the exploitation of a large step-size makes the use of an RK4 integrator inappropriate, as this leads to errors well above

Table 6.4: Simulation parameters of the mission to the outer Solar System used to test the integrators' performance.

Parameter	Symbol	Value
Initial semi-major axis	$a_0$	0.634 AU
Initial eccentricity	$e_0$	0.578
Initial inclination	$i_0$	30 deg
LS orbit semi-major axis	$a_{LS}$	1 AU
LS orbit eccentricity	$e_{LS}$	0
LS orbit inclination	$i_{LS}$	30 deg
Initial LS-S/C true anomaly difference	$\Delta\vartheta_0$	$-60$ deg
Pitch angle	$\alpha$	35.26 deg
Clock angle	$\delta$	45 deg
Characteristic acceleration	$a_c$	$1.0 \text{ mm s}^{-2}$
Sailcraft equivalent diameter	$d$	100 m
Laser beam divergence angle	$\theta$	$2.237 \cdot 10^{-6}$ deg
Critical laser distance	$\bar{s}$	0.017 AU
Laser beam power	$W_L$	$3 \cdot 10^9$ W
Laser constant	$L_0$	$0.0276 \cdot S_0$
Total integration time	$\Delta t$	3660 days

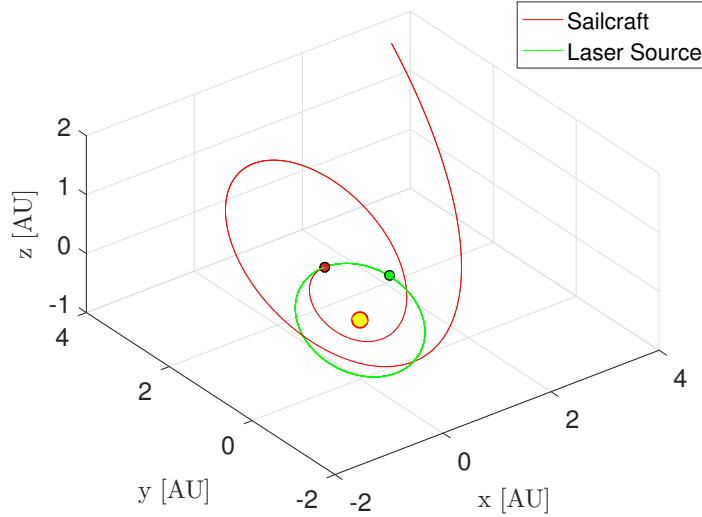


Figure 6.8: Trajectory to the outer Solar System used to test the integrators' performance.

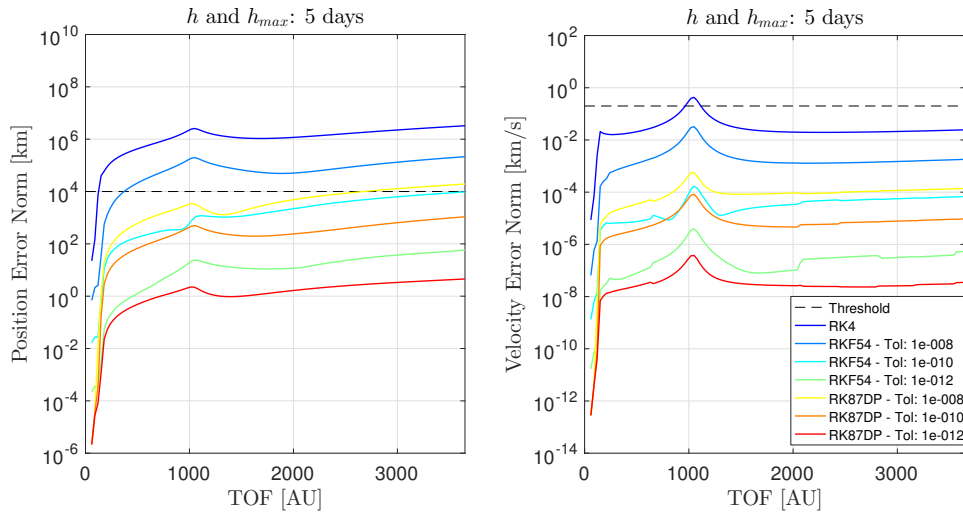


Figure 6.9: Position and velocity errors determined by different integrators for propagating a sailcraft trajectory towards the outer Solar System. Fixed and maximum step-sizes are set to 5 days for all integrators tested, while the reference solution has been computed using an RK87DP integrator with  $\delta = 10e$  and maximum step-size of 0.5 days.

the  $\varepsilon_{r,ref}$  and  $\varepsilon_{v,ref}$  thresholds. In a similar fashion to the test case discussed in the previous subsection, here  $\varepsilon_{r,ref}$  has been chosen based on the  $\Delta r_{max}$  specified in Section 6.1 for the Neptune flyby as  $\varepsilon_{r,ref} = \Delta r_{max}/100 = 10^4$  km. Instead, concerning the threshold on the velocity error, this was put equal to  $200 \text{ ms}^{-1}$  as the velocities achieved after having performed SPAs are usually in the order of  $20 \text{ km s}^{-1}$  or even higher (note the hyperbolic excess velocity given in Figure 6.3). Moving to the RKF54 and RK87DP integrators, it can be noted that the accuracy provided is similar for all  $h_{max}$  values adopted due to the step-size controls which keep the integration errors bounded. The velocity errors defined by the variable step-size integrators are always well within the  $\varepsilon_{v,ref}$  reference value. As for the position errors, the RKF54 integrator with tolerance equal to  $10^{-8}$  yields errors greater than  $\varepsilon_{r,ref}$ , whereas the RKF54 and RK87DP integration techniques, respectively with  $\delta$  set to  $10^{-10}$  and  $10^{-8}$ , yield position errors in the

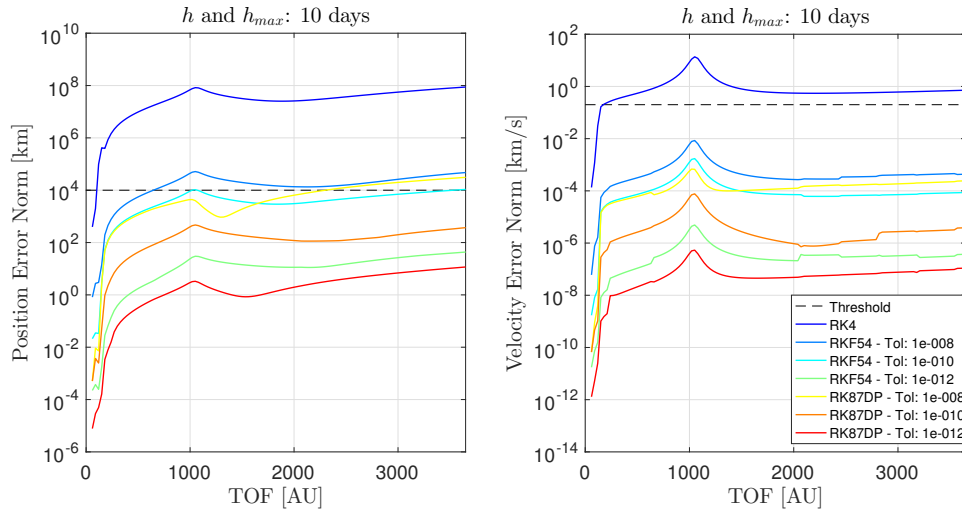


Figure 6.10: Position and velocity errors determined by different integrators for propagating a sailcraft trajectory towards the outer Solar System. Fixed and maximum step-sizes are set to 10 days for all integrators tested, while the reference solution has been computed using an RK87DP integrator with  $\delta = 10\epsilon$  and maximum step-size of 0.5 days.

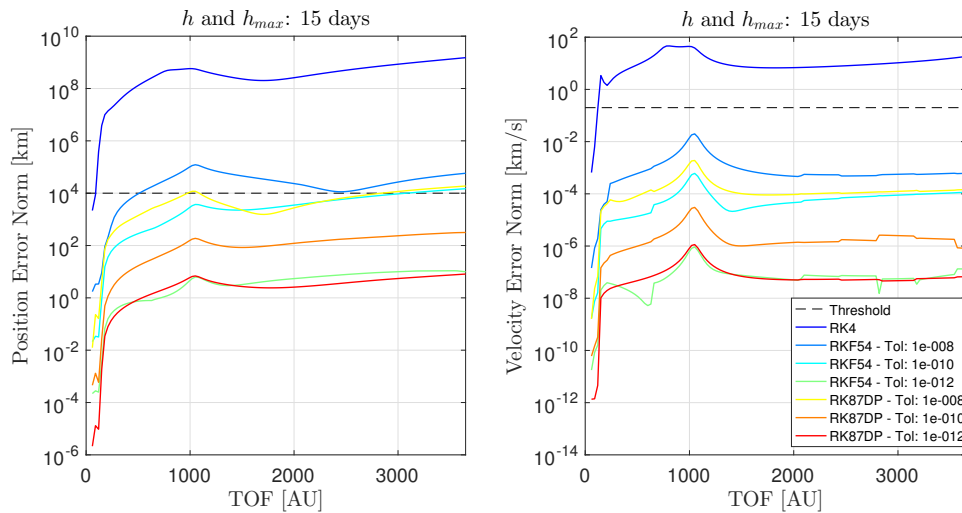


Figure 6.11: Position and velocity errors determined by different integrators for propagating a sailcraft trajectory towards the outer Solar System. Fixed and maximum step-sizes are set to 15 days for all integrators tested, while the reference solution has been computed using an RK87DP integrator with  $\delta = 10\epsilon$  and maximum step-size of 0.5 days.

order of  $\epsilon_{r,ref}$ . All other RKF54 and RK87DP integrators with smaller tolerances yield instead smaller errors as compared to the threshold.

Among the integration techniques that yield errors below the thresholds, the one that requires the least computational time for any  $h_{max}$  considered is RK87DP with  $\delta = 10^{-10}$ . This can be appreciated in the graphs of Figure 6.12, where it is also made clear how the use of a maximum step-size of 15 days defines a computational time gain with respect to the cases in which  $h_{max} = 5$  days or  $h_{max} = 10$  days. On the other hand, among the integrators yielding a position error in the order of  $\epsilon_{r,ref}$ , the one performing best for  $h_{max} = 15$  days is RK87DP with  $\delta = 10^{-8}$ , which requires roughly 1.7 times less computational time than RK87DP with  $\delta = 10^{-10}$  and  $h_{max} = 15$  days.

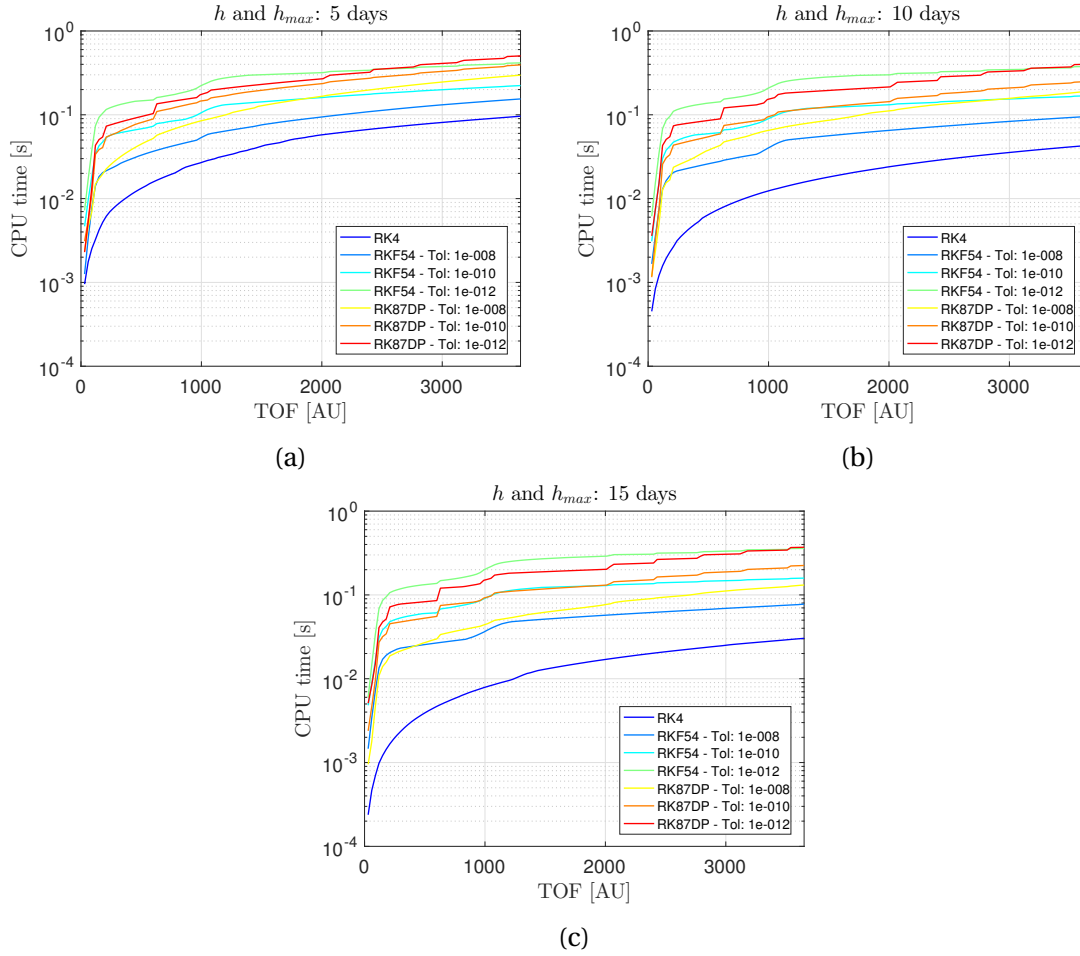


Figure 6.12: Computational time required by different integrators to propagate a sailcraft trajectory towards the outer Solar System with fixed and maximum step-sizes set to 5 days (a), 10 days (b) or 15 days (c).

Since the RK87DP integrator with  $\delta = 10^{-8}$  does not provide errors considerably higher than  $\varepsilon_{r,ref}$  while being much faster than the RK87DP integrator with  $\delta = 10^{-10}$ , in the end it was decided to exploit the former integrator both for the traditional and laser-enhanced solar sailing optimizations of the Neptune flyby trajectory. In a similar fashion to the optimization of the orbit rendezvous trajectories, also in this case it was decided to perform a refinement of the solutions. To this aim, further optimization runs have been carried out, exploiting once again an RK87DP integrator with  $\delta = 10^{-8}$ . By doing so, computational times in the order of 16 – 18 hours have been achieved for the preliminary laser-enhanced sailcraft trajectory optimizations, while runtimes in the order of 6 – 7 hours have been achieved for the refinement optimizations.

For the sake of summary, Table 6.5 shows the integrators used for all three scenarios analyzed. The choice of using two different integrators and three step-sizes depending on the scenario considered has been made mainly because of the high computational time required for laser-enhanced solar sailing optimization. In fact, by exploiting a combination of different step-sizes and refinement runs, an acceptable accuracy has been achieved (as explained in the current and previous sections), while considerably

Table 6.5: Integrators used for optimizing the trajectories of the three scenarios analyzed.

Mission	Sailcraft type	Preliminary optimization	Refinement
Mercury orbit rendezvous	Traditional	RK4, $h = 1$ day	RK4, $h = 1$ day
	Laser-enhanced	RK4, $h = 2$ days	
Mars orbit rendezvous	Traditional	RK4, $h = 1$ day	RK4, $h = 1$ day
	Laser-enhanced	RK4, $h = 2$ days	
Neptune flyby	Traditional	RK87DP, $h_{max} = 15$ days, $\delta = 10^{-8}$	
	Laser-enhanced		

reducing the overall computational time required.

As already mentioned, for all three study cases analyzed preliminary solutions have been firstly found and then their refinement has been performed. To locally narrow the search space around such preliminary optimal solutions, two different methods have been used.

Concerning the missions to Mercury and Mars orbits, the departure date of the best preliminary found trajectory has been considered in order to shrink the departure date time span allowed for the refinement optimizations. This means that for the refinement runs the departure date range has been centered in the preliminary optimal departure date previously found, and its width has been put equal to 4 days.

Such a technique has been used also for the Neptune flyby mission but, due to the higher variability of the results obtained in this case, also a second refinement technique has been adopted. In fact, given the best trajectories found through the departure date shrinking method, the corresponding solution chromosomes have been exploited to perform further optimization runs as initial reference to create the first EA chromosome generations. In this way the ENC has already available a reference solution to work on when the optimization starts, so that the latter actually performs a refinement of the initially provided steering strategy. Moreover, since an initial solution is given indeed, the optimization runs also require less time to perform, which turned out to be in the order of 7 hours, as already mentioned.

By using such refinement techniques an effective narrowing of the search space has been carried out, reducing the overall computational time and allowing to perform local optimizations which have lead to more optimal solutions than the ones found preliminary.

## 6.5. NEURAL NETWORK STRUCTURE AND CHROMOSOME POPULATION SIZE

As explained in Section 4.2, InTrance takes advantage of a feed-forward ANN having a predefined number of output neurons, as well as user-defined numbers of input neu-

rons and hidden neurons (see Figure 4.1).

The input layer used for all simulations is composed of 24 neurons, used to provide the S/C and target states to the ANN expressed both in Cartesian and spherical coordinates, while, on the other hand, the output layer is made up of three neurons in order to specify the sail normal unit vector history  $\hat{n}[t]$ . Only one hidden layer has been used for the optimizations, and since InTrance allows to choose the number of neurons inside of it, preliminary optimization runs have been performed to understand if a correlation exists between the number of hidden neurons and the quality of the results provided. Despite the effort, however, no meaningful result has been achieved, meaning that such preliminary optimization runs showed no correlation between the achieved TOF values and number of neurons used. As a consequence, in the end it has been chosen to exploit 30 hidden neurons, as in this way the same ANN topology exploited for the solar sailing optimizations given in [Dachwald, 2004] has been used. In particular in [Dachwald, 2004, pp.71-73] such an ANN structure showed to be the one giving the best results in terms of TOF for traditional solar sailing.

Before actually performing the optimizations for the three scenarios, also the tuning of the chromosome populations size has been pursued. As explained in Section 4.2, InTrance takes advantage of populations of chromosomes to find the optimal network function and thus the optimal trajectory. For each generation, all chromosomes are evaluated through a fitness function used to select only the most promising ones with a view to generating a new offspring. Consequently, the exploitation of wider populations on one hand helps scanning the search space more in-depth while, on the other hand, it increases the number of fitness evaluations and thus the overall computational time required for the optimization.

In order to determine the optimal population size to use within InTrance, traditional and laser-enhanced sailcraft rendezvous trajectories to Mercury's orbit have been optimized. The LS and sailcraft specifics used are the ones presented in Section 6.2 for the Mercury orbit rendezvous scenario, the integrator used is an RK4 with step-size of 1 day, the departure date time span was set equal to 1 year in order to account for all possible departure positions along the Earth orbit, and the LS was placed in the Sun-Earth  $L_4$  point, so that the laser beam could easily provide a braking effect on the sail. The population sizes chosen for this study have been 25, 50, 75 and 100, and for each of them 5 optimizations were run using both traditional and laser-enhanced sails.

The results of these optimization runs are given in Tables 6.6 and 6.7.

Table 6.6: Tuning of the chromosome population size used for traditional solar sailing trajectory optimization. All simulations have been run using 3 cores of a 3.3 GHz Intel processor. The values in bold represent the overall minimum TOF achieved, the minimum average TOF and the minimum standard deviation.

Pop. size	TOF[days]							Mean CPU time [h]
	Sim.1	Sim.2	Sim.3	Sim.4	Sim.5	Mean	Std.	
25	548	552	547	538	575	552	13.83	0.48
50	550	545	544	550	548	547.4	2.79	0.63
75	546	542	545	544	545	<b>544.4</b>	<b>1.51</b>	1.02
100	547	546	543	561	<b>536</b>	546.6	9.13	1.04

Table 6.7: Tuning of the chromosome population size used for laser-enhanced solar sailing trajectory optimization. All simulations have been run using 3 cores of a 3.3 GHz Intel processor. The values in bold represent the overall minimum TOF achieved, the minimum average TOF and the minimum standard deviation.

Pop. size	TOF[days]							Mean CPU time [h]
	Sim.1	Sim.2	Sim.3	Sim.4	Sim.5	Mean	Std.	
25	549	548	565	544	541	549.4	9.28	1.70
50	539	550	546	540	<b>530</b>	541	7.62	2.28
75	536	538	544	535	536	537.8	<b>3.63</b>	3.43
100	532	531	536	532	541	<b>534.4</b>	4.16	4.16

Although five simulations per population size are few to conduct a statistically reliable analysis, the above tables help in preliminary identifying the best population size to adopt. As can be seen the standard deviations of the flight times achieved with traditional solar sails are smaller than the corresponding standard deviations obtained using laser-enhanced sailcraft. This suggests that InTrance optimizes traditional solar sailing trajectories more easily. Moreover, the average runtime required for traditional solar sailing optimization is approximately 3-4 times smaller than the one required for laser-enhanced solar sailing, since in the latter case a higher number of calculations is required to compute the sailcraft thrust.

As expected, the use of more numerous populations yields better results for both propulsion systems, on average. However this also requires a higher computational effort and time.

With regard to traditional solar sailing, the number of chromosomes yielding the best results is 75, both in terms of mean TOF and standard deviation. However there is confidence that also a population size of 100 elements yields satisfactory results (in this regard it should be noted that the high mean TOF and standard deviation are mostly due to the flight time of 561 days which acts as an outlier). Similarly, also in the laser-enhanced solar sailing case the populations with 75 or 100 chromosomes tend to return better results.

Using 75 chromosomes yields satisfactory results both for traditional and laser-enhanced solar sailing, while requiring a smaller computational time compared to the optimizations performed with 100 chromosomes (especially in the laser-enhanced case). Consequently, in the end it was decided to exploit populations with 75 chromosomes for the optimizations. In this way computational time has been saved, while a satisfactory accuracy of the results has been achieved nonetheless, thanks to the high number of simulations performed and the solution refinements.

Eventually it is interesting to notice the order of magnitude of the TOF gain achieved by using laser-enhanced sailcraft, which is of only 6 days (if one compares the two best traditional and laser-enhanced solar sail trajectories found). As already explained in Section 6.3, based on this result it was eventually chosen not to place the LS in the Sun-Earth  $L_4$  point, but rather in the Sun-Venus  $L_4$  one. As will be seen in the next chapter, such a choice has indeed led to considerably higher TOF gains.



# 7

## RESULTS AND ANALYSIS

### 7.1. MERCURY ORBIT RENDEZVOUS

The traditional and laser-enhanced solar sail trajectories for this type of mission have been optimized using the parameters specified in the previous chapter. However, before actually running the simulations, an analysis concerning the optimal departure date to adopt has been carried out, as explained hereafter.

In order to consider all possible initial angular distances between sailcraft and LS, a departure time span with length equal to a Venus synodic period was adopted, i.e.  $T_{\varphi, syn} = 583.92$  days [NASA, 2017e]. However, given this time span width, different departure date ranges can be chosen. If the LS orbit, target orbit and initial S/C orbit were all circular, such a symmetry would make the specific choice of a certain departure date range unnecessary, as the relative geometry of the problem would be recovered exactly every 583.92 days. However, as Mercury's orbit is slightly eccentric, this is not strictly true for the problem analyzed here. Consequently the need to determine the best departure date time span to adopt in order to achieve the smallest TOF arose. As can be seen in Figures 5.21 and 5.22, the optimal Mercury orbit rendezvous trajectories are achieved when the sailcraft performs the Mercury orbit insertion close to the apocenter region, i.e. where the velocity is the lowest and the sailcraft is the closest to the departure conditions. As a consequence the best departure date time span is the one that allows the LS to provide a significant LRP acceleration, while making the sailcraft head to the above-mentioned target orbit apocenter region.

By means of preliminary simulations and through an analysis of the initial angular distances between LS, sailcraft and Mercury's pericenter, eventually such an optimal time span was found to be [63668 MJD, 64251 MJD] (corresponding to 12 March 2033 - 16 October 2034), where MJD stands for Modified Julian Date.

As explained in Subsection 6.4.1, in order to find the near-global optimum traditional and laser-enhanced solar sailing trajectories for this mission scenario, multiple optimization runs have been performed in order to extensively scan the search space. In particular, concerning traditional solar sailing, firstly 25 preliminary optimizations have been carried out and, based on the best trajectory found, another 10 optimization runs used for refinement have been performed. In this way a trajectory with a TOF of

535 days has been found, having a departure date equal to 63966 MJD, corresponding to 4 January 2034.

Similarly, for the laser-enhanced sailcraft trajectory 50 preliminary simulations and 25 refinement simulations have been performed, yielding an optimal trajectory with TOF and departure date respectively equal to 477 days and 63954 MJD (23 December 2033). Figure 7.1 shows the final optimal traditional and laser-enhanced solar sail trajectories presented above. Since their departure dates differ from one another by only 12 days, the two departure positions are relatively close to each other, thus making it easier to appreciate how the two trajectories evolve differently in time.

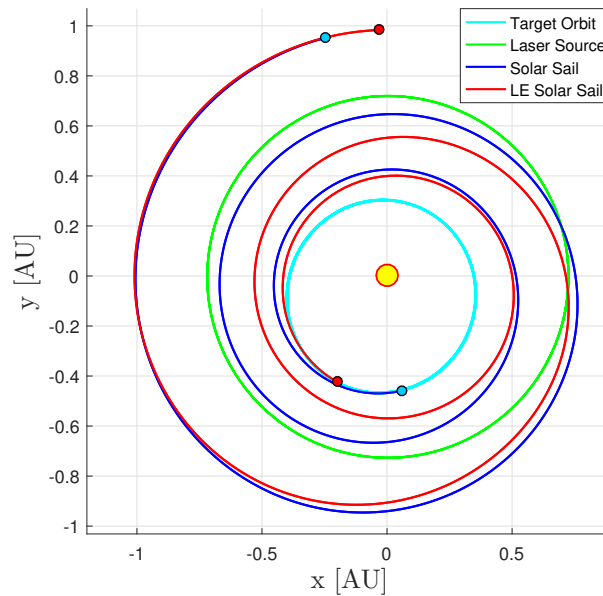


Figure 7.1: Flight time-optimal trajectories to Mercury's orbit using traditional and laser-enhanced solar sails. The blue and red circles represent the initial and final positions of the traditional and laser-enhanced sailcraft, respectively.

As shown in Figure 7.2, the clock angles of both sailcraft vary similarly, always assuming values close to 180 deg. In this way the solar sails continuously decelerate and, moreover, thanks to the oscillations in the range 140–210 deg, they slowly change their orbital inclination so as to make it match Mercury's one at arrival.

As for the pitch angles, also the traditional and laser-enhanced sailcraft angles follow similar trends, as shown in Figure 7.3.  $\alpha$  is in fact bounded in the range 20–60 deg for the entire duration of the flights and, in particular, the traditional solar sail pitch angle always assumes values close to 35.26 deg, i.e. the optimal pitch angle used to maximize the deceleration in the transversal direction. Figure 7.3 also shows the variation in time of the laser pitch angle  $\alpha_L$ . For most of the transfer time such an angle is usually high and in some cases it even gets greater than 85 deg, meaning that the LG is powered off in order not to impinge the sail front-side. The only times in which  $\alpha_L$  assumes relatively small values is within the TOF range 177–277 days and during the terminal phase of the transfer, although in this case a solar occultation prevents the laser radiation from actually impinging the sail. As can be seen in Figure 7.1, during the first part of the flights the two sailcraft follow very similar trajectories, and thus their heliocentric distances (shown in Figure 7.4) result approximately equal. How-

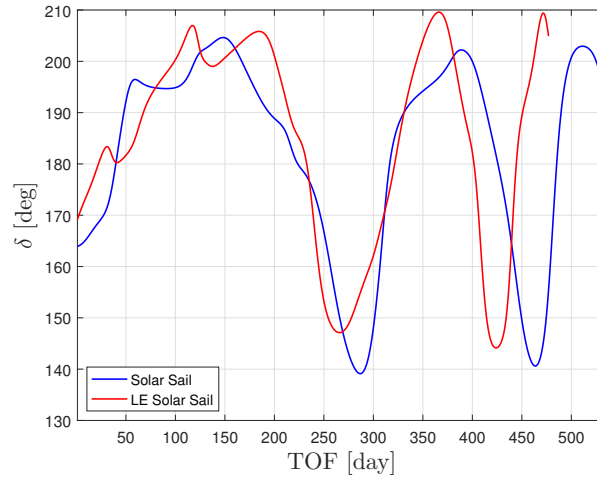


Figure 7.2: Clock angles of the traditional and laser-enhanced solar sails for the Mercury orbit rendezvous mission.

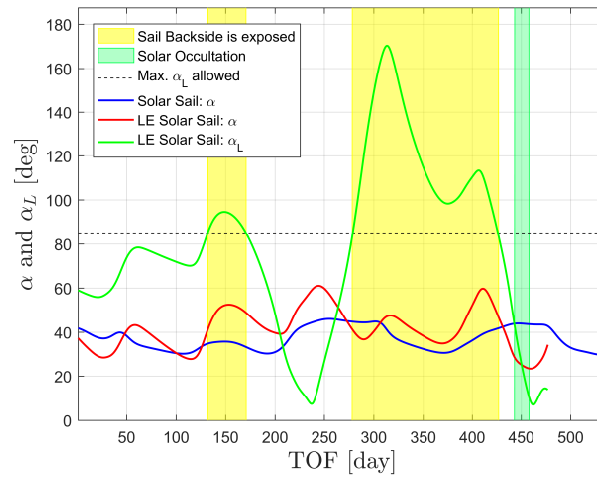


Figure 7.3: Pitch angles of the traditional and laser-enhanced solar sails for the Mercury orbit rendezvous mission.

ever a strong decrease of the laser-enhanced sailcraft orbital radius takes place after 280 days, hence yielding a deviation from the traditional solar sail trajectory right after the intersection with the LS orbit (see Figure 7.1). Such a strong decrease of the orbital radius takes place because of the high LRP thrust exerted by the LS which, in turn, is mainly due to the small laser distance achieved in this flight segment. Since between 177 days and 277 days from departure small  $\alpha_L$  and  $s$  values are achieved simultaneously, the LRP acceleration highly increases, reaching a magnitude roughly twice the SRP acceleration, as can be seen in Figure 7.5. The effects of such a close laser source approach (CLSA) can also be appreciated in Figure 7.6, where the LRP acceleration vectors are plotted along the laser-enhanced sailcraft trajectory. Figure 7.6 also shows how the LS is placed in an unfavorable position with respect to the laser-enhanced sailcraft right after the CLSA. In fact, since the LS orbits at a heliocentric distance equal to  $a_{\oplus}$  (with  $a_{\oplus} = 0.723336$  AU being the Venus semi-major axis [Wakker, 2015, p.673]) while the sailcraft continues to spiral inwards, the latter exposes its back-side to the LS,

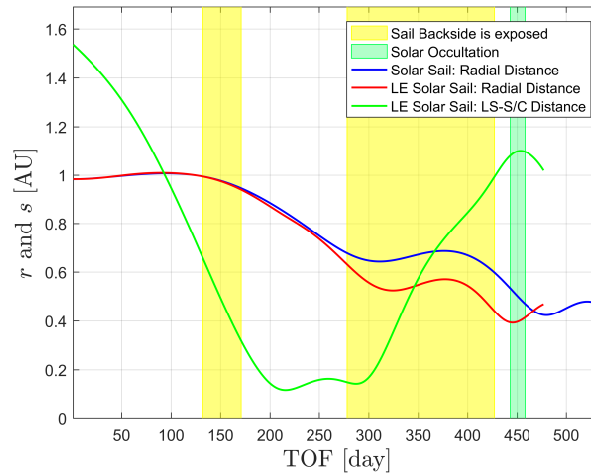


Figure 7.4: Orbital radius and laser distance of the traditional and laser-enhanced solar sails for the Mercury orbit rendezvous mission.

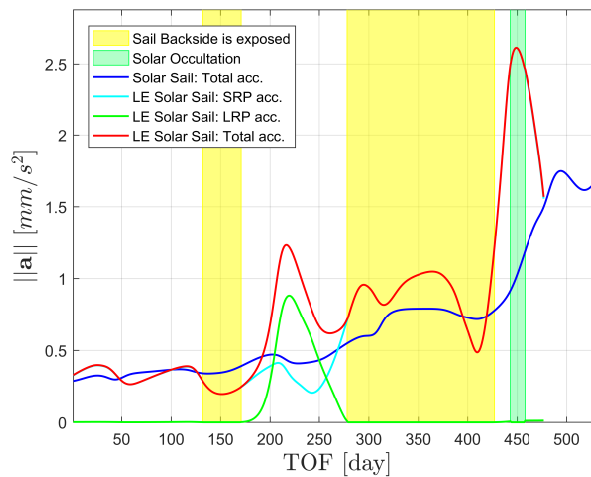


Figure 7.5: Magnitudes of the SRP, LRP and total accelerations experienced by the traditional and laser-enhanced solar sails for the Mercury orbit rendezvous mission.

so that the LG has to be powered off to prevent damaging the sail material. Such a circumstance persists for a relatively long time, approximately between 280 and 430 days from departure, hence making the LS ineffective during this period. After this period the solar sail front-side is exposed again to the LS but, on the other hand, the two are almost diametrically opposed with respect to the Sun, so that a solar occultation takes place. As a consequence also in this final phase of the flight no LRP can actually be provided.

As expected the above-discussed results have shown that, in order to efficiently take advantage of the LRP, close approaches with the LS are required. However, on the other hand, to make these happen very specific LS-sailcraft departure constellations should be exploited. Therefore, for this type of missions the LS orbit and departure date shall be chosen carefully if a CLSA is sought.

Apart from this, such a mission scenario has also shown the inefficiency of the LS when

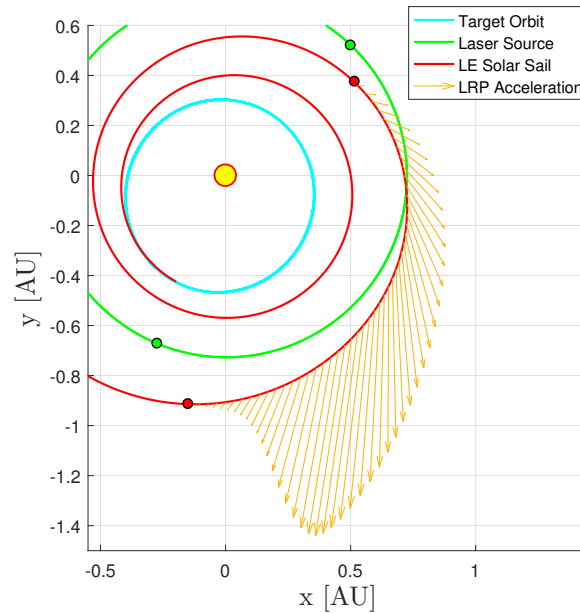


Figure 7.6: LRP acceleration experienced by the laser-enhanced sailcraft along its transfer trajectory to the Mercury orbit. The green and red circles represent the positions of the LS and laser-enhanced sailcraft at the beginning or the end of the CLSA.

this is used for irradiating a sailcraft orbiting at a smaller heliocentric distance. In fact, in these cases a combination of solar occultations and sail back-side exposures defines for most of the time unfavorable LS-sailcraft configurations, which in turn require the LG to be powered off. All of this makes the CLSA the only LRP thrusting period actually provided by the LS, hence highlighting even more how its presence plays a crucial role for laser-enhanced sailcraft missions to the inner Solar System.

For the above-presented mission scenario, the optimal traditional and laser-enhanced sailcraft flight times found are respectively equal to 535 and 477 days. Therefore the TOF gain achieved through the additional use of the LS has been 10.8% of the traditional solar sail TOF.

## 7.2. MARS ORBIT RENDEZVOUS

For this scenario the LS has been put in the Sun-Earth  $L_5$  point, so that both the sailcraft and LS departure positions lie in the Earth orbital plane, with an angular distance of  $\sim 60$  deg between the two. As a consequence, in order to consider all possible sailcraft-LS departure configurations, the departure date time span 63306 – 63671 MJD (corresponding to 15 March 2032 - 15 March 2033) has been used for this case, which has a length of 1 year.

In a similar fashion to the Mercury orbit rendezvous, also in this case 25 preliminary optimization runs have been performed using traditional solar sailing, while another 10 have been used to refine the preliminary optimal result achieved. In this way an optimal trajectory with a TOF of 577 days and a departure date equal to 63499 MJD (24 September 2032) has been found. Similarly, 50 laser-enhanced solar sail trajectory

optimizations have been run for preliminary assessing the most promising region of the search space and, subsequently, 20 more refinement runs have been performed. In this way a laser-enhanced trajectory with TOF of 527 days and departure date equal to 63320 MJD (29 March 2032) was found.

The above-mentioned flight time-optimal traditional and laser-enhanced trajectories are shown in Figure 7.7.

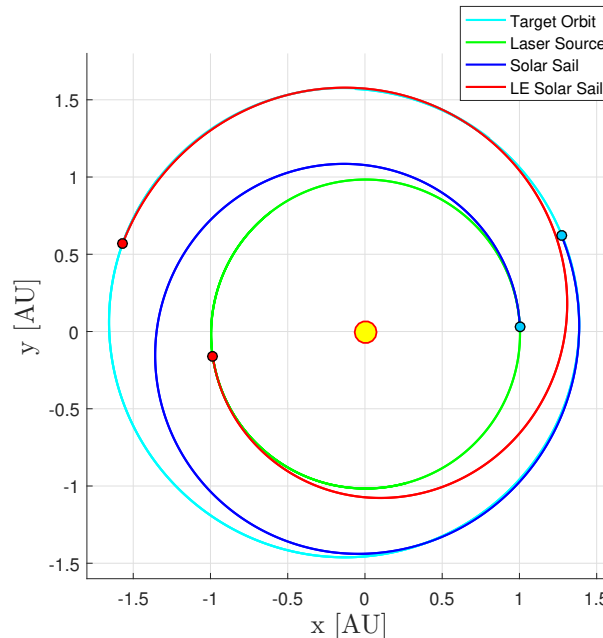


Figure 7.7: Flight time-optimal trajectories to Mars orbit using traditional and laser-enhanced solar sails. The blue and red circles represent the initial and final positions of the traditional and laser-enhanced sailcraft, respectively.

The above trajectory plot shows that the two sailcraft orbits are similar in shape but differ considerably in terms of departure positions, as these are diametrically opposed to one another. Unlike the optimal trajectories found for the Mercury orbit rendezvous, here such a big difference is present because the optimizer has a weaker "preference" in rendezvousing the target orbit in a particular (arrival) position. This is due to the relatively small eccentricities of the departure and target orbits considered, which make trajectories departing at very different points along the Earth orbit have nonetheless similar flight times.

As for the Mercury orbit rendezvous, also in this case the clock angles of both sailcraft follow a similar trend, dictated by the need of slightly changing the orbital inclination throughout the flight (see Figure 7.8). However, as expected, the  $\delta$  values assumed are always small (on average), as to make the sailcraft accelerate and increase the orbital radius.

More interesting are instead the trends followed by the sailcraft pitch angles  $\alpha$ , provided in Figure 7.9. Despite they assume values always in the same range throughout the transfer, during the first part of the flight the laser-enhanced sail pitch angle is, on average, higher than the traditional sailcraft one. This translates into the laser-enhanced sailcraft being more tilted with respect to the Sun and, at the same time, with its normal unit vector directed more towards the Sun-Earth  $L_5$  point, where the LS is

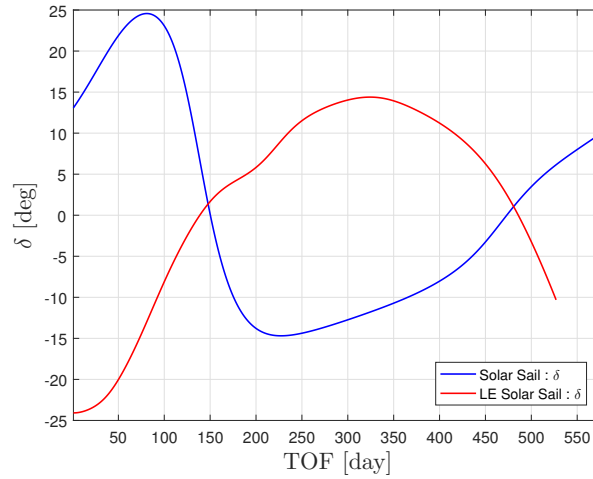


Figure 7.8: Clock angles of the traditional and laser-enhanced solar sails for the Mars orbit rendezvous mission.

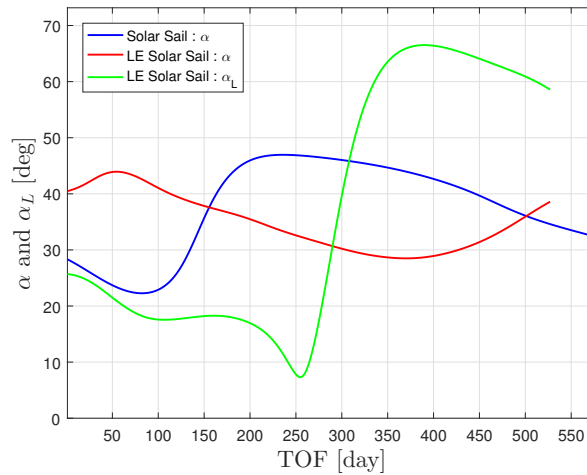


Figure 7.9: Pitch angles of the traditional and laser-enhanced solar sails for the Mars orbit rendezvous mission.

placed. As a consequence, during this first flight segment the laser pitch angle  $\alpha_L$  assumes values smaller than  $\alpha$ , as to make the laser-enhanced sailcraft take into account also the LRP provided by the LS besides the SRP. As time passes, the laser-enhanced orbital radius gradually increases while, on the other hand, its mean motion decreases, thus becoming smaller than the LS one. Such an effect makes the difference in the true anomaly between LS and laser-enhanced sailcraft decrease, so that the former gradually gets closer to the latter. In this way the laser pitch angle decreases too, so that, after  $\sim 255$  days from departure, the smallest  $\alpha_L$  value equal to  $\sim 7$  deg is achieved. Right after this moment the LS actually "overtakes" the laser-enhanced sailcraft, thus making the laser distance also get minimum while yielding a peak in the LRP acceleration (see Figures 7.10 and 7.11). Apart from such an acceleration peak achieved approximately at 270 days from departure, Figure 7.11 also shows how the LRP becomes ineffective soon after this moment, due to the unfavorable LS-sailcraft geometry defined after the LS overtake. In fact, since the laser distance gradually increases while the  $\alpha_L$  angle

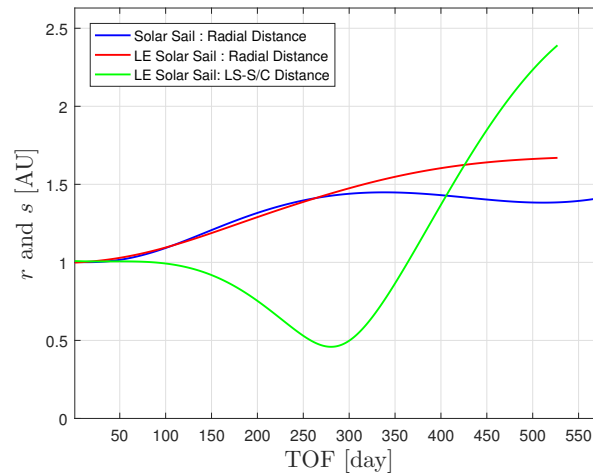


Figure 7.10: Orbital radius and laser distance of the traditional and laser-enhanced solar sails for the Mars orbit rendezvous mission.

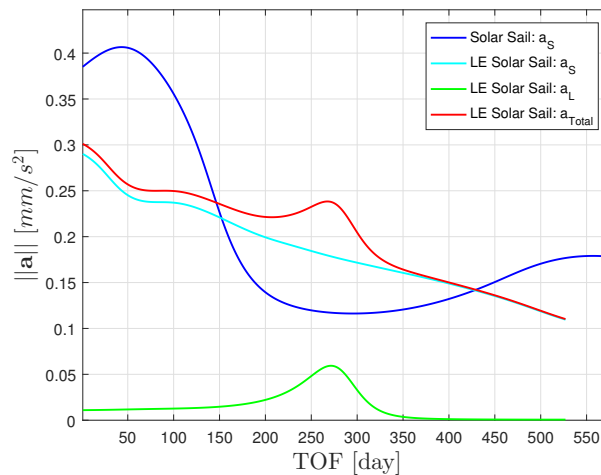


Figure 7.11: Magnitude of the SRP, LRP and total accelerations experienced by the traditional and laser-enhanced solar sails for the Mars orbit rendezvous mission.

reaches values above 60 deg in a short time, the LRP acceleration exerted suddenly drops, thus making the LS actually unable to provide thrust during this last flight segment. On the opposite, Figure 7.11 comes in handy also to appreciate the crucial role played by the LS during the first part of the transfer, in which a continuous slightly increasing LRP acceleration is provided while the SRP gradually decreases. Such a prolonged efficient exploitation of the LRP is mainly due to the LS position which, for most of the transfer, results to be relatively close to the sailcraft.

Unlike the mission to Mercury's orbit, the optimal laser-enhanced sailcraft trajectory shown in this section has highlighted how an LS can be efficiently used to provide a continuous acceleration, thus yielding reduced transfer times. Once again the relative position of the LS with respect to the sailcraft along its entire orbit plays a central role, since either a high laser pitch angle or laser distance can lead to a poor LRP pro-

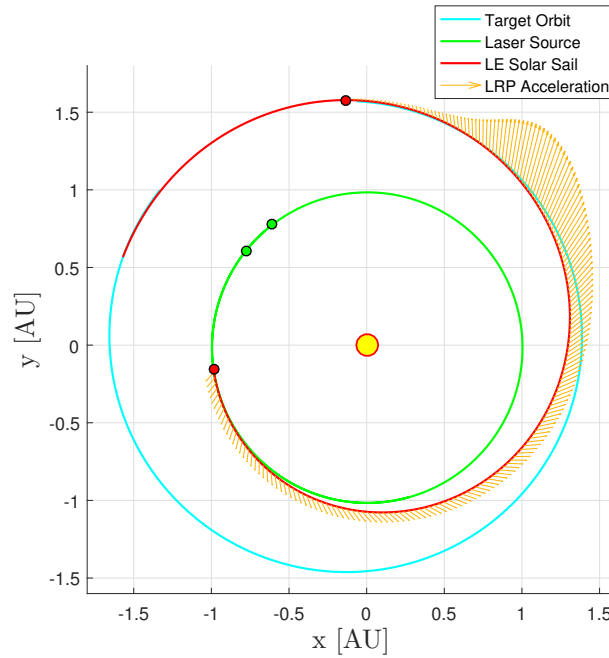


Figure 7.12: LRP acceleration experienced by the laser-enhanced sailcraft along its transfer trajectory to the Mars orbit. The green and red circles represent the positions of the LS and laser-enhanced sailcraft at the beginning or the end of the high LRP provision period.

vision and thus to an inefficient exploitation of the LG power. For transfer trajectories to outer planets as the one discussed in this section, placing the LS in the Sun-Earth  $L_5$  point results to be an advantageous choice, since for most of the flight a considerable amount of LRP is provided. However also other LS orbits being potentially more attractive might exist which could lead to a better exploitation of the laser power in the last part of the transfer.

For the above-analyzed mission scenario the flight times of the traditional and laser-enhanced trajectories are respectively equal to 577 and 527 days, meaning that the TOF gain is about 8.7%.

### 7.3. NEPTUNE FLYBY

In a similar fashion to the Mercury orbit rendezvous mission, also for this case scenario the LS has been placed in the Sun-Venus  $L_4$  point. Therefore the departure time span 62305 – 62889 MJD (18 June 2029 - 23 January 2031) having a length equal to  $T_{\varphi, syn}$  has been used to consider all possible LS-sailcraft departure configurations.

In this case a total of 40 traditional solar sailing optimization runs have been performed, where 25 have been used to initially scan the search space and 15 to refine the best found solution. Similarly, 15 preliminary laser-enhanced solar sailing trajectory optimizations have been performed and other 15 have been run for refinement. By carrying out this procedure, two optimal traditional and laser-enhanced solar sail trajectories have been found, which are shown in Figure 7.13. The traditional solar sail trajectory has a flight time of 2635 days, while for the laser-enhanced sailcraft this is 2570 days. Their departure dates are respectively 62702 MJD (20 July 2030) and

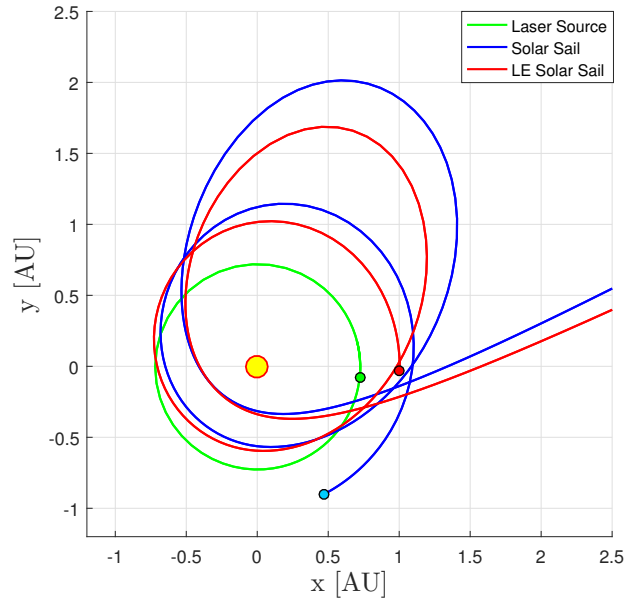


Figure 7.13: Flight time-optimal trajectories to Neptune using traditional and laser-enhanced solar sails. The blue, red and green circles represent the initial positions of the traditional sailcraft, the laser-enhanced sailcraft and the LS, respectively.

62399 MJD (20 September 2029). The trajectories given in the above figure clearly show the presence of two SPAs, similar in shape to the ones of Figure 6.3. Since the SRP and LRP effects on the trajectories are far more pronounced in the first part of the flights, hereafter the orbit analysis will focus mainly on the first 1100 days of flight. In fact, after such an amount of time both sailcraft escape the solar gravitational pull, hence traveling along hyperbolic flight legs and experiencing a negligible radiation pressure acceleration.

Figure 7.14 shows the orbital radius as a function of time for both trajectories. Since during an SPA the orbital radius gets minimum, from such a graph it is possible to recognize the moments at which the solar approaches occur. For the traditional solar sail these take place at about 310 and 870 days from departure, whereas for the laser-enhanced sailcraft they take place after 220 and 650 days.

As can be noticed, the time passed before the first SPA and between the two SPAs is in both cases smaller for the laser-enhanced sail. In particular, since the second SPA takes place earlier, the laser-enhanced sailcraft enters the hyperbolic escape flight segment earlier than the traditional one.

With regard to the laser-enhanced sailcraft, this graph also shows how the laser distance is small during the first days of flight, which is a consequence of the fact that the optimizer has chosen as optimal departure date the one for which the LS and sailcraft are the closest at departure, as shown also in Figure 7.13. As given in Figure 7.15, the trends followed by the clock angles of both solar sails are similar. In particular, during the first days of flight and between the two SPAs, both sailcraft assume  $\delta$  values roughly in the range 100 – 220 deg. In this way a deceleration is provided, which in turn makes the sails approach the Sun closely. Conversely, during the SPAs the clock angles rapidly vary with a view to assuming small values, therefore allowing the sailcraft to accelerate.

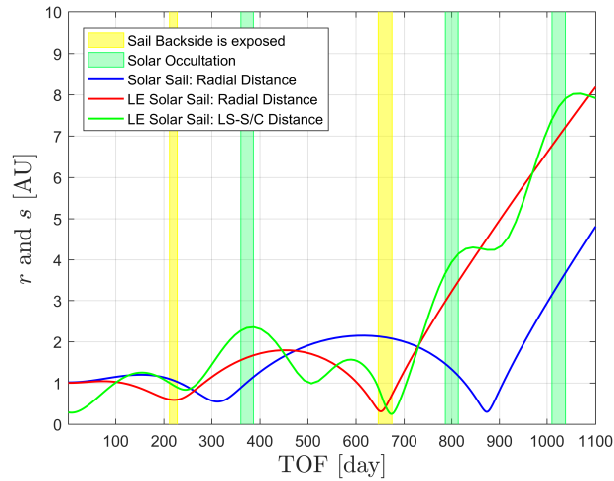


Figure 7.14: Orbital radius and laser distance of the traditional and laser-enhanced solar sails for the Neptune flyby mission.

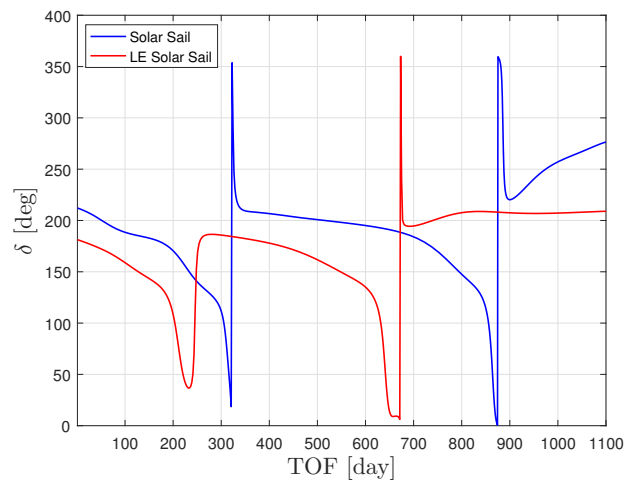


Figure 7.15: Clock angles of the traditional and laser-enhanced solar sails for the Neptune flyby mission.

In particular, in almost all SPAs performed these  $\delta$  variations take place by making the sails turn about the radial direction, hence defining the discontinuities in the graph of Figure 7.15. The only significant difference in the trends of Figure 7.15 can be noticed after the second SPA, where the clock angle of the traditional solar sail increases while the laser-enhanced one remains almost constant. However, as in this phase the sails are already at about 3 AU from the Sun or even more (see Figure 7.14), such a difference in attitude does not affect the motion considerably.

Besides the clock angles, also the pitch angles follow similar trends. In this case they gradually increase before an SPA (also reaching values in the order of 70 – 80 deg), while during the SPAs they rapidly decrease, so that, once the close solar approach has ended, the sail is placed almost normally with respect to the Sun line (see Figure 7.16).

In order to better appreciate the two sailcraft behaviors in proximity of the Sun, Figures 7.17 and 7.18 provide the  $\alpha$  and  $\delta$  values assumed by the sailcraft during the SPAs

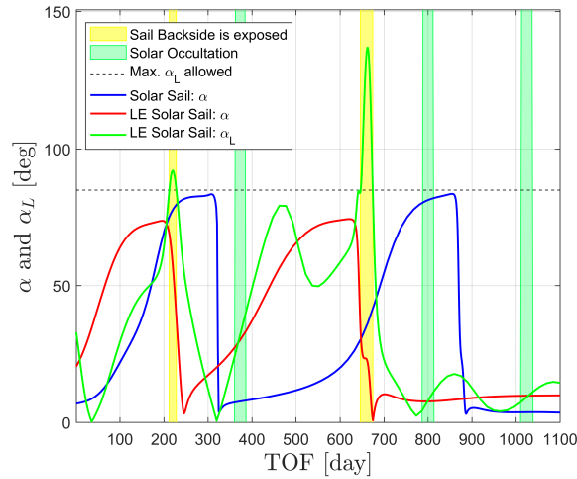


Figure 7.16: Pitch angles of the traditional and laser-enhanced solar sails for the Neptune flyby mission.

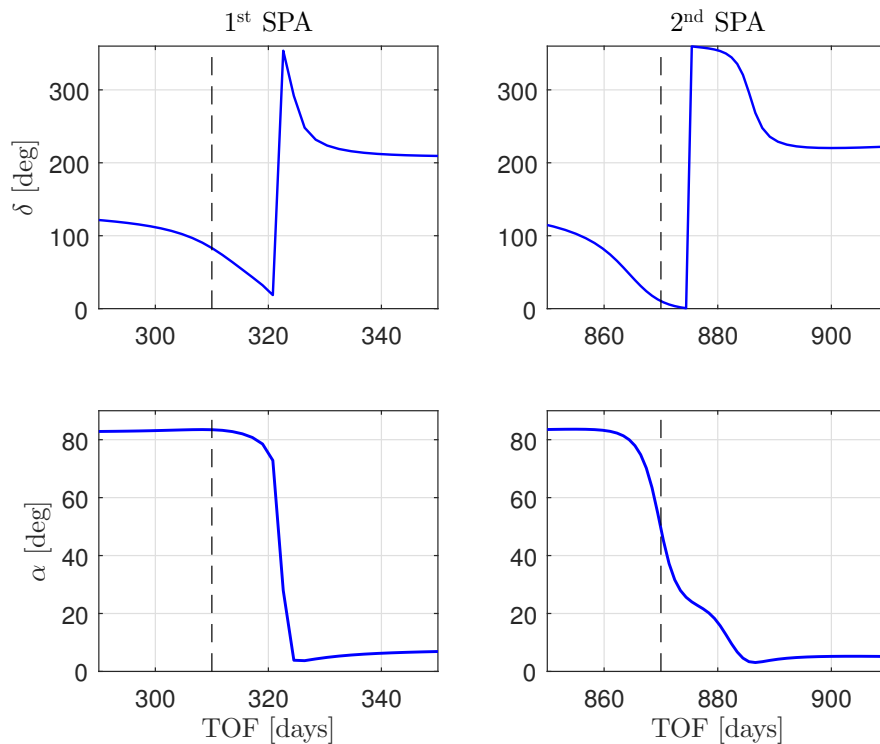


Figure 7.17: Clock and pitch angles of the traditional solar sail during the SPAs and immediately after. The dashed lines represent the times of smallest heliocentric distance.

and after (the dashed lines in the graphs represent the time of smallest heliocentric distance).

As shown in Figure 7.19, during the first days of flight the total acceleration experienced by the laser-enhanced sail is greater than the traditional solar sail acceleration. Such a difference is mainly due to the relatively close laser distance at departure, which yields a high LRP. Since the laser-enhanced sail can take advantage of this additional thrust, the initial deceleration used to spiral towards the Sun is faster and, indeed, the first SPA takes place earlier for the laser-enhanced sailcraft. Even though the LRP con-

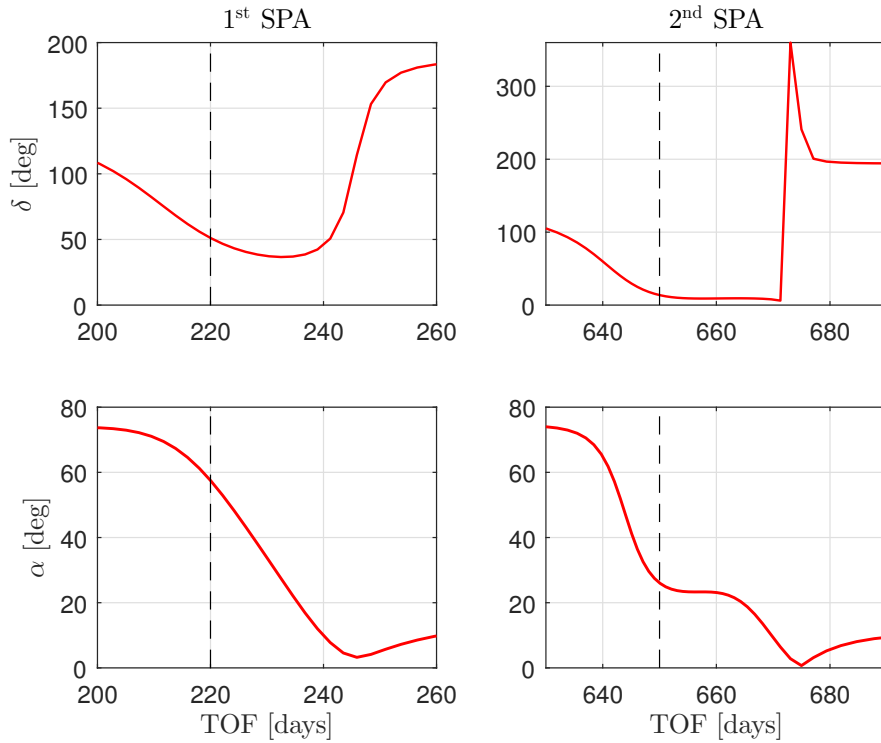


Figure 7.18: Clock and pitch angles of the laser-enhanced solar sail during the SPAs and immediately after. The dashed lines represent the times of smallest heliocentric distance.

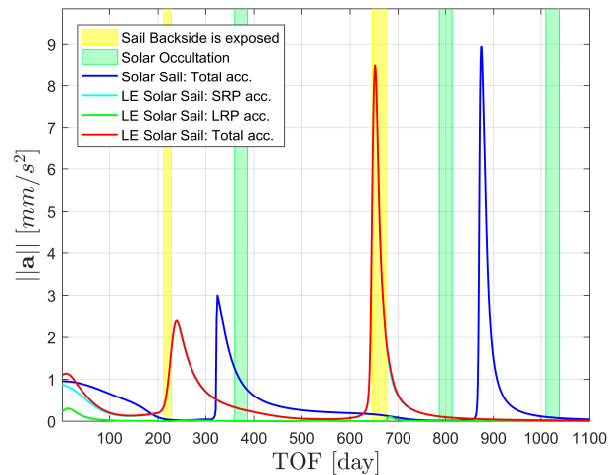


Figure 7.19: Magnitude of the SRP, LRP and total accelerations experienced by the traditional and laser-enhanced solar sails for the Neptune flyby mission.

tributes in such a fast initial deceleration (as can be appreciated in Figure 7.20), for the rest of the trajectory the laser energy is not exploited efficiently, mainly because the laser distance is always high, thus yielding an LRP acceleration practically equal to zero. Only exception in this sense is given by the second SPA during which the laser distance is  $\sim 0.25$  AU (see Figure 7.14). In this case, however, the sail back-side is exposed for most of the time and, even after, the LRP thrust provided results to be many orders of magnitude smaller than the SRP one.

Figure 7.19 also shows how, during both SPAs, the acceleration experienced by the tra-

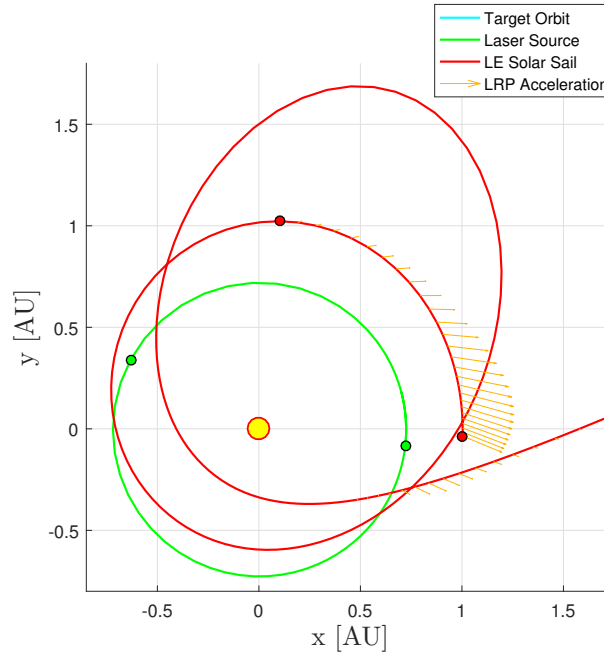


Figure 7.20: LRP acceleration experienced by the laser-enhanced sailcraft along its flyby trajectory to Neptune. The green and red circles represent the positions of the LS and laser-enhanced sailcraft at the beginning or the end of the high LRP provision period.

ditional solar sail is higher than the laser-enhanced sail one. This mainly depends on the fact that the minimum heliocentric distances achieved during the SPAs are 0.55 AU and 0.30 AU for the traditional sail, and 0.59 AU and 0.31 AU for the laser-enhanced one. However, due to the small solar distance, also minor differences in the sail attitude might considerably contribute to such acceleration magnitude differences. In this regard it is also interesting to analyze the efficiency with which the sailcraft exploits the SPAs by looking at Figure 7.21, which shows the specific sailcraft energy variation in time. As can be seen, at the beginning the laser-enhanced sail rapidly loses energy because of the fast deceleration yielded also by the LRP. Consequently, when both sailcraft approach the Sun for the first time, they already have different energies. After the first SPA such an energy gap is still present and, as the traditional solar sail energy is higher, also the orbit dimension is greater, as can be noted in Figure 7.13. Since this energy gap is not filled even with the second SPA, the final energy of the traditional solar sail results to be greater in the final part of the flight, along the hyperbolic escape trajectory. This result also in a higher velocity of the traditional solar sail as compared to the laser-enhanced one, and indeed their velocities at arrival are respectively  $27.3 \text{ km s}^{-1}$  and  $24.8 \text{ km s}^{-1}$ . In spite of this, however, the laser-enhanced sail reaches Neptune first, mainly thanks to the smaller amount of time spent between departure and first SPA, and between the two SPAs.

For this flyby mission the TOF gain has been 65 days only, i.e. 2.5% of the traditional solar sail trajectory flight time. Such a small gain is mainly due the fact that the LRP force influences only to a limited extent the laser-enhanced sailcraft motion, in particular to help it decelerate faster in the first part of the transfer. On the other hand, however, what really delineates the difference in the sailcraft performances is the way

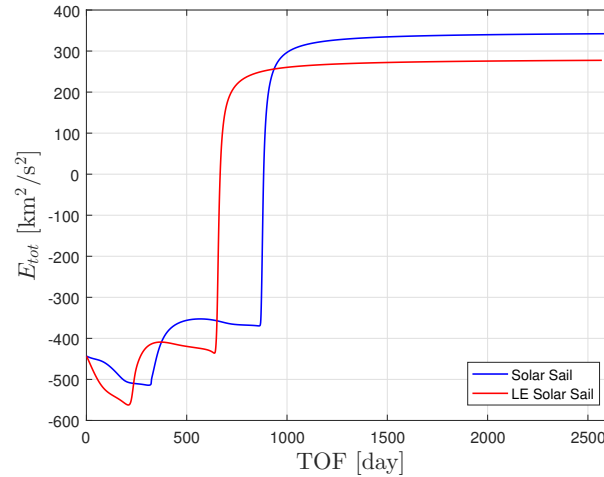


Figure 7.21: Specific energy of the traditional and laser-enhanced solar sails for the Neptune flyby mission.

in which SPAs are performed. In this regard, it resulted that between traditional and laser-enhanced sails, the former acquired the most energy after the two SPAs, hence resulting in a higher escape velocity. As a consequence, if the steering strategies found for this scenario were to be used to reach even further celestial bodies (such as Pluto), it might result that the traditional sailcraft would perform better than the laser-enhanced one. Moreover, unlike the orbit rendezvous mission to Mercury, in this case no CLSA has taken place, thus leading to think that the LS power has not been optimally exploited. Because of these reasons, one cannot be confident that the laser-enhanced trajectory found is close to the global optimum.

Despite the above, the fast deceleration of the laser-enhanced sail shows that the use of additional laser radiation is potentially fruitful also for this type of mission. Consequently there is confidence that the use of a laser-enhanced solar sailing-specific ANN might yield to more accurate optimizations and thus better results. The fact that no CLSAs have been performed for this mission suggests that a first step for the design of a new ANN may be that to implement additional input neurons to specify the LS position or entire state. In fact, in this case the neural network would be able to autonomously make the sailcraft fly towards the LS if needed, hence optimally exploiting the LRP the latter provides.



# 8

## CONCLUSIONS AND RECOMMENDATIONS

This thesis provides a preliminary analysis of laser-enhanced solar sails' performances, especially focusing on interplanetary missions. Such performances have been tested by computing different flight time-optimal trajectories to the inner and outer Solar System, both for "traditional" and laser-enhanced solar sails. In fact, in this way the flight times of both types of sailcraft could be compared, hence providing a mean to efficiently highlight the advantages of the laser radiation pressure as auxiliary thrust source. In particular, three missions have been analyzed: a Mercury orbit rendezvous, a Mars orbit rendezvous and a Neptune flyby.

The mission to the Mercury orbit has clearly shown the advantages provided by close laser source approaches, as when they take place the laser radiation pressure can also become double the solar one. The choice of the departure laser source-sailcraft constellation plays a central role if such laser source approaches are sought, but, on the other hand, if they take place a high thrust is exerted, which can be exploited to spiral inward the Solar System faster and achieve flight time gains of almost 11%. Apart from this, however, it has also been shown that for small sailcraft solar distances the laser source becomes practically unusable. In fact, if the solar sail orbital radius is smaller than the laser source one, a combination of solar occultations and sail back-side exposures makes the laser beam unable to reach the sail front-side for most of the time.

Similarly to the Mercury orbit rendezvous, also the Mars orbit rendezvous has underlined the importance of the laser source positioning for laser-enhanced sailcraft missions. In fact, by placing the laser source in the Sun-Earth  $L_5$  point at departure (i.e. "behind" the sailcraft in the along-track direction), the solar sail can take advantage of a high laser radiation pressure for roughly half of the transfer. In this way a continuous slightly increasing laser radiation pressure acceleration is provided during this period, which makes the sailcraft increase its orbital radius faster compared to a traditional solar sail. Thanks to this effect, it has been shown that a flight time gain of 8.7% can be achieved when using laser-enhanced sailcraft.

Finally, the Neptune flyby mission results have been analyzed and presented. Despite the flight time of the laser-enhanced sailcraft resulted to be about 2.5% shorter than the traditional sailcraft one, there is confidence that the laser-enhanced trajectory found is not close to the global optimum. The reason behind this is that, even if the laser source has been placed in the Sun-Venus  $L_4$  point as for the Mercury orbit rendezvous,

in this case no laser source close approach has taken place, hence leading to think that the laser radiation has not been exploited optimally. Despite this, however, the analysis of the orbits computed has shown that the laser source has been successfully used to reduce the time of flight also in this case. In fact, thanks to the additional laser radiation pressure provided at the beginning of the transfer, it has been shown that a laser-enhanced sailcraft can decelerate and spiral towards the Sun faster, in order to perform close solar approaches earlier and rapidly increase the orbital energy to escape the solar gravitational pull.

The research sub-questions at the base of this report have all been answered, since an extensive description and formulation of the laser-enhanced solar sailing dynamical model has been given, a discussion on the best laser source positions to exploit for different types of interplanetary missions has been provided, and the flight time gains related to laser-enhanced solar sailing flight time-optimal trajectories have been found both for missions to the inner and outer Solar System. In spite of this, however, it should be noted that the laser source positions have been chosen also based on the capabilities of the optimizer used, which could not optimize in an effective way trajectories with the laser source orbiting about Earth. Furthermore, concerning the Neptune flyby mission, there is confidence that even more optimal laser-enhanced solar sail trajectories might exist and, therefore, that greater time of flight gains might be found. Given these considerations, it can be concluded that the research question at the base of this project has been answered, even though, on the other hand, performing again this study using an optimizer specifically designed to work with laser-enhanced sailcraft trajectories might yield better results.

In particular, in the case further studies were to be carried out using the same optimizer exploited in this project, the first step to take would be to implement a neural network specifically designed to optimize laser-enhanced sailcraft trajectories. This could be done by taking as starting point the neural network used for traditional solar sailing and add input neurons used for specifying the laser source state. In addition to these, also an ulterior output neuron might be implemented, with a view to making the optimizer autonomously control the laser generator throttle.

Furthermore, in the case promising results were to be found using an optimizer specifically designed for the laser-enhanced sailcraft dynamics, further analysis of this propulsion system may be performed considering more realistic sail models than the ideal reflection one.

Eventually, since this work focused only on interplanetary missions, it would also be interesting to analyze the performances of laser-enhanced solar sailing as compared to traditional solar sailing for geocentric missions (e.g. to perform orbit raising).





# A

## APPENDIX

### A.1. FLIGHT TIME VARIATION DUE TO NEPTUNE'S PERTURBING ACCELERATION

As discussed in Section 3.7, during a Neptune flyby the sailcraft motion can be influenced by gravitational perturbations during the terminal phase of the flight, when inside the planet's SOI. In order to calculate the flyby TOF difference between the case in which the planet's gravity is considered and when it is not, let us consider Equation 3.52, which provides the maximum magnitude of the third-body acceleration. When such a disturbing body is Neptune, one can set  $r_d = a_\Psi = 30.069923$  AU,  $\mu_d = 6.8351 \cdot 10^6 \text{ km}^3 \text{ s}^{-2}$ , while  $r$  varies in the range  $[r_0, r_f] = [a_\Psi - R_{SOI,\Psi}, a_\Psi]$ , with  $R_{SOI,\Psi} = 8.66 \cdot 10^7 \text{ km}$  being the SOI radius. In this way it results that the disturbing acceleration is equal to:

$$a_d(r) = \frac{\mu_\Psi}{a_\Psi^2} \left| \left( \frac{a_\Psi}{a_\Psi - r} \right)^2 - 1 \right| \quad (\text{A.1})$$

Given this, the following chain of relations hold:

$$a_d(r) = \frac{dv}{dt} = \frac{dv}{dr} \frac{dr}{dt} = v \frac{dv}{dr} \implies a_d(r) dr = v dv$$

Therefore, by indicating with the subscripts 0 the values of the variables when entering the SOI, the following can be written:

$$\int_{r_0}^r a_d(\tilde{r}) d\tilde{r} = \int_{v_0}^v \tilde{v} d\tilde{v}$$

Such an integral results in

$$\frac{\mu_\Psi}{a_\Psi^2} \left[ \frac{a_\Psi^2}{a_\Psi - \tilde{r}} - \tilde{r} \right]_{r_0}^r = \frac{1}{2} (v^2 - v_0^2)$$

and therefore:

$$v(r) = \sqrt{v_0^2 + 2 \frac{\mu_\Psi}{a_\Psi^2} \left[ \left( \frac{a_\Psi^2}{a_\Psi - r} - r \right) - \left( \frac{a_\Psi^2}{a_\Psi - r_0} - r_0 \right) \right]} \quad (\text{A.2})$$

In order to retrieve the dependency on time the following can be written

$$v = \frac{dr}{dt} \implies dt = \frac{dr}{v}$$

so that, eventually:

$$t - t_0 = \int_{t_0}^t d\tilde{t} = \int_{r_0}^r \left\{ v_0^2 + 2 \frac{\mu_\Psi}{a_\Psi^2} \left[ \left( \frac{a_\Psi^2}{a_\Psi - \tilde{r}} \right) - \left( \frac{a_\Psi^2}{a_\Psi - r_0} \right) \right] \right\}^{-\frac{1}{2}} d\tilde{r} \quad (\text{A.3})$$

The integral on the RHS of Equation A.4 cannot be solved analytically but only numerically, e.g. by using the Simpson's quadrature technique available in Matlab. Therefore by integrating this equation with  $v_0 = 15 \text{ km s}^{-1}$  until the terminal conditions  $t = t_f$  and  $r = r_f$ , it results that  $\Delta t = t_f - t_0 \approx 66.658$  days.

On the other hand, in the case Neptune's disturbing acceleration is not considered and the sailcraft is assumed to be flying with a constant (escape) velocity  $v_0$ , the following is found:

$$\Delta t = t_f - t_0 = \frac{r_f - r_0}{v_0} \approx 66.802 \text{ days} \quad (\text{A.4})$$

Given the above  $\Delta t$  values, eventually it results that the difference in the TOF between the two cases is  $\sim 0.144$  days.

On the other hand, by performing the same calculations with a higher initial (escape) velocity of  $30 \text{ km s}^{-1}$ , a TOF difference equal to  $\sim 0.020$  days is achieved.

## A.2. FILES MODIFIED AND IMPLEMENTED WITHIN INTRANCE

The following list shows all the C++ files that have been created (in red) or modified (in black) in order to implement laser-enhanced solar sailing optimization within InTrance.

<b>SpaceLib</b>	<b>CLBG.cpp</b>
SpaceConst.h	CInputSC.cpp
	CPropSys.cpp
<b>SCLib</b>	CSC.cpp
<b>CLaserEnhancedSolarSail.h</b>	
<b>CLBG.h</b>	<b>InTrance Project</b>
CInputSC.h	CFlightDynamicsCartesian.h
CPropSys.h	CFlightDynamics.h
CSC.h	CFlightDynamicsCartesian.cpp
SCConst.h	CFlightDynamicsPolar.cpp
<b>CLaserEnhancedSolarSail.cpp</b>	CFlybySim.cpp

## A.3. LASER SOURCE POSITIONING FOR THE MISSIONS TO NEPTUNE AND MARS ORBIT

In a similar fashion to the trade-off described in Section 6.3 for the Mercury's orbit rendezvous mission, also the LS positions used for the Mars orbit rendezvous and Neptune flyby have been determined by taking advantages of Pugh matrices. These are presented hereafter.

### A.3.1. NEPTUNE FLYBY MISSION

The Pugh matrix relative to the choice of the LS position for the Neptune flyby is given in Table A.1. As already shown in Figure 6.3, for this type of trajectory the sailcraft tends to spiral inwards the Solar System in order to perform SPAs. Since also for performing Mercury's orbit rendezvous the sailcraft spiral inwards, all considerations made in Section 6.3 are valid also in this case, translating in the below Pugh matrix being equal to the one given in Table 6.2. Therefore once again placing the LS in an inner Solar System orbit results to be the best option. More specifically, it was chosen to put the LS in the Sun-Venus  $L_4$  point, just as for the mission to Mercury's orbit.

Table A.1: Pugh matrix used for comparing different LS positioning options for the Neptune flyby mission.

Criteria	Weights	LEO	HEO	$L_4$	< 1 AU
$\Delta V$ budget	1	+1	0	0	-1
LS Eclipse	3	-1	+1	+1	+1
Obstruction from other S/C	1	-1	0	+1	+1
Relative geometry	3	+1	+1	-1	0
Optimization	4	-1	-1	+1	+1
	<b>Sum</b>	-4	+2	+5	+7

### A.3.2. MARS ORBIT RENDEZVOUS MISSION

The Pugh matrix used for choosing the LS position for the Mars orbit rendezvous is given in Table A.2. Main difference between this matrix and the ones presented for the other two scenarios is that this time the Sun-Earth  $L_4$  point has been considered instead of the Sun-Earth  $L_5$  one. In spite of this, most of the considerations made in Section 6.3 for the Mercury orbit rendezvous hold also in this case, and therefore many of the values in the below Pugh matrix are the same of Table 6.2. The only exceptions are represented by the values related to the "relative geometry" criterion. In fact, unlike the Mercury orbit rendezvous mission, in this case placing the LS in an inner Solar System orbit does not represent a good choice, since to get to the Mars orbit the sail-

Table A.2: Pugh matrix used for comparing different LS positioning options for the Mars orbit rendezvous mission.

Criteria	Weights	LEO	HEO	$L_5$	< 1 AU
$\Delta V$ budget	1	+1	0	0	-1
LS Eclipse	3	-1	+1	+1	+1
Obstruction from other S/C	1	-1	0	+1	+1
Relative geometry	3	+1	+1	+1	-1
Optimization	4	-1	-1	+1	+1
	<b>Sum</b>	-4	+2	+11	+4

craft needs to spiral outwards. On the other hand, placing the LS in the Sun-Earth  $L_5$  point turns out to be advantageous as the LS in this way is placed behind the sailcraft (in the along-track direction) for a long time and can continuously provide LRP thrust. Based on these reasons, the below Pugh matrix has been designed, indeed showing that placing the LS in the Sun-Earth  $L_5$  position represents the best choice.





## REFERENCES

- G. Beals, R. Crum, H. Dougherty, D. Hegel, and J. Kelley. Hubble Space Telescope precision pointing control system. *Journal of Guidance, Control, and Dynamics*, Volume 11(2):pp.119–123, 1988.
- J. K. Beatty, B. O'Leary, and A. Chaikin. *The new Solar System*, Sky Publishing Corporation, Cambridge, MA. 1981.
- Breakthrough Initiatives. Launch - Precision pointing for a meter-scale lightsail. <http://breakthroughinitiatives.org/index.php?controller=Forum&action=viewforum&id=2&page=2>, a. Date of access: 24-09-2017.
- Breakthrough Initiatives. Lightsail integrity under thrust. <http://breakthroughinitiatives.org/index.php?controller=Forum&action=viewforum&id=5&page=5>, b. Date of access: 24-09-2017.
- Breakthrough Initiatives. Starshot. <http://breakthroughinitiatives.org/Initiative/3>, c. Date of access: 24-09-2017.
- L. Carzana. Laser-enhanced solar sailing for interplanetary missions - Literature study report. Technical report, TU Delft, 2017.
- Colorado Center for Astrodynamics Research (CCAR). Interplanetary transfers using low thrust. [http://ccar.colorado.edu/asen5050/projects/projects\\_2001/parker/Interplanetary.html](http://ccar.colorado.edu/asen5050/projects/projects_2001/parker/Interplanetary.html). Date of access: 27-10-2017.
- B. Dachwald. *Low-thrust trajectory optimization and interplanetary mission analysis using evolutionary neurocontrol*. PhD thesis, Universität der Bundeswehr München Fakultät für Luft-und Raumfahrttechnik, Germany, 2004.
- B. Dachwald. Optimal solar sail trajectories for missions to the outer Solar System. *Journal of Guidance, Control, and Dynamics*, Volume 28(6):pp.1187–1193, 2005.
- B. Dachwald. Solar sail dynamics and control. In *Encyclopedia of Aerospace Engineering*. Wiley Online Library, 2010.
- B. Dachwald and A. Ohndorf. InTrance 2.6: It's a kind of manual, October 2010.
- S. Davidovich and J. Whittington. Concept for continuous inter-planetary communications. *Space Manufacturing*, 12, 1999.
- J. Davis. LightSail test mission declared success, first image complete, *The Planetary Society*. <http://www.planetary.org/blogs/jason-davis/2015/20150609-lightsail-test-mission-success.html>, June 9, 2015. Date of access: 11-06-2017.

- A. De Marco and D. P. Coiro. Lecture notes of "Dinamica e Simulazione di Volo", Quaderno 2, *Department of Aerospace Engineering - Università degli Studi di Napoli "Federico II"*, Italy, January 2016a.
- A. De Marco and D. P. Coiro. Lecture notes of "Dinamica e Simulazione di Volo", Quaderno 3, *Department of Aerospace Engineering - Università degli Studi di Napoli "Federico II"*, Italy, January 2016b.
- J. Diebel. Representing attitude: Euler angles, unit quaternions, and rotation vectors. *Matrix*, 58(15-16):1–35, 2006.
- S. Dodelson. *Modern cosmology*. Academic Press, 2003.
- eoPortal. IKAROS (Interplanetary Kite-craft Accelerated by Radiation Of the Sun). <https://directory.eoportal.org/web/eoportal/satellite-missions/i/ikaros>, a. Date of access: 11-06-2017.
- eoPortal. JWST (James Webb Space Telescope) - Characteristics. <https://directory.eoportal.org/web/eoportal/satellite-missions/j/jwst>, b. b. Date of access: 26-09-2017.
- eoPortal. LightSail missions of The Planetary Society. <https://eoportal.org/web/eoportal/satellite-missions/content/-/article/lightsail1>, c. Date of access: 11-06-2017.
- eoPortal. NanoSail-D (NanoSail-Demonstration). <https://eoportal.org/web/eoportal/satellite-missions/n/nanosail-d>, d. Date of access: 11-06-2017.
- R. Falck and J. Dankanich. Optimization of low-thrust spiral trajectories by collocation. In *AIAA/AAS Astrodynamics Specialist Conference, AIAA Paper 2012*, page 4423, August 2012.
- J. Finseth. ROVER nuclear rocket engine program: Overview of rover engine tests. Final report. Technical report, Sverdrup Technology, Inc., Huntsville, AL (United States), for NASA Marshall Space Flight Center, 1991.
- R. L. Forward. Roundtrip interstellar travel using laser-pushed lightsails. *Journal of Spacecraft and Rockets*, Volume 21(2):pp.187–195, 1984.
- A. P. French. *Special relativity*. CRC Press, 1968.
- L. Friedman. The rise and fall of Cosmos 1. <http://sail.planetary.org/story-part-2.html>. Date of access: 11-06-2017.
- R. L. Garwin. Solar sailing - A practical method of propulsion within the Solar System. *Jet Propulsion, AIAA*, Volume 28(3):pp.188–190, 1958.
- U. Geppert, B. Biering, F. Lura, J. Block, and R. Reinhard. The 3-step DLR-ESA Gossamer Roadmap to solar sailing. [http://www.dlr.de/Portaldata/46/Resources/dokumente/systemkonditionierung/DLR-ESA\\_Gossamer.pdf](http://www.dlr.de/Portaldata/46/Resources/dokumente/systemkonditionierung/DLR-ESA_Gossamer.pdf), 2010. Date of access: 26-09-2017.

- S. Hassani. *Mathematical methods: for students of physics and related fields*, volume 720. Springer Science & Business Media, 2008.
- D. Hatch. The right way to calculate stuff. <http://www.plunk.org/~hatch/rightway.php>. Date of access: 18-10-2017.
- J. Hennessy, K. Balasubramanian, C. S. Moore, A. D. Jewell, S. Nikzad, K. France, and M. Quijada. Performance and prospects of far ultraviolet aluminum mirrors protected by atomic layer deposition. *Journal of Astronomical Telescopes, Instruments, and Systems*, 2(4):041206–1–041206–9, 2016.
- L. Herbeck, M. Leipold, C. Sickinger, M. Eiden, and W. Unckenbold. Development and test of deployable ultra-lightweight CFRP-booms for a solar sail. In *Spacecraft Structures, Materials and Mechanical Testing*, volume 468, pages 107–112, 2001.
- L. Herbeck, C. Sickinger, M. Eiden, and M. Leipold. Solar sail hardware developments. In *European Conference on Spacecraft Structures, Materials and Mechanical Testing, Toulouse*, pages 1–10, 2002.
- L. Honorio, J.-G. Bartaire, R. Bauerschmidt, T. Ohman, Z. Tihanyi, H. Zeinhofer, J. Scowcroft, V. De Janeiro, H. Kruger, H.-J. Meier, D. Offerman, and U. Langnickel. Efficiency in electricity generation. Technical report, Eurelectric: Union of the Electric Industry, Brussels, Belgium, in collaboration with VGB Powertech, Essen, Germany, 2003.
- A. Janota, V. Šimák, D. Nemeč, and J. Hrbček. Improving the precision and speed of Euler angles computation from low-cost rotation sensor data. *Sensors*, 15(3):7016–7039, 2015.
- Japan Aerospace Exploration Agency (JAXA). IKAROS. <http://www.isas.jaxa.jp/en/missions/spacecraft/current/ikaros.html>. Date of access: 11-06-2017.
- Japan Aerospace Exploration Agency (JAXA). Small solar power sail demonstrator 'IKAROS': Successful attitude control by liquid crystal device. Press release, July 23, 2010a. URL [http://global.jaxa.jp/press/2010/07/20100723\\_ikaros\\_e.html](http://global.jaxa.jp/press/2010/07/20100723_ikaros_e.html). Date of access: 11-06-2017.
- Japan Aerospace Exploration Agency (JAXA). Small solar power sail demonstrator 'IKAROS': Confirmation of photon acceleration. Press release, July 9, 2010b. URL [http://global.jaxa.jp/press/2010/07/20100709\\_ikaros\\_e.html](http://global.jaxa.jp/press/2010/07/20100709_ikaros_e.html). Date of access: 11-06-2017.
- L. Johnson. Solar sails for spacecraft propulsion. <https://ntrs.nasa.gov/archive/nasa/casi.ntrs.nasa.gov/20160005683.pdf>, 2016. Date of access: 26-09-2017.
- L. Johnson, J. Castillo-Rogez, J. Dervan, and L. McNutt. Near Earth Asteroid (NEA) Scout. In *4<sup>th</sup> International Symposium on Solar Sailing (ISSS 2017), Kyoto, Japan*, pages 1–5, January 2017.
- G. Kopp. Magnitudes and timescales of total solar irradiance variability. *Journal of Space Weather and Space Climate*, 6:A30, 2016.

- V. Kumar. The theorems of Euler and Chasles, *University of Pennsylvania School of Engineering and Applied Science, I-Net, USA*, 2000.
- J. J. Lissauer and I. De Pater. *Fundamental planetary science: physics, chemistry and habitability*. Cambridge University Press, USA, 2013.
- P. Llanos, J. Miller, and G. Hintz. Mission and navigation design of integrated trajectories to L4/L5 in the Sun-Earth system. In *AIAA/AAS Astrodynamics Specialist Conference 2012-4668*, 2012.
- M. Macdonald. *Advances in solar sailing*. Springer Science & Business Media, 2014.
- A. Marinan, J. Castillo-Rogez, L. Johnson, J. Dervan, C. Seybold, and E. Betts. Near Earth Asteroid (NEA) Scout cubesat mission. <http://www.lcpm12.org/wp-content/uploads/2017/08/1455-1515-Marinan.pdf>. Date of access: 14-11-2017.
- L. Mazzini. *Flexible spacecraft dynamics, control and guidance*. Springer, 2016.
- C. R. McInnes. *Solar sailing: technology, dynamics and mission applications*. Springer-Verlag, 1999.
- W. Moeckel. Propulsion by impinging laser beams. *Journal of Spacecraft and Rockets*, Volume 9(12):pp.942–944, 1972.
- O. Montenbruck and E. Gill. *Satellite orbits: models, methods and applications*. Springer Science & Business Media, 2012.
- National Aeronautics and Space Administration (NASA). Mercury fact sheet. <https://nssdc.gsfc.nasa.gov/planetary/factsheet/mercuryfact.html>, a. Date of access: 22-10-2017.
- National Aeronautics and Space Administration (NASA). Neptune fact sheet. <https://nssdc.gsfc.nasa.gov/planetary/factsheet/neptunefact.html>, b. Date of access: 07-11-2017.
- National Aeronautics and Space Administration (NASA). Sun fact sheet. <http://nssdc.gsfc.nasa.gov/planetary/factsheet/sunfact.html>, c. Date of access: 02-10-2017.
- National Aeronautics and Space Administration (NASA). Technology demonstration mission. [https://www.nasa.gov/mission\\_pages/tdm/solarsail/solarsail\\_overview.html#WKI6RG8rLIU](https://www.nasa.gov/mission_pages/tdm/solarsail/solarsail_overview.html#WKI6RG8rLIU), d. Date of access: 11-06-2017.
- National Aeronautics and Space Administration (NASA). Venus fact sheet. <https://nssdc.gsfc.nasa.gov/planetary/factsheet/venusfact.html>, e. Date of access: 29-10-2017.
- National Aeronautics and Space Administration (NASA). Small Satellite Missions - Image Gallery. [https://www.nasa.gov/mission\\_pages/smallsats/nsd\\_team.html](https://www.nasa.gov/mission_pages/smallsats/nsd_team.html), 2008. Date of access: 11-06-2017.

- NIST: National Institute of Standards and Technology. Fundamental physical constants - Extensive listing. <http://physics.nist.gov/cgi-bin/cuu/Category?view=pdf&All+values.x=60&All+values.y=12>. Date of access: 04-11-2017.
- N. Perakis, L. E. Schrenk, J. Gutmiedl, A. Koop, and M. J. Losekamm. Project Dragonfly: A feasibility study of interstellar travel using laser-powered light sail propulsion. *Acta Astronautica*, Volume 129:316–324, 2016.
- L. Rios-Reyes. *Solar sails: modeling, estimation, and trajectory control*. PhD thesis, University of Michigan, USA, 2006.
- RP Photonics Encyclopedia. Wall-plug efficiency. [https://www.rp-photonics.com/wall\\_plug\\_efficiency.html](https://www.rp-photonics.com/wall_plug_efficiency.html). Date of access: 09-10-2017.
- E. F. Schubert, T. Gessmann, and J. K. Kim. *Light emitting diodes*. Wiley Online Library, 2005.
- Space.com. World's largest solar sail to launch in November 2014. <http://www.space.com/21556-sunjammer-solar-sail-launch-2014.html>, 2013a. Date of access: 13-02-2017.
- Space.com. Photos: Meet Sunjammer, world's largest solar sail. <https://www.space.com/23172-sunjammer-solar-sail-photos.html>, 2013b. Date of access: 14-11-2017.
- Spacenews.com. NASA nixes Sunjammer mission, cites integration, schedule risk. <http://spacenews.com/42227nasa-nixes-sunjammer-mission-cites-integration-schedule-risk/>. Date of access: 14-11-2017.
- P. Sprangle, J. Penano, B. Hafizi, and I. Ben-Zvi. Wall-plug efficiencies of high-power free electron lasers employing energy recovery linacs. Technical report, Naval Research Laboratory, Washington DC, Beam Physics Branch, Plasma Physics Division, 2009.
- T. Taylor, R. C. Anding, D. Halford, G. L. Matloff, and A. V. Pakhomov. Space-based energy beaming requirements for interstellar laser sailing. In *AIP Conference Proceedings*, volume 664, pages 369–381. AIP, 2003.
- T. Tsu. Interplanetary travel by solar sail. *Ars Journal*, Volume 29(6):pp.422–427, 1959.
- TUDAT. Acceleration Set-Up. <http://tudat.tudelft.nl/tutorials/tudatFeatures/accelerationSetup/index.html>. Date of access: 14-10-2017.
- S. Turner, A. Back, G. Brown, and B. Hall. P1\_10 delta-v requirements of spaceflight. *Physics Special Topics*, 10(1), 2011.
- K. F. Wakker. *Fundamentals of Astrodynamics*. TU Delft Library, Delft, the Netherlands, 2015.
- M. Walker. A set of modified equinoctial orbit elements. *Celestial Mechanics and Dynamical Astronomy*, 38(4):409–419, 1986.
- B. Wie. Solar sail attitude control and dynamics, part 1. *Journal of Guidance, Control, and Dynamics*, Volume 27(4):526–535, 2004.